HEAT TRANSFER TO SMALL CYLINDERS AND FLAT STRIPS IMMERSED IN A FLUIDIZED BED

by

Dennis Rosero

Bachelor of Engineering (B.Eng.)

Ryerson University, Toronto, 2004

A thesis

presented to Ryerson University

in partial fulfillment of the

requirements for the degree of

Master of Applied Science

in the Program of

Mechanical Engineering

Toronto, Ontario, Canada, 2006

AUTHOR'S DECLARATION

I hereby declare that I am the sole author of this thesis. I authorize Ryerson University to lend this thesis or dissertation to other institutions or individuals for the purpose of scholarly research.

I further authorize Ryerson University to reproduce this thesis by photocopying or by other means, in total or in part, at the request of other institutions or individuals for the purpose of scholarly research.

BORROWER

Ryerson University requires the signature of all persons using or photocopying this thesis.

Please sign below, and give address and date.

ABSTRACT

Heat Transfer to Small Cylinders and Flat Strips Immersed in a Fluidized Bed
Dennis Rosero, M.A.Sc., 2006
Program of Mechanical Engineering
Ryerson University

Fluidized bed heat treating systems have been used to heat treat low carbon steel wires for a number of years. Extending this application to high carbon steel wires and metal straps has been implemented with very little success due to the lack of knowledge of heat transfer coefficients or, alternatively, Nusselt number for small cylinders and flat strips. The objective of this study was to provide reliable data for predicting a suitable Nusselt number for small horizontal cylinders and flat strips at various orientations under conditions typically encountered in heat treating fluidized bed systems.

In this study, resistively heated small cylinders and flat strips ranging in diameter from 1.27 to 9.53mm and in width from 6.25 to 25.4mm respectively were immersed in a 311mm in diameter lab-scale fluidized bed. The bed consisted of fine alumina oxide sand of mean particle size ranging from 145 to 330μm fluidized by air at ambient temperatures. The fluidized bed unit was capable of fluidizing rates ranging from 0.14 to 23 G/G_{mf}. The cylinder and flat strip samples were positioned horizontally in the bed. The flat strip samples were rotated around the length's center axis in 15° increments from a 0° horizontal position to a 90° vertical position.

The results showed that published correlations over-predict small cylinder Nusselt numbers over the entire fluidizing range; furthermore, their trends did not agree. Flat strip results demonstrated highest heat transfer rates at a vertical position. A correlation that predicts the mean Nusselt number within ±15% for both geometries was developed for operating conditions covered by the experiments.

ACKNOWLEDGEMENTS

I would like to thank my supervisors Dr. Jake Friedman and Dr. David Naylor for giving me the opportunity to continue my education at the graduate level. Their financial support, guidance and expertise in their respective fields helped me greatly throughout my thesis and course work.

I am also grateful to all technical support staff at Ryerson University for their assistance in various matters during the experiments. Sincere thanks to Roy Churaman.

I am genuinely thankful to my engineering colleagues Tony Avedissian, Tom Krajac, Andy Constantinou and Azar Hojabr for their amity and loyal friendship. A special thanks to all my friends for good times. I more than ever thank my adoring fiancée Laura Bongertman for her moral support, love, and companionship.

Finally, I am forever in debt to my parents and brother for their everlasting support in everything I do.

TABLE OF CONTENTS

CHAPTER FOUR

CHAPTER FIVE

CHAPTER SIX

CHAPTER SEVEN

CHAPTER EIGHT

LIST OF TABLES

LIST OF FIGURES

NOMENCLATURE

A_c Cross Sectional Area of Sample (m^2)

A_b Effective Bed Area (m^2)

A_s Outside Surface Area of Sample (m^2)

A_T Throat Area of Venturi (m^2)

Ar Archimedes Number, $Ar = \frac{\rho_g d_p^3 (\rho_p - \rho_g) g}{\mu_g^2}$

C_v Discharge Coefficient

C_{pg} Specific Heat of Fluidizing Gas at Constant Pressure (J/kg-K)

C_{ps} Specific Heat of Solid Particles at Constant Pressure (J/kg-K)

d_p Particle Diameter (m)

d_s Outer Diameter of Cylinder (m)

d_T Throat Diameter of Venturi (m)

g Acceleration due to Gravity (m/s^2)

G Fluidizing Gas Mass Flow Rate (kg/m^2-s)

G_{mf} Fluidizing Gas Mass Flow Rate at Minimum Fluidization (kg/m^2-s)

h Heat Transfer Coefficient (W/m^2-K)

h_{avg} Average Heat Transfer Coefficient (W/m^2-K)

h_{gc} Gas Convective Component (W/m^2-K)

h_{pc} Particle Convective Component (W/m^2-K)

h_{rad} Radiant Component (W/m^2-K)

h_{tot} Total Bed-to-Surface Heat Transfer Coefficient (W/m^2-K)

H_{mf} Bed Particle Height at Minimum Fluidization (m)

I Current (A)

k Thermal Conductivity of Sample Material (W/m-K)

k_{air} Thermal Conductivity of Air (W/m-K)

k_g Fluidizing Gas Thermal Conductivity (W/m-K)

k_p Thermal Conductivity of Particle (W/m-K)

L Sample Length (m)

L_c Characteristic Length (m)

Nu Nusselt Number, $Nu = \frac{h_{avg} L_c}{k_g}$

Nu_{exp} Experimental Nusselt Number

Nu_{mean} Mean Nusselt Number

$Nu_{pred,cyl}$ Predicted Nusselt Number for Small Cylinders

$Nu_{pred,strips}$ Predicted Nusselt Number for Flat Strips

P Perimeter of Samples (m), defined in Table 5.1

P_o Power (W)

Pr Gas Prandtl Number, $Pr = \frac{\mu_g C_{pg}}{k_g}$

q_x Heat Conduction into the CV (W)

q' Heat Generation per Unit Length (W/m)

q''' Volumetric Heat Generation (W/m^3)

Q Air Flow Rate Through Venturi Meter or Rotameter (m^3/s or CFM)

r Radius of Cylinder (m)

r_i Inner Radius of Cylinder (m)

r_o Outer Radius of Cylinder (m)

R Resistance (Ω)

Re_{mf} Reynolds Number at Minimum Fluidization, $Re_{mf} = \frac{\rho_g d_p U_{mf}}{\mu_g}$

t Time (s)

t_s Thickness of Flat Strip Sample (m)

T_{film} Film Temperature (K or °C)

T_s Surface Temperature of Sample (K or °C)

T_T Terminal Temperature (K or °C)

T_∞ Bed Temperature (K or °C)

U Superficial Gas Velocity (m/s)

U_{mf} Minimum Fluidization Velocity (m/s)

V Voltage (V)

w_{A_s} Uncertainty in Sample Surface Area

w_{A_T} Uncertainty in Venturi Throat Area

w_{C_v} Uncertainty in Discharge Coefficient

w_I Uncertainty in Current

w_s Width of Flat Strip Sample (m)

w_V Uncertainty in Voltage Drop

$w_{\Delta P}$ Uncertainty in Pressure Difference

$w_{\Delta T}$ Uncertainty in Sample Temperature Difference

w_β Uncertainty in Throat-to-Pipe Diameter Ratio

w_{ρ_g} Uncertainty in Gas Density

W_h Overall Uncertainty in Heat Transfer Coefficient

W_Q Overall Uncertainty in Air Flow Rate

x Position Along Sample (m)

GREEK SYMBOLS

β Throat-to-Pipe Diameter Ratio of Venturi

ΔP Pressure Drop Across the Bed

ΔT Temperature Difference Between Sample Surface and Bed (K or °C)

ε Bed Voidage Fraction

ε_b Bulk Bed Voidage

ε_{mf} Bed Voidage Fraction at Minimum Fluidization

ε_s Surface Voidage

μ_g Fluidizing Gas Viscosity (N-s/m^2)

τ Particle Residence Time (s)

ρ_g Density of Fluid/Gas (kg/m^3)

ρ_P Density of Solid Particles (kg/m^3)

ρ_{rcs} Resistivity of Stainless Steel, $\rho_{rcs} = 720 n\Omega$-m

φ_s Sphericity Factor

θ_o Angle Orientation of Flat Strip (°)

θ_T Excess Terminal Temperature

ACRONYMS

CV Control Volume

GW Good Will Instrument Co.

RMSE Root Mean Square Error

S+S Sprecher+Schuh Relay

T/C Thermocouple

CHAPTER ONE

INTRODUCTION

1.1 INTRODUCTION

Fluidized beds possess very high heat transfer capability; therefore, their potential to be used in the heat treatment industry has not been ignored. Heat transfer between fluidized beds and immersed surfaces is one of several sub-processes of importance in the application of the fluidized bed as a heat treating medium. It is necessary for design purposes that methods of predicting the heat transfer rate to immersed surfaces be available. Considerable research has been reported on heat transfer to/from immobile tubes, walls and thick plates in gas fluidized beds [1, 2], but very little research has been done for other geometries such as flat strips and small cylinders. The present work investigates heat transfer coefficients, or alternatively Nusselt numbers, for thin flat strips at different orientations and small horizontal cylinders immersed in a gas-solid fluidized bed.

1.1.1 SMALL CYLINDERS

The steel wire industry has adopted fluidized bed technology in the manufacturing process of its wires. The wires that have been previously work-hardened by drawing machines often need to be heat-treated to achieve proper material properties, such as tensile strength and

ductility. The heat treatment of steel wires from either low or high carbon steel is described well by Koundakjian [3] and is summarized below.

The heat treatment of steel wires is accomplished in either batch processes or continuous processes. In batch processes, many spools or strands of wire, each weighing several hundred to several thousand pounds, are loaded into a furnace. The furnace is then sealed up and heated until the wire is fully treated over a period of several hours to a few days. In continuous heat treating processes, wire strands move continuously through a furnace. Continuous wire heat treating operations for both low and high carbon steel wires are discussed below.

Traditional continuous low carbon wire heat treatment consists of immersing the wire in a tank of molten lead at approximately 730°C for a period of time until the wire temperature reaches approximately 710°C. The heat treatment cycle for this material is relatively undemanding compared to the heat treatment of high carbon steels. High carbon steel wire heat treatment requires precise control of product temperature and heating rates, as well as controlled quench rates. In a process called patenting, the wire must be heated to over 800°C, followed by a rapid, controlled quench to 480°C, and finally a soak at 480°C is required. The patenting process is achieved using two furnaces. The first one is usually a direct fired furnace operating at approximately 1050°C. Once the wires emerge from this furnace, they are immediately fed into a lead quench furnace via special rollers or sinkers. Molten lead furnaces are traditionally used to achieve the desired steel structure configuration for both low and high carbon steel wires in continuous processes; however, many jurisdictions prohibit the use of lead-based systems due to serious health and environmental concerns, forcing steel wire manufacturers to seek alternative furnaces for their heat treatment processes, such as the fluidized bed.

Fluidized bed furnaces have been used successfully for heat treating low carbon steel wire for several years. Under the correct conditions, these fluidized beds offer high heat transfer efficiencies and have virtually no environmental issues. Heat treating high carbon steel wire in a fluidized bed furnace has been employed with very little success due to the lack of adequate information on heat transfer rates to cylinders in the size range of 1 to 10mm in diameter.

Many researchers have studied heat transfer to boiler-tube sized cylinders (25 to 50mm diameter) immersed in fluidized beds. However, extrapolating the correlations developed for boiler-tubes to small cylinders has produced contradictory results. The work reported herein studies heat transfer to small cylinders in a lab-scale fluidized bed of fine grit aluminum oxide sand operated at ambient temperatures.

1.1.2 FLAT STRIPS

Steel strapping is widely used to stabilize and secure pallet loads for packaging and transporting. To obtain the steel configuration needed, the steel strap undergoes a heat treatment process similar to that used for steel wire. The steel strap is made from medium carbon steel ranging in width from 6.35mm (¼") to 31.75mm (1¼"). In a continuous process, the steel is annealed in a lead bath furnace at approximately 800°C followed by an air quench. Similar to the reasons stated above for steel wire, an alternative to lead furnaces to heat treating steel straps is essential for future manufacturing.

In the present study, heat transfer to flat strips of 6.35 (¼") to 25.4mm (1") in width will be examined. These strips are immersed in a lab-scale fluidized bed of fine grit aluminum oxide sand operated at ambient temperature. It is also of interest to establish the strip's orientation for best heat transfer in a fluidized bed.

1.2 LITERATURE REVIEW

The study of heat transfer to horizontal cylinders immersed in a fluidized bed is not a new area of research. The majority of work in this area has focused on heat transfer rates to boiler tubes immersed in coal-firing fluidized bed combustors in the power generation industry, and has been well summarized by Botterill [4] and Saxena [1]. As already mentioned, little work has been done in investigating small diameter cylinders immersed in a fluidized bed and nearly no work has been done for flat strips since their geometries have no design applications for fluidized beds in the power generation industry, the industry driving most Fluidized Bed research. The work done by previous researchers is discussed below.

Vreedenberg [5] measured heat transfer coefficients from fluidized beds to horizontal water-cooled tubes. Experiments were conducted with the tube fixed 0.85m above the sieve plate (distributor) in a 0.565m bed diameter and height of 1.2m in the non-fluidized state. Six parameters were varied including bed temperature, mass velocity of the fluidizing air, mean particle diameter, particle shape, particle density and water-tube diameter. The types of particles included regenerated cracking catalyst and fine sand with particle diameter varying from 63.5 to 316μm. The outer diameter of the tube varied from 16.9 to 51mm. Vreedenberg developed a correlation for predicting the heat transfer coefficient based on the assumption that fluidized fine particles follow the path of the gas and that the motion of coarser particles would be less dependent on the gas path. On this basis, the correlation is recommended only when the value of the Reynolds number is higher than 2550 and when, moreover, all the variables are within or nearly within the range covered by the operating conditions in the experiments.

Andeen and Glicksman [6] measured heat transfer rates for horizontal tubes in shallow fluidized beds. Experiments were conducted in a 0.6m square fluidized bed. The fluidized bed

walls were made of clear plastic and the bed was filled with various types of sand particles ranging in diameter 360 to 710μm. The electrically heated tube was made of aluminum and had a 19mm diameter. Andeen and Glicksman correlated their data well with a modified version of the Vreedenberg [5] correlation, which included a (1-ε) term, suggesting the heat transfer from tube to bed is a strong function of the bed voidage. The correlation was stipulated to be valid only for air at standard conditions.

Grewal and Saxena [7] conducted experiments to measure the heat transfer coefficient (h) between an electrically heated single horizontal tube and air-solid fluidized beds of glass beads, dolomite, sand, silicon carbide and alumina particles of 259μm diameter. Three tube diameters varying from 12.7 to 28.6mm of different material composition (bronze and copper) were tested. They reported that the effect of tube material had no influence on h, but the value of h decreased with an increase in tube diameter, in agreement with Vreedenberg's [5] observations. Grewal and Saxena proposed a modified correlation based on Vreedenberg's correlation with an additional dimensionless factor which accounts for the volumetric heat capacity of solid particles, the tube diameter, and the thermal conductivity of the fluidizing gas. The new correlation agreed with their experimental values of h within an uncertainty of ±25% (presented in Section 2.4.3) and is in good agreement with the data of other investigators.

Petrie *et al.* [8] conducted heat transfer experiments between a tube bundle of 19 horizontal 25.4mm diameter tubes in a 0.3m diameter bed. A correlation was developed to best fit their results, showing that the heat transfer coefficient is inversely related to the particle diameter and the tube diameter and is directly related to the reduced fluidizing mass velocity. A comparison to Vreedenberg's [5] correlation for heat transfer to a single tube showed a good

agreement, indicating that the individual heat exchanger tubes were essentially unaffected by the other tubes for tube-to-tube separations exceeding 43 particle diameters.

Baskakov *et al.* [2] studied heat transfer to objects immersed in fluidized beds of 92 and 98mm diameter. Tests were conducted on a 30mm diameter vertical, water-cooled, stainless steel tube immersed in beds of corundum and slag beads ranging in particle diameter from 120 to 650μm. The fluidizing gases were carbon dioxide, helium (both at a temperature of 20°C) and air at temperatures from 20°C to 550°C. The effect of shape and position was studied by measuring heat transfer rates from a flat calorimeter while varying the position from a vertical position to a horizontal position. A modified packet model was developed that took into account the effective gap heat resistance between the packet of particles and surface and for the heat transferred directly by convection through the gas filtering through the particles and between the particles and the immersed object.

Rasouli *et al.* [9] investigated the effect of annular fins of a horizontal immersed tube in bubbling fluidized beds. Experiments were carried out in a cylindrical Plexiglas column of inner diameter 90mm and a height of 260mm. The unfinned horizontal steel tube had a 15mm outside diameter and was 50mm long. The tube was resistively heated and placed 70mm above the distributor plate. The solid particles used were silica sand with 200 and 307μm diameters. Experimental results showed values of h increasing with increasing gas velocity up to a certain value with no significant changes by increasing the gas velocity further. Furthermore, they observed that increasing the particle diameter from 200μm to 307μm reduces h substantially, in agreement with other published results [1, 4].

Saxena [1] reported a summary of all the research contributions in the field of heat transfer between a smooth horizontal tube and fluidized beds. Several correlations were

examined, some of which are presented in section 2.4.3. According to Saxena's analysis, almost all the correlations for predicting the Nusselt number corresponded to a certain limit of operating conditions specified by the researcher and only the correlation proposed by Grewal and Saxena [7] was able to predict the greater part of the available data in the literature, as well as their own experimental data, within an uncertainty of ±25%.

Koundakjian [3] investigated heat transfer rates to wire-sized cylinders between 1 and 6mm diameter immersed in a pilot-scale fluidized bed. The bed consisted of aluminum oxide fine sand with grit number 60 corresponding to a mean particle diameter of 254μm. Heat transfer tests were conducted under cold (air only) and hot (air/natural gas mixture) bed conditions. The experimental Nusselt numbers were well predicted by Grewal and Saxena's correlation within the stated uncertainty value of ±25% for U/U_{mf} between 1.3 and the maximum U/U_{mf} value tested. The fluidized bed furnace was limited to fluidizing rates up to 3 x U/U_{mf}.

Most of the work cited above was of experiments conducted on relatively large tube diameters, summarized in Table 1.1. There does not appear to have been much work done for small cylinders and virtually no work done for flat strips. The work reported in this thesis involves measuring heat transfer rates for small cylinders and flat strips at different orientations immersed in a solid-gas fluidized bed. In addition, a correlation is developed to predict the Nusselt number within the operating conditions tested for both geometries. An attempt is made to include published data with the proposed correlations.

Table 1.1 – Summary of Work Cited

Reference	Material	Particle Diameter d_p (μm)	Tube Diameter d_s (mm)	Bed Temperature (°C)
Vreedenberg [5]	Regenerated Cracking Catalyst	63.5	16.9-51	50-250
	Sand used for Sandblasting	136		
	Maas Sand	316		
	Dune Sand	230	16.9-33.6	
Andeen and Glicksman [6]	Ottawa Sand	360, 510, 710	19	Ambient Temperature
Grewal and Saxena [7]	Silicon Carbide	178	12.7-28.6	Ambient Temperature
	Alumina	362		
	Silica	259		
	Dolomite	167, 451 504		
	Glass Beads	293, 312		
	Lead Glass	265, 357, 427		
		241		
Petrie *et al.* [8]	Small Sand	256-735	25.4	130-500
Baskakov *et al.* [2]	Corundum	120, 320, 500	30	20-550
	Slag Beads	650		
Rasouli *et al.* [9]	Silica Sand	200, 307	15	Ambient Temperature
Koundakjian [3]	Aluminum Oxide Sand	254	1-6	$Ambient_{(cold)}$ $100\text{-}675_{(hot)}$

CHAPTER TWO

THEORETICAL CONSIDERATIONS

2.1 GAS-SOLID FLUIDIZATION

A gas-solid type fluidized bed is a bed of finely divided solid particles placed in a container with a porous base plate (distributor) through which a gas is pumped passing upwards through the bed. The air percolates through the particles and emerges at the surface.

Figure 2.1 illustrates the regimes of fluidization. As the gas velocity is increased, the air pressure at the base of the bed, and hence the drag force acting on the particles, will also increase until a point is eventually reached at which the drag force is equal to the gravitational force holding the particles within the container. The bed expands upwards as the particles become suspended in the flowing air stream. In this state, known as the point of *incipient fluidization*, the fluid/particle system begins to behave like a fluid. The pressure drop across the bed will be equal to the weight of the bed, although it is likely that this pressure drop will be exceeded just prior to the achievement of fluidization with gas-fluidized systems because the residual packing and interlocking of particles within the bed must first be broken down (this is indicated by the "hump" in the stylized curve for bed pressure drop as a function of the fluid flow rate) [4]. The superficial gas velocity (U) at which this occurs is called the 'minimum fluidization velocity', U_{mf}, and its value depends on the physical properties of the gas and of the solid particles. As the

gas velocity is increased above U_{mf}, the bed pressure drop remains constant. Gas bubbles form within the bed and rise to the surface where they burst like bubbles of a boiling liquid. A further increase in gas velocity leads to more vigorous bubbling with bigger bubbles appearing at the surface. If the ratio of the height to the diameter of the bed is high enough, the size of bubbles may become almost the same as the diameter of the bed. The bed is then said to be 'slugging' and it is characterized by a considerable heaving of the surface with many particles being thrown up into space above the bed [10]. The bed becomes turbulent at higher gas flow rates and eventually reaches an entrainment state with further gas velocity increase. This is where the fluidized bed is in a dilute or lean phase, which amounts to pneumatic transport of solids. The intense mixing and gas solids contact make it easy to have an isothermal system with good mass transfer; therefore, a fluidized bed is ideal for reaction, drying, mixing and heat transfer applications [11]. Heat transfer in fluidized beds is discussed in more detail in subsequent sections.

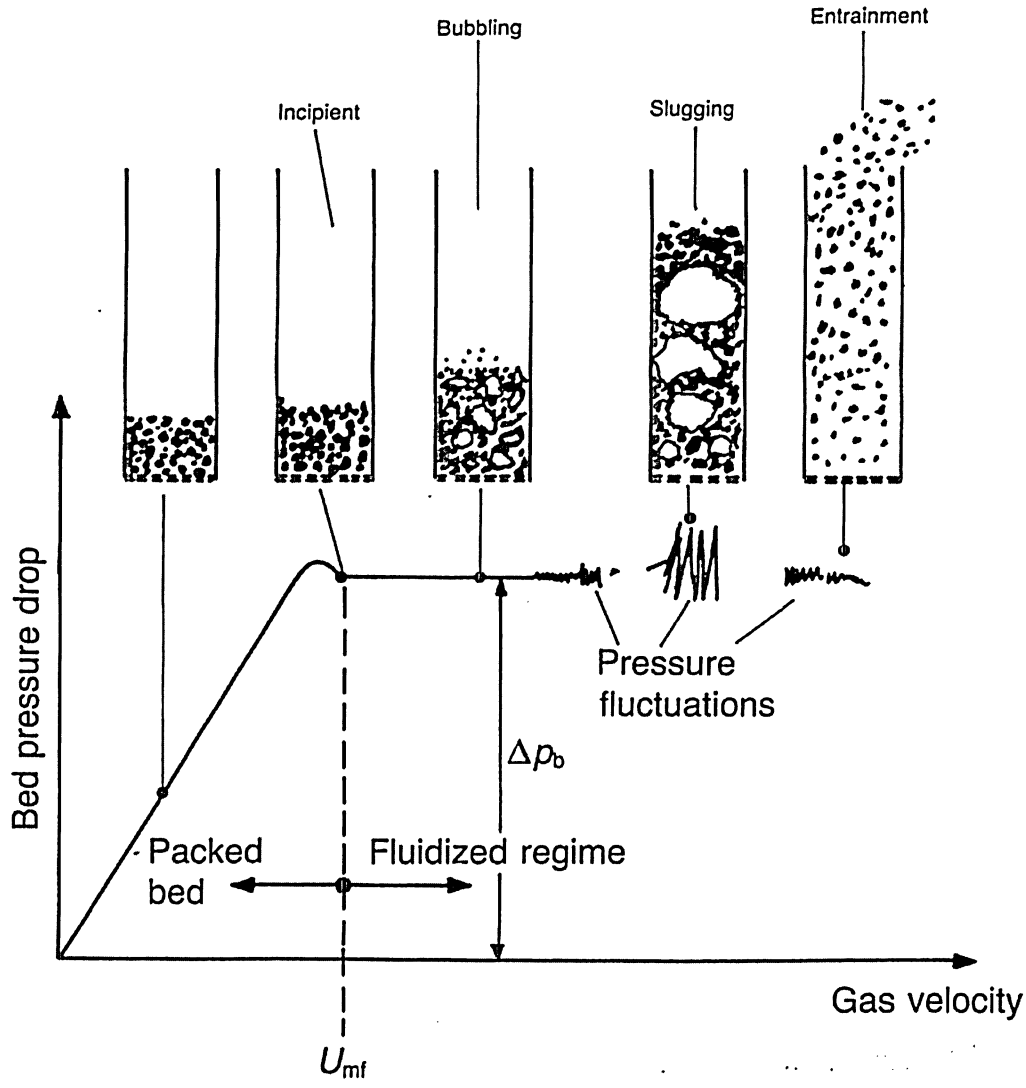

Figure 2.1 – Regimes of Fluidization (Adapted from [12])

2.2 CLASSIFICATION OF PARTICLES

Several types of particles can be used for different fluidized bed applications, each having its own fluidizing properties. Geldart [13] published a categorization of particles that considers the hydrodynamic behaviour of solid particles forming a bed when fluidized by a gas. The particles are classified in four groups, namely, A, B, C and D. A 'phase diagram' showing the boundaries of the various groups is given in Figure 2.2. The groups are dependent on the density difference between the particle density (ρ_p) and fluid/gas density (ρ_g) and the particle diameter (d_p).

Group A particles are designated as aeratable and form a slightly cohesive structure. They are commonly encountered as cracking catalyst powders that are used in the fuel refinery industry. Group B powders are identified as 'sand-like' particles. They begin to bubble at gas velocities just in excess of U_{mf}. Examples of Group B materials are coarse sand and glass beads (ballotini). Powders which are in any way 'cohesive' belong in Group C, which are mainly fine powders and are very difficult to fluidize under normal conditions. Examples of group C materials are talc, flour and starch. Group D powders are known as 'spoutable' and are confined to large and/or very dense particles. Lead shot and some roasting metal ores are examples of group D powders.

Geldart's classification is straightforward to use, as illustrated in Figure 2.2. The graph helps predict the type of fluidization to be expected for any solid of a known density and mean particle size. It also helps predict fluidizing behaviours such as bubble size, bubble velocity, the existence of slugs etc. Particles used in the current experiment fall in Group B and are discussed in detail in Chapter 5.

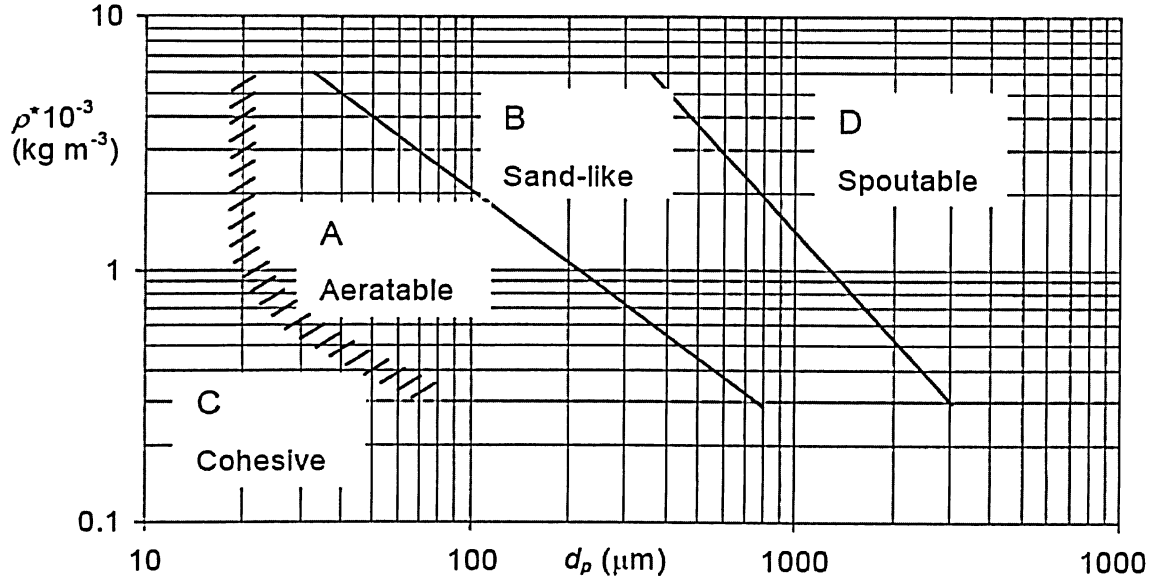

Figure 2.2 – Geldart Powder Classification Diagram for Fluidization by Air-Ambient Conditions $\rho^* = \rho_p - \rho_g$ (According to [13])

2.3 MINIMUM FLUIDIZATION VELOCITY, U_{mf}

The gas velocity at which a bed of powder becomes fluidized may be found by measuring the pressure drop across the bed as a function of gas velocity. As described in the previous section, when gas passes through a sand bed, the drag force exerted on the particles will cause the particle spacing to expand after the inter particle adhesion force is overcome. The bed pressure increases as the gas velocity is increased up to a point where the bed pressure drop remains constant. This velocity is defined as the minimum fluidization velocity, U_{mf}. A number of empirical expressions are available which give the value of U_{mf} for a particular powder in terms of the physical properties of the solid particles and of the fluidizing gas. Following is a derivation of one equation for predicting the minimum fluidization velocity [1, 10].

When the pressure drop stops increasing with increasing gas velocity, the force exerted by the upward flowing fluid is equal to the gravitational force acting on the particles:

$$\frac{\Delta P}{H_{mf}} = (1-\varepsilon_{mf})(\rho_p - \rho_g)g \tag{2.1}$$

where,

ΔP = Pressure drop across the bed
H_{mf} = Bed particle height at minimum fluidization
ε_{mf} = Bed voidage fraction at minimum fluidization
ρ_p = Particle density
ρ_g = Gas density

The Ergun [14] equation is used to describe the drag force:

$$\frac{\Delta P}{H} = \frac{150(1-\varepsilon)^2}{\varepsilon^3}\frac{\mu_g U}{(\varphi_s d_p)^2} + \frac{1.75(1-\varepsilon)}{\varepsilon^3}\frac{\rho_g U^2}{\varphi_s d_p} \tag{2.2}$$

where,

ε = Bed voidage fraction

$$\varepsilon = \frac{\text{Volume of bed} - \text{Volume of particles}}{\text{Volume of bed}}$$

μ_g = Gas viscosity

U = Gas velocity

d_p = Particle diameter

For beds of non-spherical particles it is necessary to introduce a sphericity factor φ_s defined as:

$$\varphi_s = \frac{\text{surface area of sphere of volume equal to that of particle}}{\text{surface area of particle}}$$

Thus $\varphi_s = 1$ for perfect spheres and $0 < \varphi_s < 1$ for other shapes. The following table presents typical sphericities of various particles.

Table 2.1 – Typical Sphericities of Particles

Type of Particle	Sphericity (φ_s)
Glass Beads	1.00
Sand (round)	0.92 – 0.98
Coal (crushed)	0.8 – 0.9
Silica	0.8 – 0.9
Alumina	0.3 – 0.8

Combining Equations (2.1) and (2.2) and substituting $\varepsilon = \varepsilon_{mf}$ and $U = U_{mf}$ with $\varphi = 1$ yields:

$$\frac{\rho_g d_p^3 (\rho_p - \rho_g) g}{\mu_g^2} = \frac{150(1-\varepsilon_{mf})}{\varepsilon_{mf}^3} \frac{\rho_g d_p U_{mf}}{\mu_g} + \frac{1.75}{\varepsilon_{mf}^3} \frac{\rho_g^2 d_p^2 U_{mf}^2}{\mu_g^2} \tag{2.3}$$

Equation (2.3) can be further simplified:

$$Ar = \frac{150(1-\varepsilon_{mf})}{\varepsilon_{mf}^3} Re_{mf} + \frac{1.75}{\varepsilon_{mf}^3} Re_{mf}^2 \tag{2.4}$$

where the Reynolds number at minimum fluidization is defined as:

$$Re_{mf} = \frac{\rho_g d_p U_{mf}}{\mu_g} \tag{2.5}$$

and the Archimedes number Ar is defined as:

$$Ar = \frac{\rho_g d_p^3 (\rho_p - \rho_g) g}{\mu_g^2} \tag{2.6}$$

One of the problems in applying the Ergun equation to the calculation of U_{mf} is that the minimum fluidization voidage is frequently unknown and tends to vary from one researcher to another. Wen and Yu [15] found that for a range of particle types and sizes the following two empirical relationships were valid:

$$\frac{1-\varepsilon_{mf}}{\varphi_s \varepsilon_{mf}^3} \approx 11; \quad \frac{1}{\varphi_s \varepsilon_{mf}^3} \approx 14 \tag{2.7}$$

An approximate value of 0.4 for ε_{mf} is used [1], simplifying Equation (2.4):

$$Re_{mf} = \frac{Ar}{1400 + 5.22\sqrt{Ar}} \tag{2.8}$$

It is recognized that in deriving Equation (2.8), the product term in solving the quadratic equation (2.4) is neglected, and that this approximation has a pronounced effect in the transitional flow regime [1]. The quadratic equation (2.4) must be used for higher values of the Reynolds number ($Re_{mf} > 10$) at the point of incipient fluidization.

Solving for U_{mf} from Equations (2.5) and (2.8) gives:

$$U_{mf} = \frac{\mu_g}{\rho_g d_p} \frac{Ar}{\left(1400 + 5.22\sqrt{Ar}\right)} \tag{2.9}$$

Equation (2.9) is used for predicting the minimum fluidization velocity for particle sizes larger than 100μm belonging to Geldart's groups B and D at Reynolds numbers greater than 1 [13].

The fluidizing gas mass flow rate, G, is defined as:

$$G = \frac{\rho_g Q}{A_b} = \rho_g U \tag{2.10}$$

where,

Q = Air flow rate through venturi meter or rotameter
A_b = Effective bed area

The gas mass flow rate is non-dimensionalized by the minimum fluidizing gas mass flux, G_{mf}, given by:

$$G_{mf} = U_{mf}\rho_g \tag{2.11}$$

It is sometimes more convenient to use the non-dimensional parameter G/G_{mf} to describe the fluidizing rate instead of U/U_{mf}. The reason for this is G_{mf} includes the gas density which varies with temperature and type of fluidized gas used, making it easier to compare data at higher temperatures. Another form of Equation (2.11) is:

$$G_{mf} = Re_{mf}\frac{\mu_g}{d_p} \tag{2.12}$$

2.4 HEAT TRANSFER IN FLUIDIZED BEDS

One of the reasons fluidized beds have such wide application is their excellent heat transfer characteristics. Generally, the heat capacity of a fluidized bed is high (approximately $10^6 J/m^3$-K) and the heat transfer coefficient of solid-to-gas ranges from 250 to $700 W/m^2$-K [16]. This is due to the large surface area of particles exposed to the gas and small temperature gradients within the bed. The heat transfer mechanisms involved in the fluidized bed are discussed further below.

2.4.1 GAS-TO-PARTICLE HEAT TRANSFER

Owing to the fact that flow of gas around particles in a fluidized bed is essentially laminar and that the local Reynolds number is correspondingly small, gas-to-particle heat transfer coefficients are typically small, of the order 6 to $23 W/m^2$-K [4]. However, because the bed particles are small and numerous, the total surface area of solid per unit volume of bed exposed to the flowing gas is very large ($3000 - 45000 m^2/m^3$) [4], with the result that the overall heat transfer rate between particles and gas is very high. Furthermore, the larger heat capacities of solids than gases cause a fast equilibration in temperature between an incoming gas and the bed material; therefore, the gas will attain the temperature of the bed within a few particle diameters of the point of entry of the gas [10]. This results in an isothermal fluidized bed.

2.4.2 HEAT TRANSFER TO AN IMMERSED SURFACE

Heat transfer to immersed surfaces in a gas-fluidized bed operating under normal conditions occurs by three modes:

i. The particle convective component, h_{pc}

ii. The gas convective component, h_{gc}

iii. The radiant component, h_{rad} (considered only at temperatures in excess of 600°C)

The relative magnitude of the contribution made by each of these mechanisms depends on factors like flow conditions, the nature of the particles, and the temperature of operation [16]. For this reason, the operational parameters are clearly quite complex and have been the focus of many researchers, as discussed by Saxena [1] and Botterill [4]. The total bed-to-surface heat transfer coefficient is effectively the sum of the above three components:

$$h_{tot} = h_{pc} + h_{gc} + h_{rad} \tag{2.13}$$

The three components are considered independent of one another and are discussed briefly below.

2.4.2.1 PARTICLE CONVECTIVE COMPONENT, h_{pc}

The particle convective component uses the mechanism of energy transfer caused by the motion of particles near the surface. When the particle is in contact with the surface, actual solid-to-solid contact only occurs over a microscopically small area so that the main path through which heat is transferred from the particle to the surface is via the gas separating the particle and the surface [12] known as the 'gas film', illustrated in Figure 2.3. This insinuates that the conduction between the particles and surface through its actual physical contact is small and considered insignificant at fluidizing rates in excess of G_{mf}. This is because the total contact area between the particle and surface is comparatively smaller than the area covered by the gas film. Furthermore, the particles near and in contact with the heat transfer surface are continuously replaced by fresh particles at bed temperatures by the fluidizing behaviour of rising bubbles. It is the temperature gradient that allows the heat to be transferred between particles and the surface.

The amount of heat transferred is governed mainly by the particle residence time, τ, and the gas conductivity, k_g. The shorter the residence time, the greater the temperature difference between the particles and the surface, an important factor in controlling the heat transfer rate. Another important parameter is the size of particles. Smaller particles provide a greater density of contact and a shorter limiting conduction heat transfer path through the gas film adjacent to the surface when traveling in 'packets'. Decreasing the mean gas film thickness by decreasing the particle size improves the particle convective component. Reducing the particle size into the Group C range will reduce particle mobility and so reduce particle convective heat transfer. Figure 2.4 illustrates the model.

The limiting factor for heat transfer between the bed and surface is the gas thermal conductivity, k_g, since virtually all the heat must be transferred through a gas film between the particles and the surface. The larger the thermal conductivity, the more readily heat will flow. Generally, the thermal conductivities of gases are low compared to those of solids.

Thus, to promote heat transfer between a bed of particles and a surface, the densest packing of the smallest particles having the shortest residence times and most frequent replacement is required, together with the most conductive gas. Particle convective heat transfer is the dominant component in Group A and B powders where particle circulation is good.

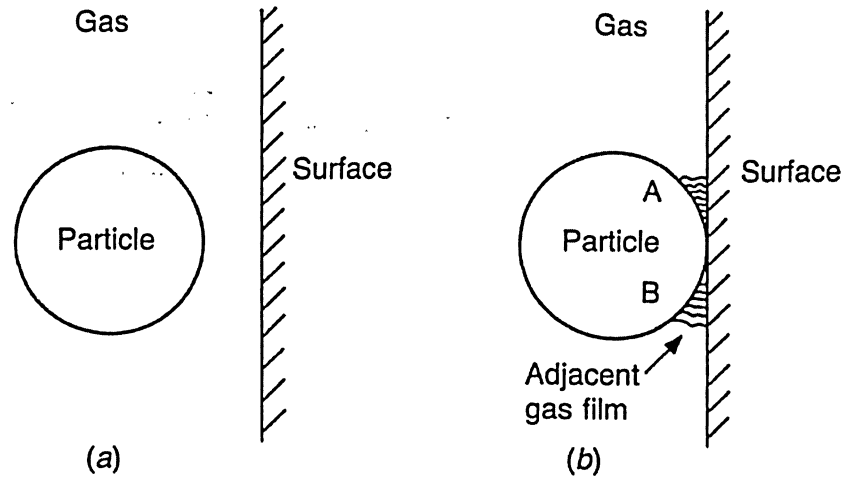

Figure 2.3 – Gas Film Between Particle and Surface (a) Particle Remote from the Surface– negligible heat transfer (b) Particle Residing at the Surface – most heat flows through the gas film adjacent to the sector AB (Adapted from [12])

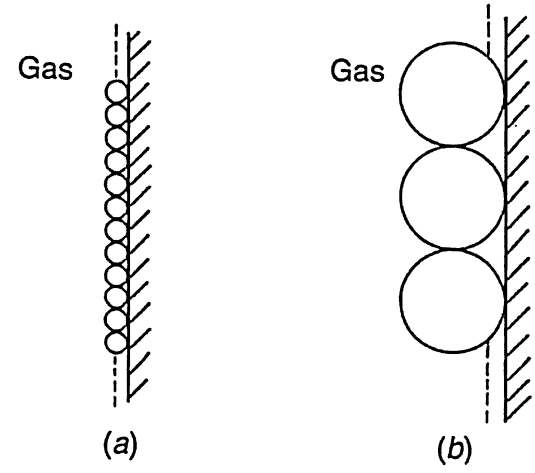

Figure 2.4 – The Effect of Particle Size on the Thickness of Gas Film (a) Small Particles with a large number of points of contact. A large fraction of the particle surface is close to the plane surface. (b) Large particles with a small number of points of contact. A smaller fraction of the particle surface is close to the plane surface. (Adapted from [12])

2.4.2.2 GAS CONVECTIVE COMPONENT, h_{gc}

The gas convective component becomes important when the mean size of the bed particles is large, $d_p > 800\mu m$. Botterill [4] suggests that the gas convective component becomes the dominant mechanism at $Re_{mf} \approx 12.5$. Gas convective heat transfer is the dominant component in Group D powders where higher gas velocities are required to fluidize the bed. This leads to the gas flow regime in the spaces surrounding the particles being transitional or turbulent, rather than laminar [12].

2.4.2.3 RADIATIVE COMPONENT, h_{rad}

The radiative heat transfer coefficient is considered for high temperature gas-fluidized bed furnaces. Because of the nonlinear dependence of radiation on temperature, determining a suitable correlation that includes the two convection components, as well as the radiation component, becomes fairly complex; therefore, radiation effects are treated separately from the convective components and considered for bed temperatures greater than 600°C [1].

2.4.3 HEAT TRANSFER CORRELATIONS FOR IMMERSED SURFACES

Heat transfer to immersed tubes has been studied by a number of researchers, but mainly in the context of boiler size tubes ($d_s > 25.4mm$) as discussed earlier. Many factors, including size and shape of tubes, the location of the tube in the bed, their orientation, particle properties, gas properties, etc. all influence the magnitude of the bed-to-surface heat transfer coefficient; therefore, the following correlations have been developed to predict the total average heat

transfer coefficient, h_{avg}, for smooth horizontal tubes immersed in a fluidized bed of small particles [1].

Vreedenberg [5]:

$$Nu = 420\left[\left(\frac{Gd_s\rho_p}{\rho_g\mu_g}\right)\left(\frac{\mu_g^2}{d_p^3\rho_p^2 g}\right)\right]^{0.3} Pr^{0.3} \tag{2.14}$$

Andeen and Glicksman [6]:

$$Nu = 900(1-\varepsilon)\left[\left(\frac{Gd_s\rho_p}{\rho_g\mu_g}\right)\left(\frac{\mu_g^2}{d_p^3\rho_p^2 g}\right)\right]^{0.326} Pr^{0.3} \tag{2.15}$$

Grewal and Saxena [7]:

$$Nu = 47(1-\varepsilon)\left[\left(\frac{Gd_s\rho_p}{\rho_g\mu_g}\right)\left(\frac{\mu_g^2}{d_p^3\rho_p^2 g}\right)\right]^{0.325}\left[\frac{\rho_p C_{ps} d_s^{\frac{3}{2}} g^{\frac{1}{2}}}{k_g}\right]^{0.23} Pr^{0.30} \tag{2.16}$$

Petrie *et al.* [8]:

$$Nu = 14\left(\frac{G}{G_{mf}}\right)^{\frac{1}{3}} Pr^{\frac{1}{3}}\left(\frac{d_s}{d_p}\right)^{\frac{2}{3}} \tag{2.17}$$

Gelperin *et al.* [17]:

$$Nu = 4.38\left[\frac{1}{6(1-\varepsilon)}\left(\frac{Gd_p}{\mu_g}\right)\right]^{0.32}\left(\frac{1-\varepsilon}{\varepsilon}\right)\frac{d_s}{d_p} \tag{2.18}$$

The Nusselt number is based on the outside tube diameter, d_s, (sample diameter) defined as:

$$Nu = \frac{h_{avg} d_s}{k_g} \tag{2.19}$$

and the gas Prandtl number is defined as:

$$Pr = \frac{\mu_g C_{pg}}{k_g} \tag{2.20}$$

The gas and solid particle properties are described below:

C_{pg} = Specific heat of fluidizing gas at constant pressure

C_{ps} = Specific heat of solid particles at constant pressure

μ_g = Gas viscosity

k_g = Gas thermal conductivity

Figure 2.5 illustrates the above correlations for typical conditions.

Equation (2.16) is quoted as "the only one that can successfully represent all the available data in the literature not employed in its development within an uncertainty of ±25%" [1]. Taking a look at Equation (2.16), it contains all the expected relevant parameters, including a volumetric heat capacity term of the solid particles, $\rho_p C_{ps}$ appearing in the dimensionless group $\frac{\rho_p C_{ps} d_s^{\frac{3}{2}} g^{\frac{1}{2}}}{k_g}$, not present in most other correlations. Furthermore, the bed voidage is given by:

$$\varepsilon = \frac{1}{2.1}\left[0.4 + \left\{4\left[\frac{\mu_g G}{d_p^2\left(\rho_g\left(\rho_p - \rho_g\right)\right)\varphi_s^2 g}\right]^{0.43}\right\}^{\frac{1}{3}}\right] \tag{2.21}$$

Equation (2.21) is a function of the gas mass flow rate and the non-dimensional sphericity term, presented in Table 2.1 for different types of particles. The gas property μ_g is also present, suggesting the bed voidage, to some degree, is affected by its value. Kunii *et al.* [18] reported an 8% increase in ε for furnace temperatures up to 500°C in beds of fine particles.

2.4.4 THE EFFECT OF SHAPE OF THE IMMERSED BODY

The shape of the immersed body has an influence on the local circulation of particles close to it, affecting the surface-to-bed heat transfer behaviour. Gas voids and particle contact time are parameters greatly influenced by the shape [2] which are also important factors for good heat transfer.

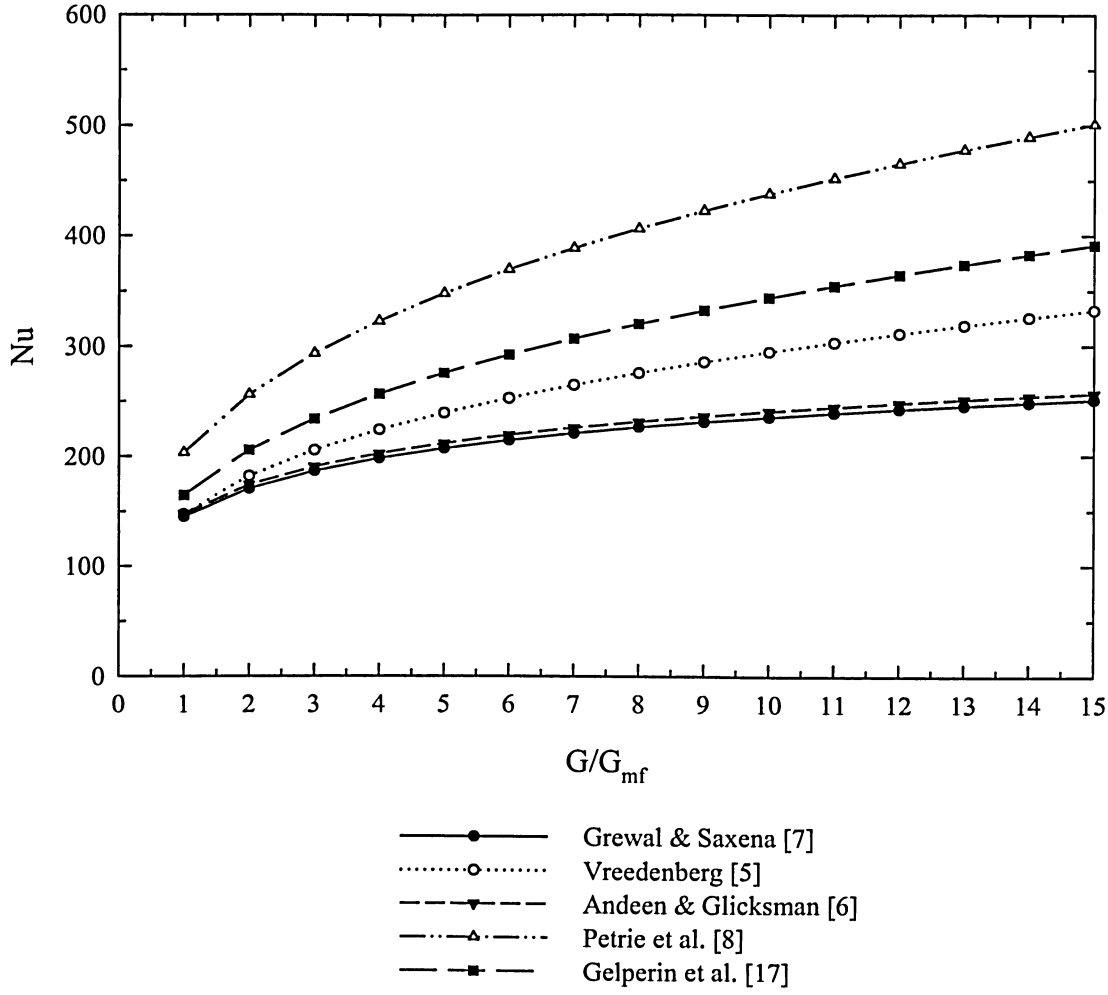

Figure 2.5 – Predicted Nusselt Number for Standard Correlations for Typical Conditions

CHAPTER THREE

EXPERIMENTAL APPARATUS

3.1 LAB SCALE FLUIDIZED BED

The lab-scale fluidized bed unit used for this research is shown in Figure 3.1. Its active bed area is 311mm (12¼") in diameter with an overall height of 915mm (36"). A schematic cross section of the apparatus is illustrated in Figure 3.2. The shell of the unit is cylindrical in shape and made of stainless steel with 6.35mm (¼") thick walls. It is bolted onto a 622mm (24½") square plenum 457mm (12½") from the floor. Fluidizing air is introduced through the center bottom of the plenum at the desired fluidizing rate. The fluidizing air enters the plenum and is distributed evenly into the bed by a 305mm x 305mm x 25.4mm (1' x 1' x 1") thick porous fused alumina hearth tile mounted flush with the top of the base. There is a 6.35mm (¼") clearance all around between the tile and the steelwork which is filled with high temperature grout to hold the tile in place. The tile has a porosity of 64% and provides a very even gas distribution. The sample holder is held in place by a pin and steel block assembly bolted on the top flange of the bed unit. The sample holder is discussed in detail in Section 3.3. A cone made of sheet metal is placed on the top opening of the unit (not shown in Figure 3.1) to collect any sand that is blown out the top of the bed unit.

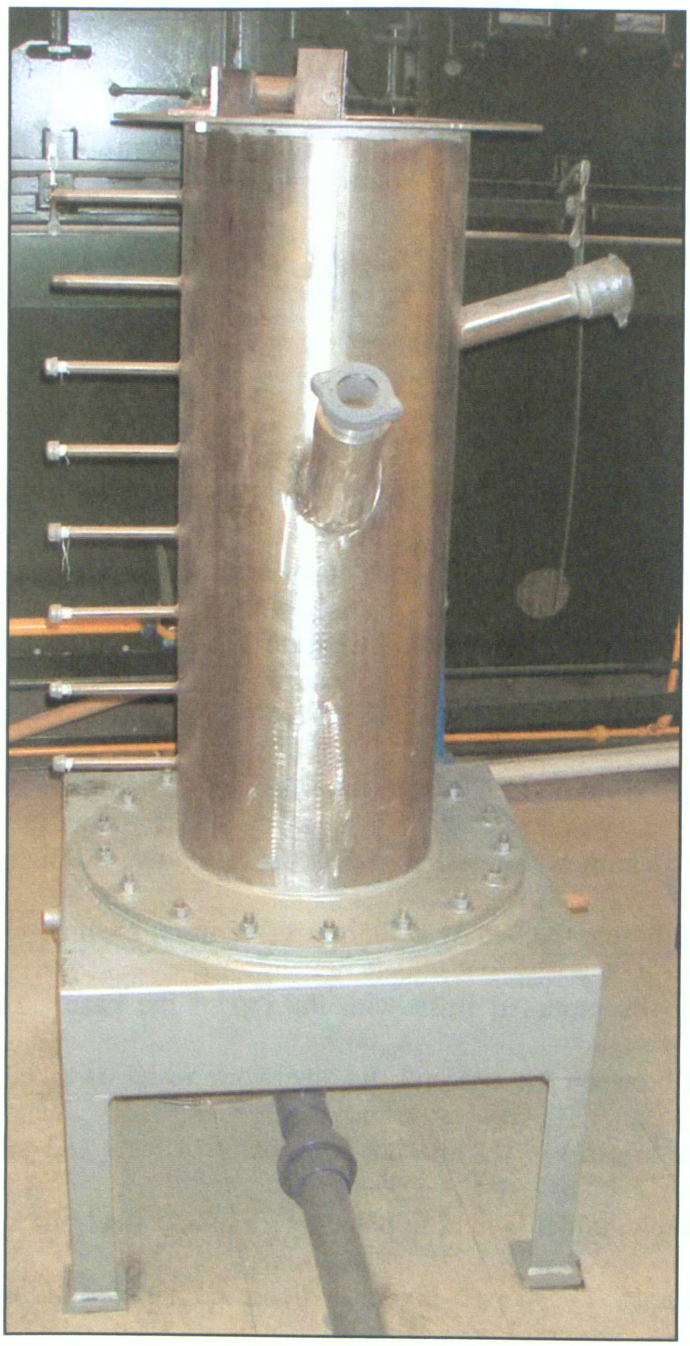

Figure 3.1 – Lab Scale Fluidized Bed Apparatus

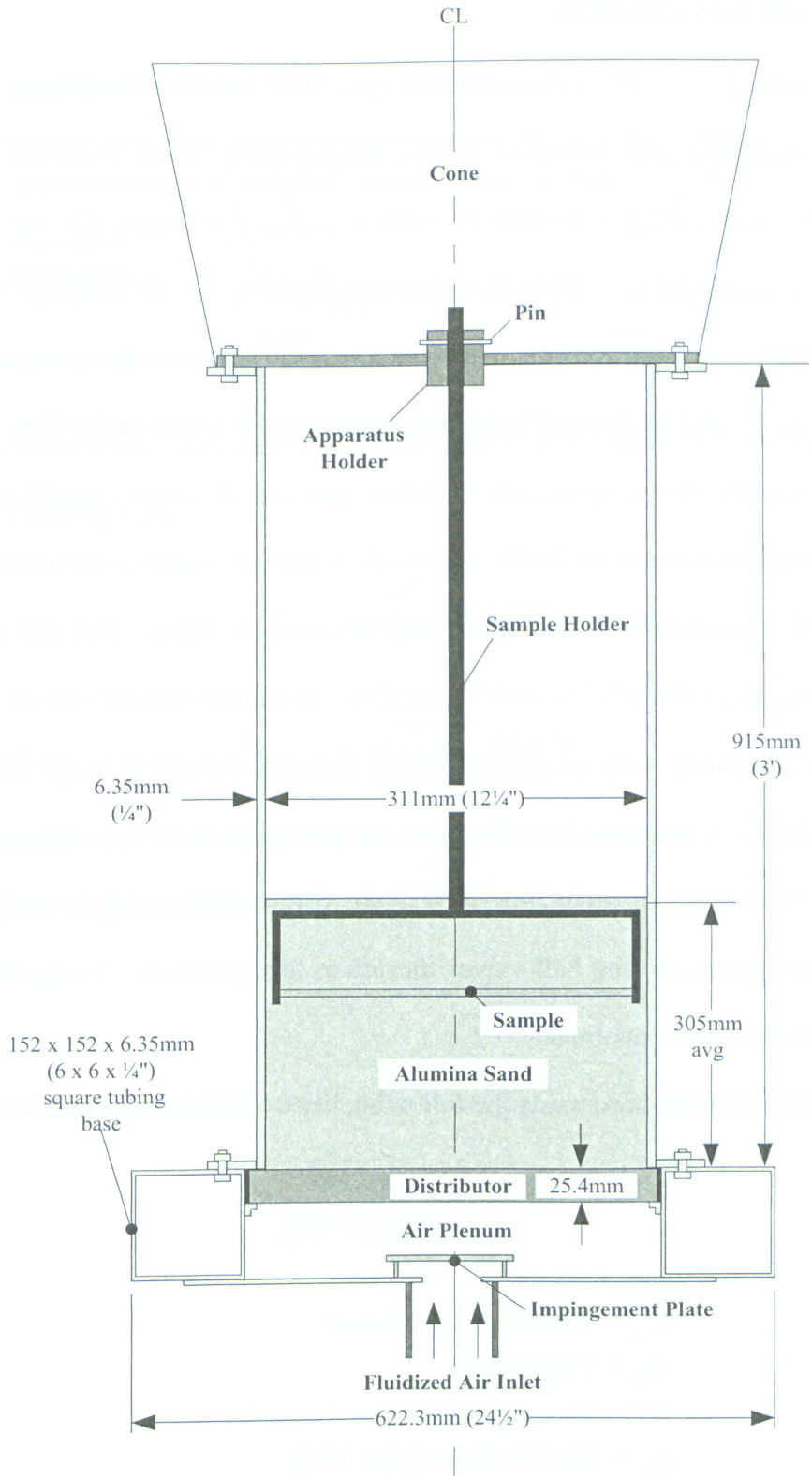

Figure 3.2 – Schematic Cross-Section of Lab Scale Fluidized Bed with Immersed Sample

3.2 AIR DELIVERY SYSTEM

Air is supplied by a Spencer centrifugal type 3005 blower driven by a 3.8kW (5HP), 3490RPM electric motor. The blower is capable of delivering 229m^3/hr (135SCFM) of air at 21kPa (3.0PSIG). The schematic air delivery system is shown in Figure 3.3. It is configured to supply the fluidized bed unit with an air flow rate ranging from 5 to 187m^3/hr (3-110CFM). Air flows from the blower outlet into a 102mm (4") PVC pipe, which acts like a manifold delivering air to a 63.5mm (2½") and 25.4mm (1") pipe connected perpendicular to the flow direction. The 1" pipe flow path splits into two paths; the first flow path provides flow rates from 5 to 21 m^3/hr (3-21CFM) using a rotameter while the second flow path provides a maximum flow rate of 48m^3/hr (28CFM) measured by a manometer and venturi flow meter. The 2½" pipe flow path provides flow rates from 46 to 187m^3/h (27-110CFM). A manometer and venturi are used when smaller flow rate increment readings are needed, but they are unstable at larger flow rates (above 85 m^3/h or 50CFM). A Magnehelic differential pressure gage is used to measure higher flow rates in increments of approximately 10m^3/h (6CFM). The air path and flow rates are controlled by manually opening and closing ball valves located at four positions. Using this method, the desired fluidizing rate can be attained.

Flow rates were calculated using the following basic Venturi flow equation:

$$Q = C_v A_T \sqrt{\frac{2\Delta P}{\rho_g \left(1-\beta^4\right)}} \tag{3.1}$$

where,

C_v = Discharge Coefficient
A_T = Throat Area
ΔP = Pressure Difference Across Venturi
ρ_g = Gas/Air Density (at inlet)
β = Throat-to-Pipe Diameter Ratio

Table 3.1 – Venturi Specifications

	1" Venturi	2½" Venturi
C_v	0.9797	0.9797
d_T - throat diameter (mm/in)	19.05/0.750	33.35/1.313
d_{in} - pipe diameter (mm/in)	25.4/1.00	62.71/2.469
A_T (mm^2/in^2)	285.2/0.442	873.5/1.354
β	0.5628	0.2828

Simplifying the known venturi variables shown in Table 3.1, Equation (3.1) can be written as a function of ΔP ("H_2O) given by:

$$Q_{1"} = 80\sqrt{\frac{\Delta P}{34}} \quad \text{(SCFM)} \tag{3.2}$$

$$Q_{2\frac{1}{2}"} = 150\sqrt{\frac{\Delta P}{14.7}} \quad \text{(SCFM)} \tag{3.3}$$

The above equations approximated the air flow rates of their respective venturi. Uncertainties associated with the measured flow rate are discussed in Chapter 7.

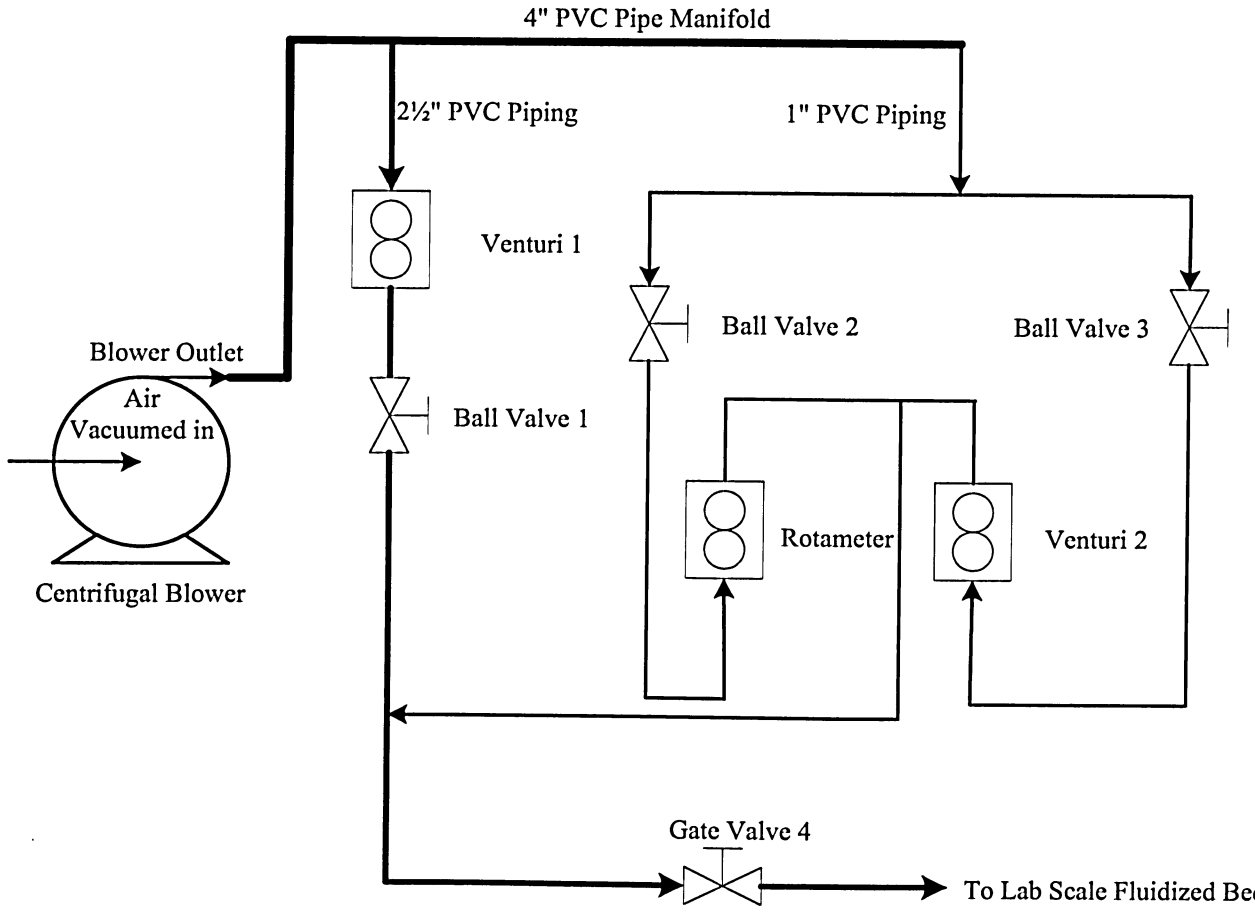

Figure 3.3 – Schematic of the Air Delivery System

3.3 SAMPLE APPARATUS

Two sample geometries were used in the experiment. They are described more fully in subsequent sections.

3.3.1 SMALL CYLINDER APPARATUS

The sample cylinder tubes were made of stainless steel and varied in outside diameter from 1.27 to 9.53mm (0.05-0.375") with a wall thickness ranging from 0.254 to 1.7mm (0.01-0.07"). Each sample was supported by a steel fixture illustrated in Figure 3.4. The fixture shaft was made of 19mm (¾") steel square tubing with a bracket welded at the bottom of the tube. At each end of the bracket a 12.7mm hole was drilled to hold the plastic inserts. The inserts provided support for the sample cylinder and electrically and thermally insulated the cylinder and the copper terminals from the steel bracket. Copper mechanical lugs were used as terminals on both sides of the cylinder. Each lug had a screw that sandwiched the terminal T/C and high current wires to the sample cylinder at each end. Figure 3.5 illustrates the terminal assembly. The electrical heat generating system is discussed later in the report. The high current cables were clamped with a screw and bolt to the copper terminals using tinned copper lug wire connectors. The connector sizes were determined by the electrical cable used. For larger samples, larger copper terminals and cables were needed to handle the supplied current. The two dissimilar metal leads of the sample center T/C was spot welded at their joint tip and insulated with electrical tape before being fed inside the tube. The electrical or thin clear tape protected the T/C from accidentally touching the tube wall, where grounding effects caused noise in the readings due to metal to metal contact and ground problems in the lab. Silicon sealed the plastic ends making sure no air flow entered the tube. All the wires were securely taped along the

bracket and along the tube shaft. A type K T/C probe was attached along the shaft of the sample apparatus and bent away from the sample cylinder (approximately 75mm) to monitor the bed temperature in the vicinity of the sample. The thermocouple setup is discussed in detail in Section 3.5.1.

3.3.2 FLAT STRIP APPARATUS

The flat strip apparatus is shown in Figure 3.6. The sample flat strips were made from a 24 gauge (0.61mm) stainless steel sheet laser cut to the correct geometry, illustrated in Figure 3.7. The flat strips varied in width, w_s, from 6.35 to 25.4mm (¼ - 1"). Each sample was supported by an aluminum fixture illustrated in Figure 3.8. The main shaft was made of 19mm (¾") aluminum square tubing. It was 915mm (36") in length with a 286mm (11¼") aluminum tube shaft (bracket) welded perpendicular at the bottom of the main shaft. Two aluminum plates holding the terminal assembly were screwed at each end of the bracket. The terminal assembly is illustrated in detail in Figure 3.8. The terminal assembly consisted of a 31mm (1¼") diameter by 19mm (¾") thick copper shaft and plastic sleeve. The terminal assembly was designed to rotate the flat strip sample from a horizontal position (0° - sample surface parallel to the bed) to a vertical position (90° - sample surface perpendicular to the bed) in 15° increments. Two screws located and clamped the sample to the top and bottom part of the copper terminal. The terminal T/C and high current wires were sandwiched between the sample and top part of the copper terminal. With the sample secure between the copper terminals the plastic sleeves were placed around the terminals and clamped to the desired orientation by screwing together the bottom portion of the aluminum plate with the top part. Figure 3.9 illustrates the terminal assembly. The high current cables were screwed to the outside face of the copper terminals. All the wires

were securely taped along the bracket and along the tube shaft. The thermocouple setup is discussed in detail in Section 3.5.1.

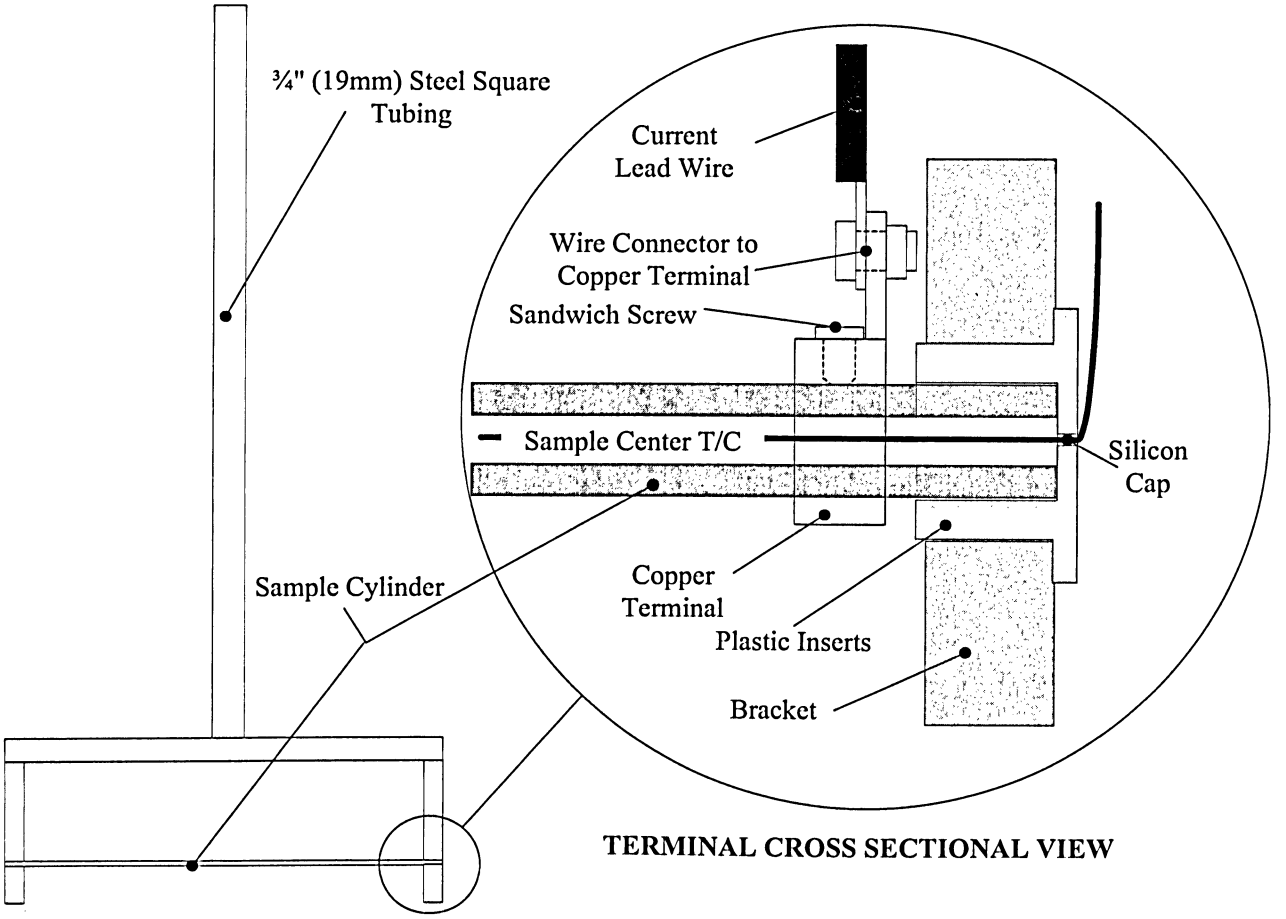

Figure 3.4 – Steel Fixture with Detailed View of Cylinder Terminal Assembly

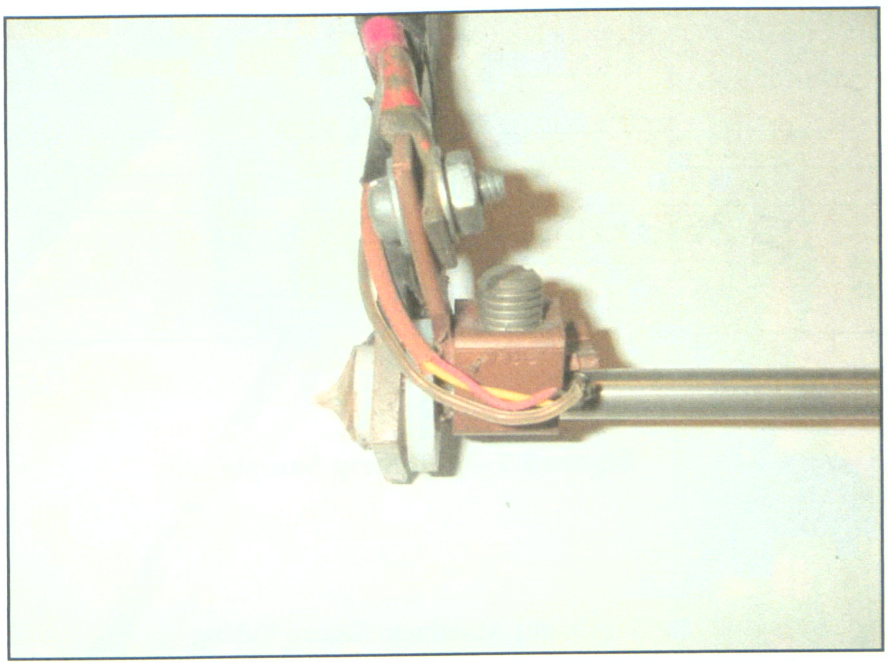

Figure 3.5 – Sample Cylinder Terminal Assembly

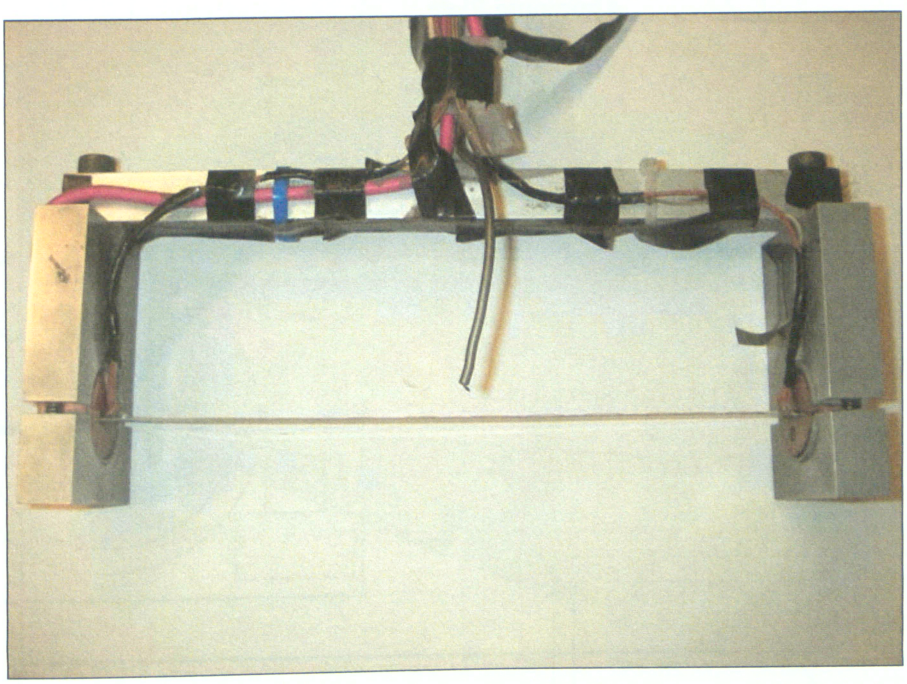

Figure 3.6 – Flat Strip Sample Apparatus

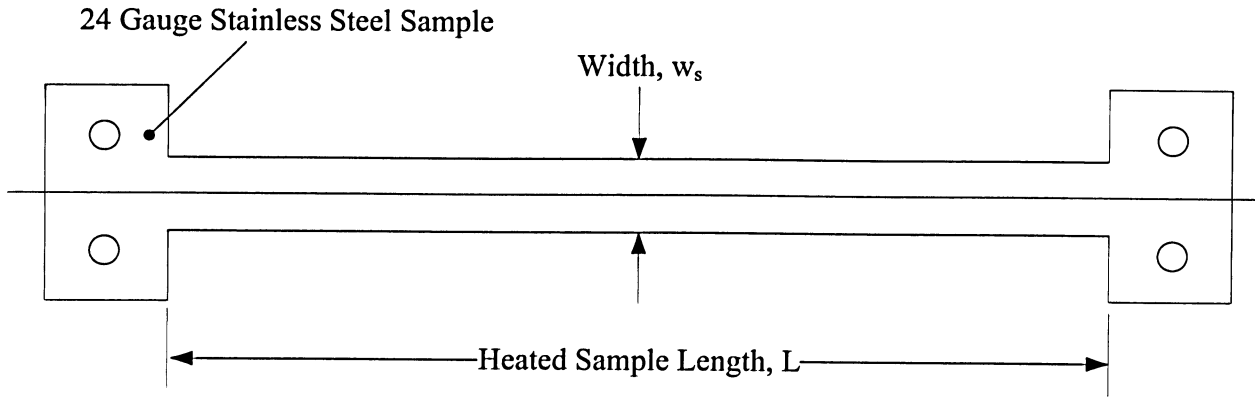

Figure 3.7 – Flat Strip Sample

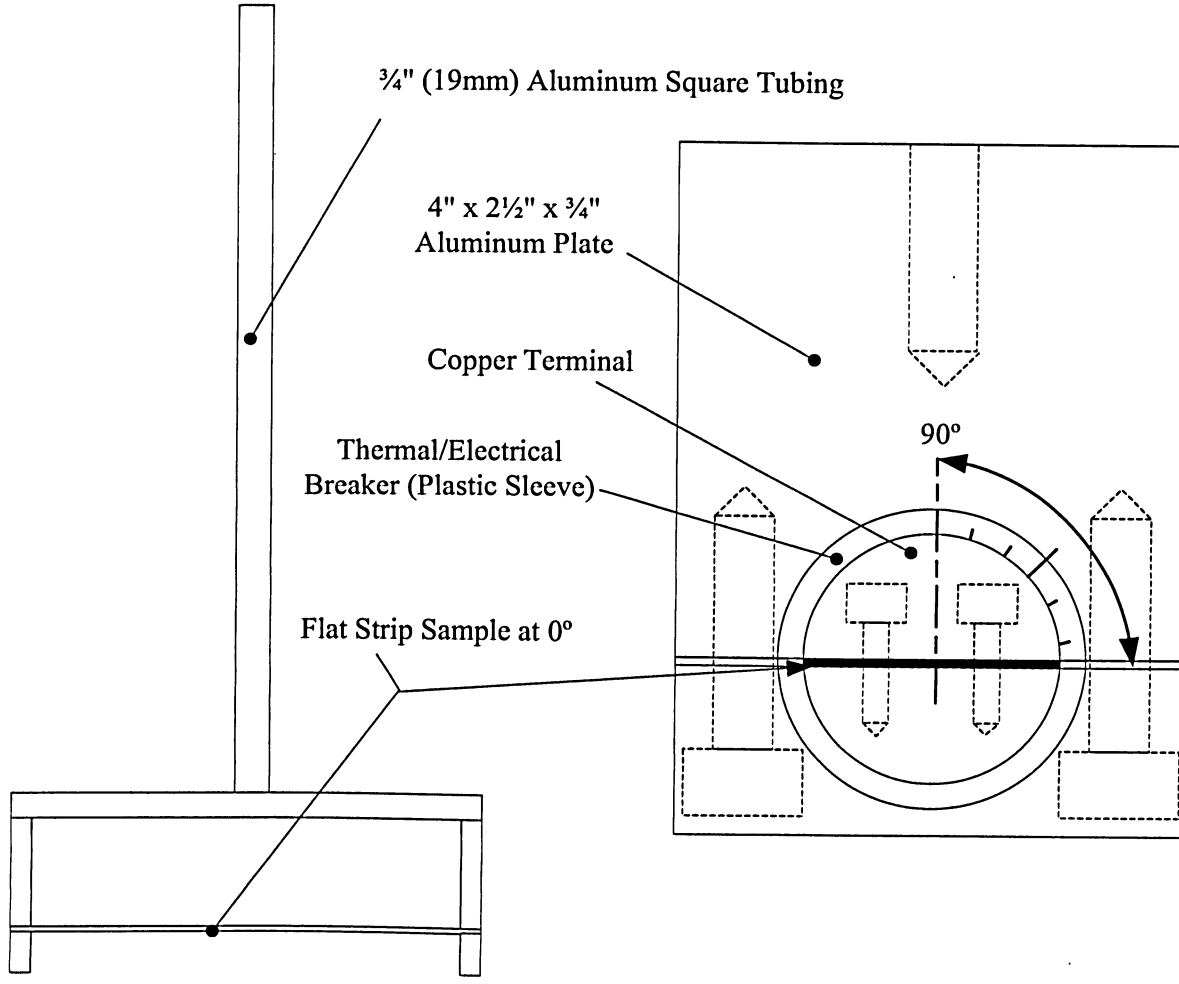

Figure 3.8 – Aluminum Fixture with Detailed View of Terminal Assembly

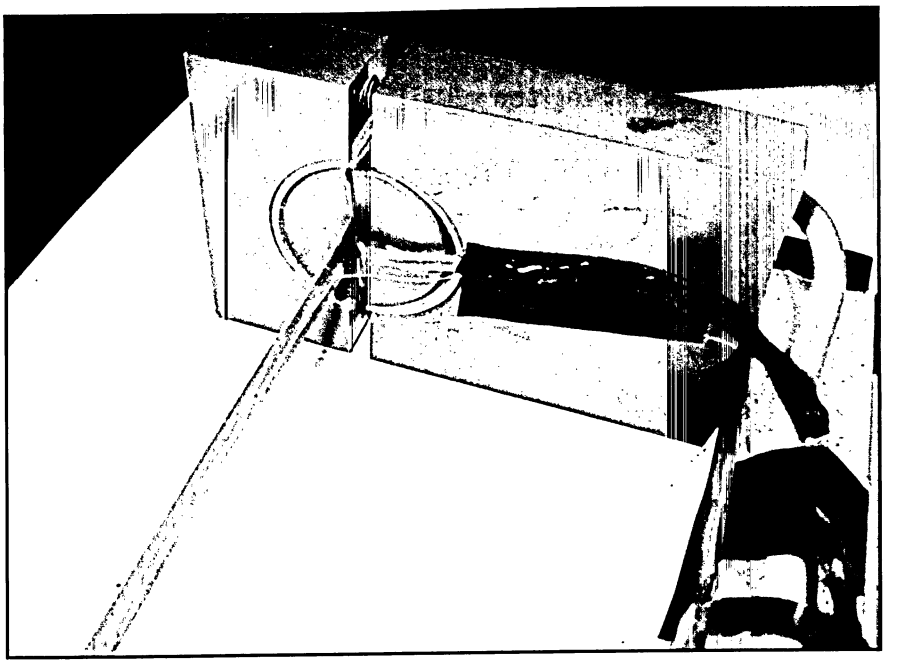

(a)

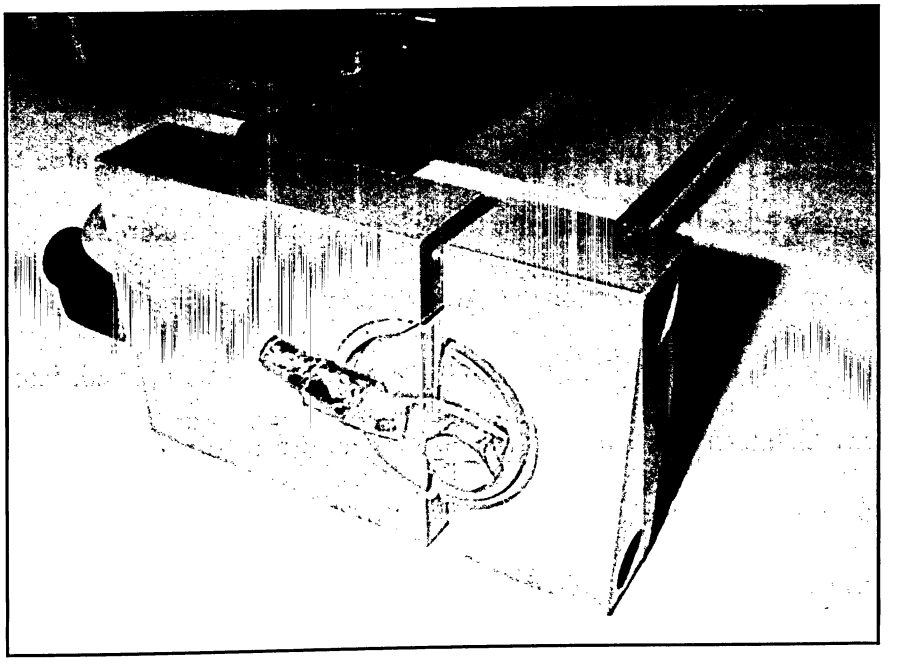

(b)

Figure 3.9 – Terminal Assembly (a) Front Side (b) Back Side

3.4 SAMPLE HEAT GENERATING SYSTEM

A schematic of the heat generating system used is illustrated in Figure 3.10. The current was supplied by a GW Instek® Programmable Power Supply model PSH-10100, capable of providing up to 100A at up to 10VDC. The power required to resistively heat the samples was calculated by:

$$P_o = VI \tag{3.4}$$

where,

$$V = IR \tag{3.5}$$

$$R = \frac{\rho_{res} L}{A_c} \tag{3.6}$$

ρ_{res} ≡ 720 nΩ-m (resistivity of stainless steel)
L = Sample Length
A_c = Cross Sectional Area

The maximum power needed to resistively heat the 25.4mm flat strip sample positioned at 90° in a 90 Grit bed was determined to be 81W. The power supply used was able to supply enough current to resistively heat all of the samples to their required temperature.

A Sprecher+Schuh (S+S) model CA6-140 relay was activated using a manual trigger (on/off switch). With the manual trigger ON, the S+S relay was opened, isolating the sample from any electrical interference (noise) when temperature readings were made. Current was supplied to the sample with the manual trigger set to the OFF position, closing the S+S switch. Two high current cables were connected to the large copper terminals at each end of the sample. These copper terminals also acted as effective heat sinks, removing heat from the samples at each end. The samples were resistively heated by providing the necessary current to raise the

sample temperature approximately 15°C above the bed temperature. A Digital Multimeter model GDM-8145 was used to read the voltage drop across the sample.

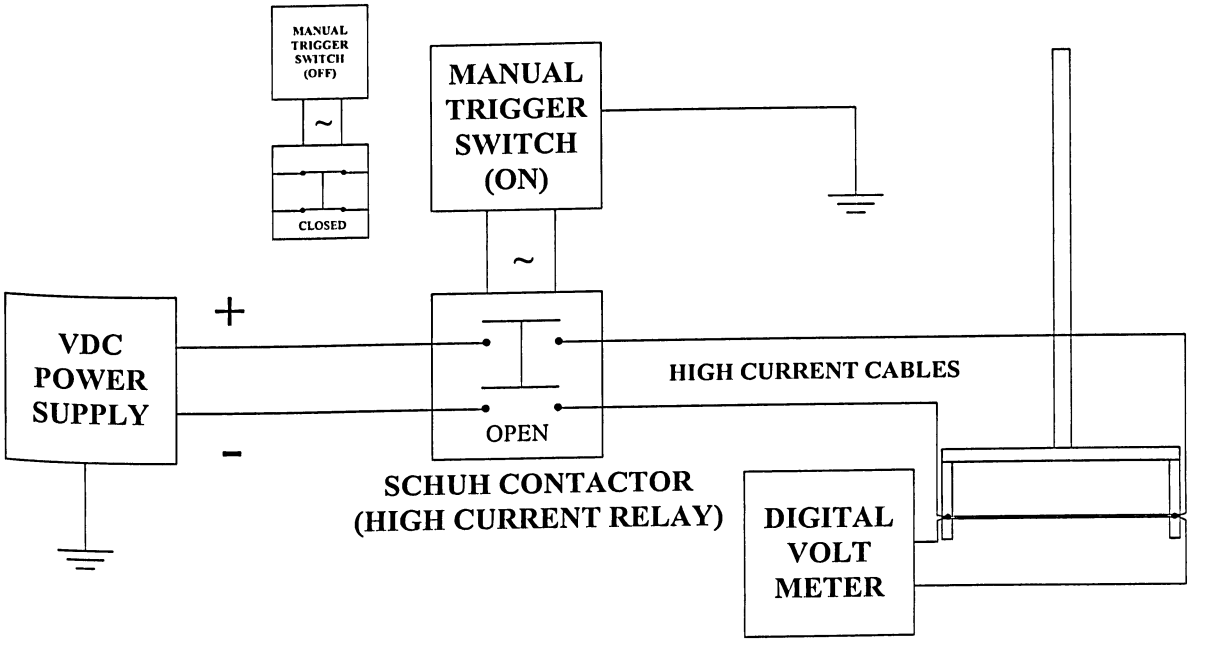

Figure 3.10 – Schematic of the Heat Generating System

3.5 TEMPERATURE MEASUREMENT DEVICES

The components used to measure temperatures are discussed below.

3.5.1 THERMOCOUPLE SETUP

Figure 3.11 illustrates the typical T/C setup for each sample apparatus. Type K T/C's (model TT-K-24-SLE) were used to measure temperatures at three locations. At each end of the sample, the two dissimilar T/C wires were twisted and sandwiched to the sample by the copper terminals. The bed T/C was insulated with M_gO and fixed in a stainless steel sheath allowing it to be bent to position. Again, the two dissimilar T/C wires were twisted and spot welded together. It was secured along the main shaft of the apparatus with electrical tape and bent into position approximately 75mm parallel to the sample center. The fourth measured temperature was the sample center temperature. The two geometries had different setups and are discussed in detail further into this section.

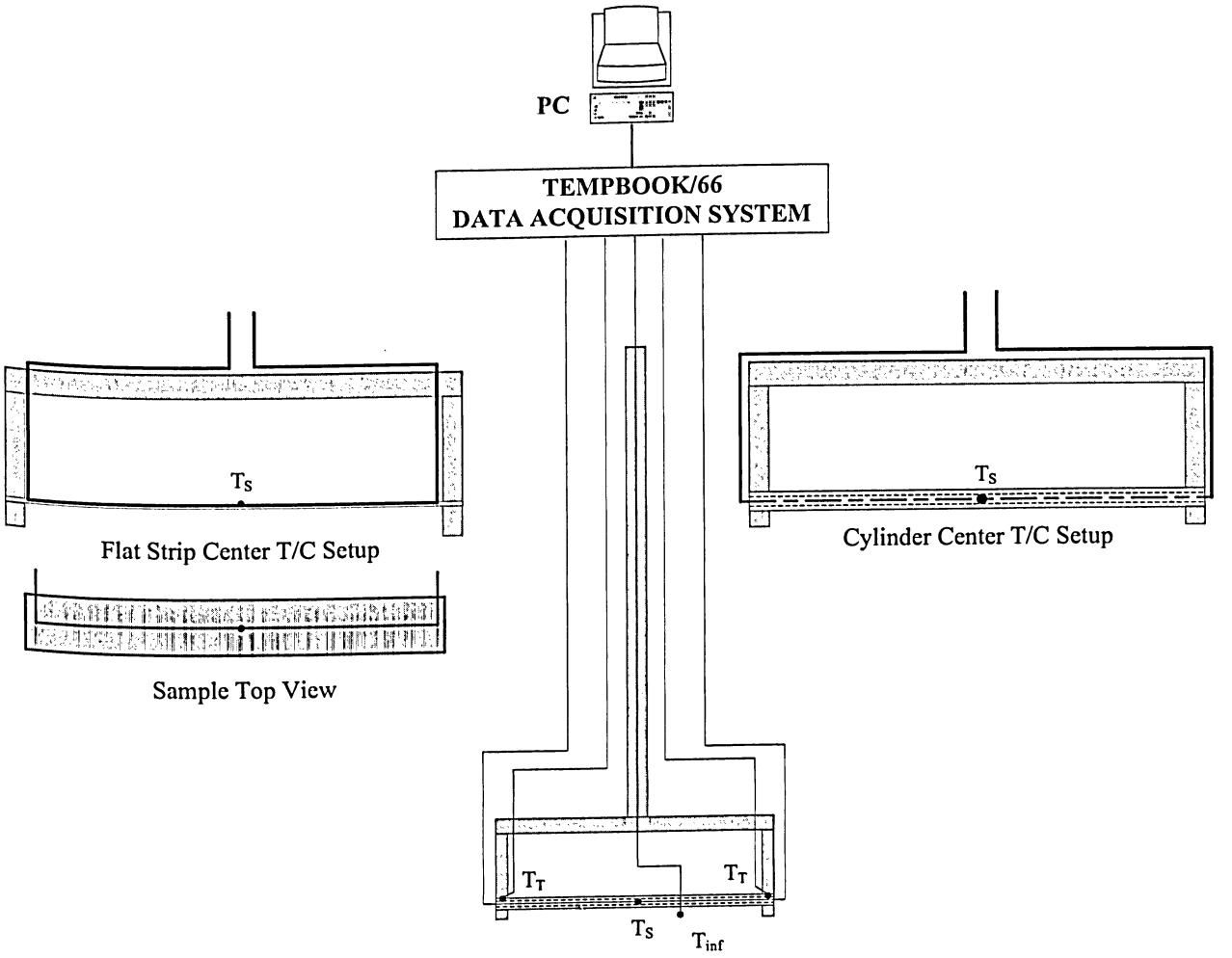

Figure 3.11 – Temperature Measuring Components and Thermocouple Setup

3.5.1.2 SMALL CYLINDER CENTER THERMOCOUPLE SETUP

To avoid temperature errors due to the "fin" effect caused by heat conduction out the thermocouple wire, particularly for the smaller samples, the sample center T/C was located inside the tube along the centerline. The lead T/C wires were twisted and spot welded together. The junction was insulated with thin clear tape and positioned inside at the center and middle of the tube. A simple correction to account for temperature drop from the tube inside wall to the outside wall was used, based on a 1-D steady state heat conduction model as shown below. The steady state, 1-D conduction equation with generation is given by:

$$\frac{1}{r}\frac{d}{dr}\left(r\frac{dT}{dr}\right) + \frac{q'''}{k} = 0 \qquad (3.7)$$

Solving Equation (3.7) and applying the following boundary conditions:

At $r = r_i$, $\frac{dT}{dr} = 0$ No heat transfer to inside of tube.

At $r = r_i$, $T(r_i) = T_s$ Known inside tube surface temperature .

The resulting expression for the outside tube temperature is given by:

$$T(r_o) = \frac{-q'''}{4k}\left(r_o^2 - r_i^2\right) + \frac{q'''r_i^2}{2k}\ln\left(\frac{r_o}{r_i}\right) + T_s \qquad (3.8)$$

The temperature difference between the inside of the tube and outside wall temperature was evaluated to be less than 0.5°C for all samples tested. Smaller thermocouples (0.08mm diameter) were used for the smaller samples.

3.5.1.3 FLAT STRIP CENTER THERMOCOUPLE SETUP

To avoid conduction losses through the wire ("fin" effects), the smallest insulated type K thermocouple wire capable of withstanding the vigorous fluidized bed conditions was used

(Nominal wire diameter 0.08mm (0.003"), insulation thickness 0.076mm (0.003")). A thinner wire would reduce the heat conduction from the sample into the T/C. To further avoid heat conduction losses and to provide an isothermal condition along the T/C lead wires, the two dissimilar metals were crossed over one another and fused at their point of contact to the top center of the sample (creating a junction). The welding was performed using a Hotspot II T/C welder with a maximum rating of 300W. The welder was set in the range of 5 to 10W, depending on factors like wire diameter and location of the weld. To avoid convective cooling from the bed at the junction and to bond the loose wire along the center line of the sample a high thermal conductive chemical epoxy cement was used. Delta Bond 154 and an A4 Hardener were applied to keep the T/C wire from being ripped off the sample while immersed in the fluidized bed. The film was kept thin as possible to minimize bed flow interference.

3.5.2 DATA ACQUISITION SYSTEM

Experimental data were collected using the Iotech Tempbook/66 with DaqView software discussed in the following subsections.

3.5.2.1 HARDWARE SYSTEM

The hardware used for the temperature data acquisition was the Iotech TempBook/66. The TempBook was connected to a standard PC parallel port and transferred readings (directly to disk) at up to 100K readings/s. It provides 8 differential thermocouple inputs with temperature readings at up to 100kHz. It is powered by an AC adapter and features a hardware-based digital/TTL trigger that minimizes trigger latency to less than 10μs. The TempBook was calibrated prior to being used by the manufacturer and was quite accurate and easy to install.

Table 3.2 shows the accuracy of the hardware for different types of thermocouples. For example, using type K T/C to measure a temperature in the range of 0 to 100°C using the hardware, the TempBook would have an accuracy of ±1.5°C.

Table 3.2 – Temperature Specifications for TempBook/66 @ 0 to 50 °C

Thermocouple Type	Range (°C)	Resolution (°C)	Accuracy (°C)
K	-200(min) to 0	1.1	±2.4
	0 to 1260(max)	0.8	±1.5

3.5.2.2 SOFTWARE SYSTEM

The software used to record the experimental temperature data was DaqView V7.15.11, a 32-bit Windows-based data acquisition program. It is extremely adaptable and easy to use. It allows the recording of temperature data into various file types (ASCII, Matlab, Excel, etc.). The trigger source can be set to different settings (key hit, external TTL Rising/Falling) depending on the device and setup being used. The counter/timer can be configured for one of three modes for measuring frequency, totalizing, or generating pulse trains. Along with all the configurations available, the main window can display bar graph meters, analog meters, digital meters and charts for all the channels being used. The software setup used to record the data will be discussed further in Chapter 4.

DaqView was used to record the sample, bed and terminal temperatures of the cylinder and flat strips immersed in the fluidized bed. Reducing the recorded data by taking the average sample and bed temperatures, the heat transfer coefficient, h, can be calculated. The details of this calculation will be explained in Chapter 5.

CHAPTER FOUR

EXPERIMENTAL PROCEDURE

4.1 EXPERIMENTAL APPARATUS SETUP AND OPERATION

The experimental apparatus setup includes the lab scale fluidized bed, air delivery system, sample apparatus, data acquisition system and thermocouple setup described in Chapter 3. Their operations are discussed in the following sections.

4.1.1 FLUIDIZED BED AND AIR DELIVERY OPERATION

The lab-scaled fluidized bed was filled to a depth of approximately 305mm with fine aluminum oxide sand of #50 (330μm), 60 (254μm), 70 (203μm), 80 (165μm) and 90 (145μm) grit sizes. A heavy duty vacuum was used to empty the sand from the bed when changing between grit sizes.

All the ball valves were secured and closed prior to initial start-up. This ensured that the sand did not blow out of the fluidized bed unexpectedly when the blower was turned on. With the blower on, fluidizing rates were controlled by four valves as described in Section 3.2 and illustrated in Figure 3.3.

Table 4.1 summarizes the flow paths, flow rate ranges and delivery operation. The air delivery system was capable of delivering the required fluidizing rates at selected increments covering the entire fluidizing rate range of the respective grit being tested.

Table 4.1 – Air Delivery Operation

Flow Path	Measurement Device	Ball/Gate Valve 1	2	3	4	Flow rate Range (CFM)
1	Rotameter	Closed	Adjusted	Closed	Adjusted	3 – 21
2	Venturi 2	Closed	Closed	Adjusted	Adjusted	21 – 28
3	Venturi 1	Adjusted	Closed	Closed	Adjusted	27 – 110

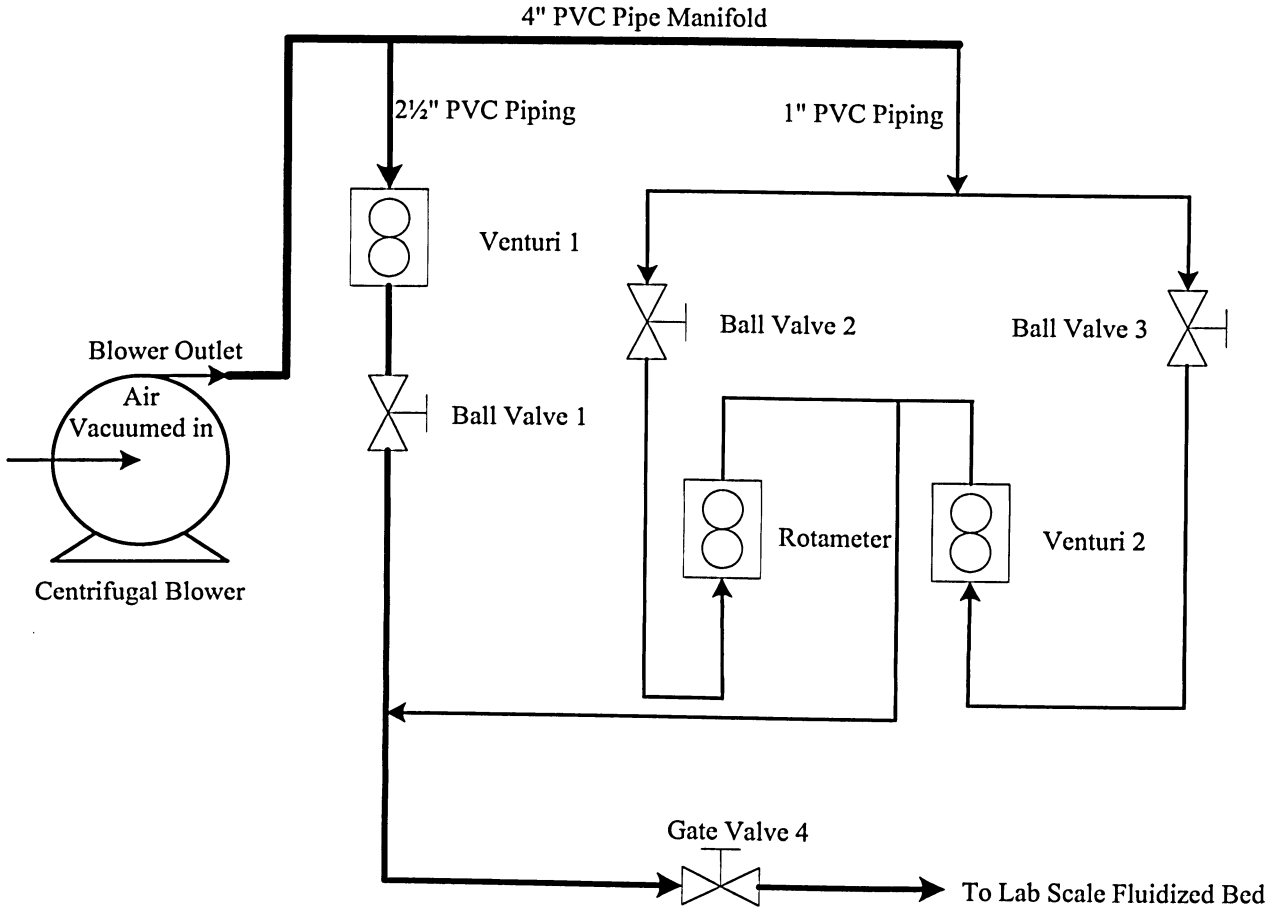

Figure 4.1 - Schematic of the Air Delivery System (Figure 3.3 reproduced)

The following table shows the typical range and increments of the flow rates measured and the devices used. Flow rates were calculated using Equations (3.2) and (3.3).

Table 4.2 – Range of Flow and Fluidization Rates

Measurement Device	ΔP ("H_2O)	Volume Flow Rate Q (CFM)	Mass Flow Rate $Q \cdot \rho_g$ (kg/s)	Fluidizing Gas Mass Flow Rate G(kg/m^2-s)
Rotameter 1" Flow Path		3	0.0017	0.0224
		4	0.0023	0.0298
		.	.	.
		.	.	.
		.	.	.
		21	0.0119	0.1566
Venturi 2 1" Flow Path	2.5	21.7	0.0123	0.1681
	3	23.8	0.0135	0.1772
	3.5	25.7	0.0146	0.1914
	4	27.4	0.0156	0.2047
Venturi 1 2½" Flow Path	0.5	27.7	0.0157	0.2063
	1	39.1	0.0222	0.2918
	1.5	47.9	0.0272	0.3574
	2	55.3	0.0314	0.4127
	3	67.8	0.0384	0.5054
	4	78.2	0.0444	0.5836
	5	87.5	0.0496	0.6525
	6	95.8	0.0544	0.7148
	8	110.7	0.0628	0.8253

4.1.2 SAMPLE HEAT GENERATING OPERATION

The sample was resistively heated by the heat generating system described in Section 3.4. The supplied current was adjusted by regulating the digital power supply from 2A for the smaller samples to 85A for the largest sample in available increments of 0.1A. The current was adjusted manually for each run. The voltage drop across the sample was displayed on the digital voltmeter and recorded. The volumetric heat generation was calculated by:

For small cylinders,

$$q''' = \frac{VI}{\pi\left(r_o^2 - r_i^2\right)L} \tag{4.1}$$

For flat strips,

$$q''' = \frac{VI}{w_s t_s L} \tag{4.2}$$

4.1.3 DATA ACQUISITION SETUP

Four Type K thermocouples were connected to the TempBook/66 data acquisition system. The temperatures were monitored but not recorded while the sample was being heated to steady state conditions. The S+S contactor and external manual trigger were used to isolate the sample from any grounding effects or electrical interference (noise). The S+S contactor was connected to the TempBook trigger source, sending an electrical pulse when the S+S was opened. The DaqView software was configured to start recording the temperature data by this electrical signal, activated by the manual trigger. This allowed the system to accurately start recording data within 10μs of turning the switch on. With the switch on, current was no longer provided to the sample. One thousand scan counts were recorded at a rate of 100 scans per second. The temperature measurements were recorded as an ASCII (.txt) and Matlab (.m) file. Once the temperature measurements were recorded the switch was turned back off and the current supply was restored. Figure 4.2 illustrates the temperature acquisition for a cylinder sample of 9.53mm diameter during preliminary test runs. As shown in the figure, the terminal temperature measurements were subject to grounding effects causing noise while the current was supplied to the sample. To stabilize the temperature readings the S+S contactor was opened by

the manual switch isolating the sample from the supplied current eliminating the noise, as shown in the figure after approximately 1.2 seconds. A typical experimental run would start recording temperatures at t = 0s. Figure 4.3 illustrates a typical experimental temperature acquisition. As shown, the grounding effects causing noise are eliminated by isolating the sample from the supplied current. This insures a more reliable data set. Once the temperature data were recorded after approximately ten seconds, the S+S contactor was closed, supplying current back to the sample.

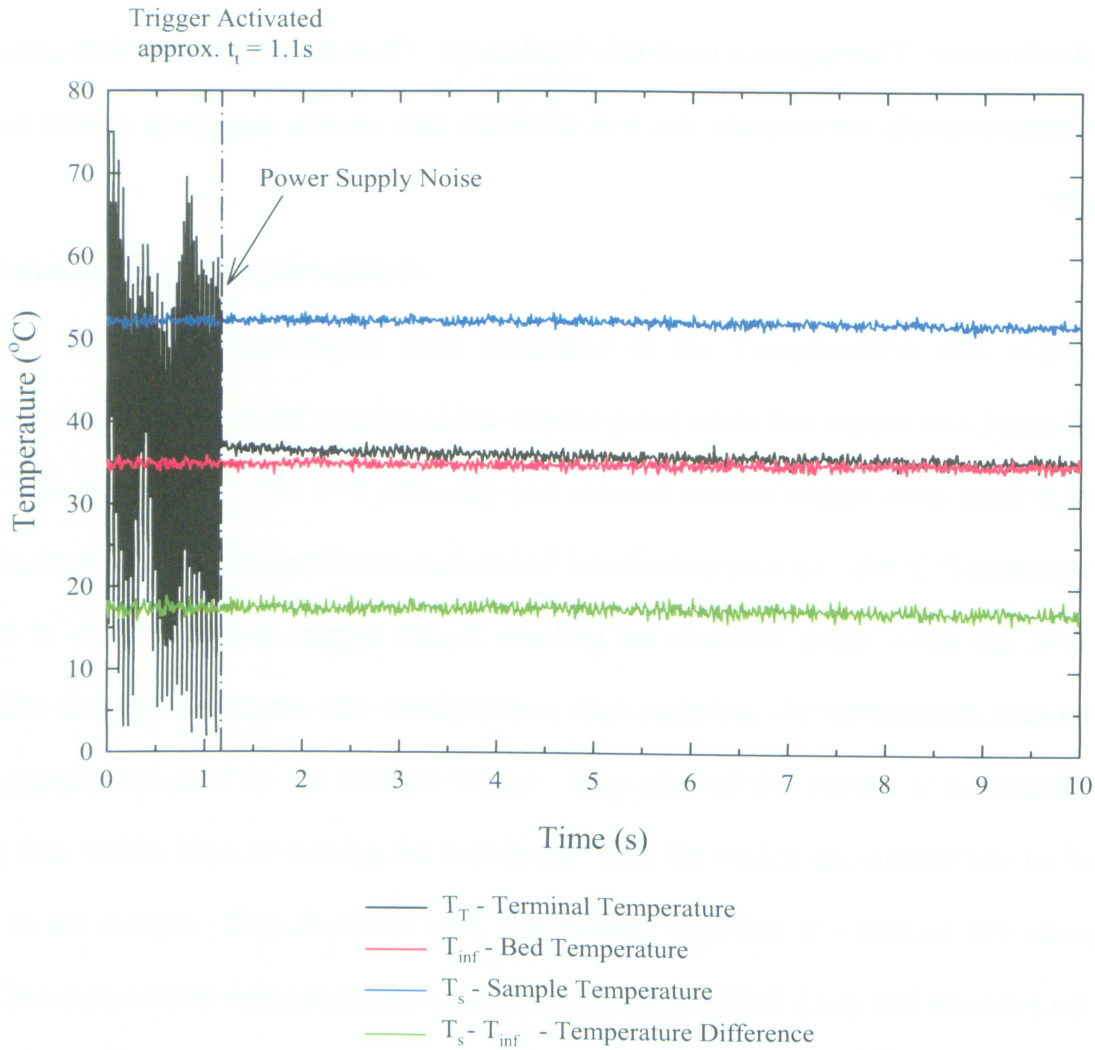

Figure 4.2 – Temperature Acquisition for a Preliminary Test Run of a 9.53mm Cylinder Sample

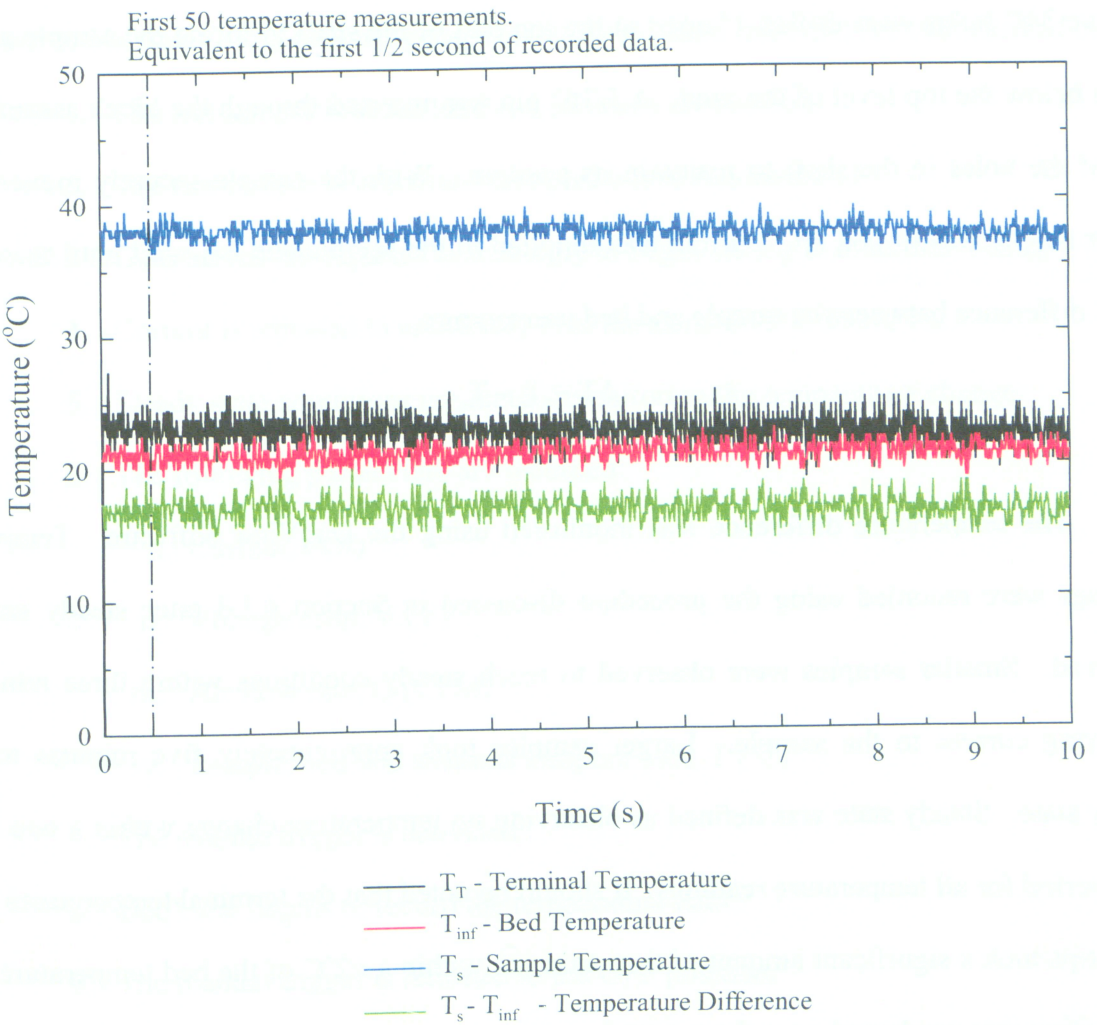

Figure 4.3 – Temperature Acquisition for a Typical Test Run for all Samples

4.1.4 SAMPLE SETUP

All the wires were connected and secured along the shaft of the holder. The bed of sand was fluidized in order to immerse the sample. The bed was then returned to packed bed conditions and the sample was positioned approximately 120mm below the top of the bed. Twelve 3/8" holes were drilled 1" apart at the top part of the shaft to locate the sample a certain depth below the top level of the sand. A 5/16" pin was inserted through the block assembly and one of the holes in the shaft to maintain its position. With the sample securely immersed the power supply was turned on. Current was supplied to the sample and adjusted until there was a 15 °C difference between the sample and bed temperature.

$$\Delta T = T_s - T_\infty$$
$$\Delta T \approx 15°C \tag{4.3}$$

The temperature difference was monitored using the DaqView software. Temperature readings were recorded using the procedure discussed in Section 4.1.3 once steady state was observed. Smaller samples were observed to reach steady conditions within three minutes of supplying current to the sample. Larger samples took approximately five minutes to reach steady state. Steady state was defined as observing no temperature change within a two minute time period for all temperature readings. It should be noted that the terminal temperatures for the flat strips took a significant amount of time to reach within a ±2°C of the bed temperature. Data acquisition was conducted once these criteria were met.

4.2 EXPERIMENTAL STEPS AND TEST MATRIX

The experiment was carried out in ambient bed temperature conditions. In this work, the heat transfer coefficient was evaluated using steady state temperatures of the sample (T_s), the terminal temperatures (T_T) and the bed (T_∞). The derivation of the heat transfer coefficient is discussed in Chapter 5. The following steps taken during each test (run) are summarized below:

1. The test sample is assembled and all wires are secured.
2. The test sample is immersed into position in fluidized bed.
3. Gate valves are adjusted accordingly to begin testing at minimum G/G_{mf}.
4. Current is adjusted to resistively heat the sample 15°C above T_∞.
5. Steady state conditions are met by monitoring the temperature change.
6. The following parameters are recorded:
    i. Current, I (A)
    ii. Voltage drop, V (V)
    iii. Air flow rate, Q (CFM)
    iv. Sample, bed and terminal temperatures, T (°C)
7. The manual trigger is activated.
8. DaqView begins to record the temperature data.
9. The manual trigger is returned to the OFF position.
10. Ball valves are adjusted to increase G/G_{mf} at the desired increment.
11. Steps 4 - 10 are repeated up to the maximum G/G_{mf}.
12. The test sample or sand is changed. Steps 1 – 11 are repeated.

Two geometries were tested. Approximately 3500 individual tests were performed. The following tables summarize the tests performed.

Table 4.3 – Test Summary for Small Cylinders

Cylinder Diameter (mm)	Grit Size	G/G_{mf}
1.27, 2.11, 3.18, 4.76, 6.35, 7.94, 9.53	50	0.14 – 5
	60	0.22 – 8.5
	70	0.34 – 14
	80	0.5 – 15
	90	0.64 – 22

Table 4.4 – Test Summary for Flat Strips

Flat Strip Width (mm)	Grit Size	Orientation (Degrees)	G/G_{mf}
6.35, 9.53, 12.7, 25.4	50	0, 15, 30, 45, 60, 75, 90	0.14 – 5
	60	0, 15, 30, 45, 60, 75, 90	0.22 – 8.5
	70	0, 15, 30, 45, 60, 75, 90	0.34 – 14
	80	0, 15, 30, 45, 60, 75, 90	0.5 – 15
	90	0, 15, 30, 45, 60, 75, 90	0.64 – 22

4.3 DATA PROCESSING

Processing the experimental data followed the block diagram illustrated in Figure 4.4. The temperature data were recorded by the DaqView software as an ASCII text file and entered into the Mathcad program. The temperature data were reduced by taking the average of the first fifty readings (0.5s). The reason for this was because the temperature for smaller samples decreased to the bed temperature within the time frame of the temperature acquisition; therefore, the average of the first fifty readings, corresponding to the first half second, would be a better representation of the steady state temperatures. Figure 4.5 illustrates the captured temperatures for the first half second for the smallest cylindrical sample tested (d_s = 1.27mm) for two runs in different grit. This sample decreased to the bed temperature the fastest and would represent the worst case of all the samples tested. As shown in the figure the temperature average for each 0.1s interval deviated from the mean by approximately ±1.2°C for both cases. This shows that the error is relatively small compared to the noise in the first 0.5s and does not decrease significantly in the first half second time frame.

The Mathcad program calculated the heat transfer coefficient, h, and film temperature, T_{film}, defined in Chapter 5. These values were inputted into an Excel file where Nu_{exp} vs. G/G_{mf} plots were generated. For each test run a mean Nusselt number, Nu_{mean}, was evaluated. Chapters 5 and 6 discuss the data analysis and results in more detail.

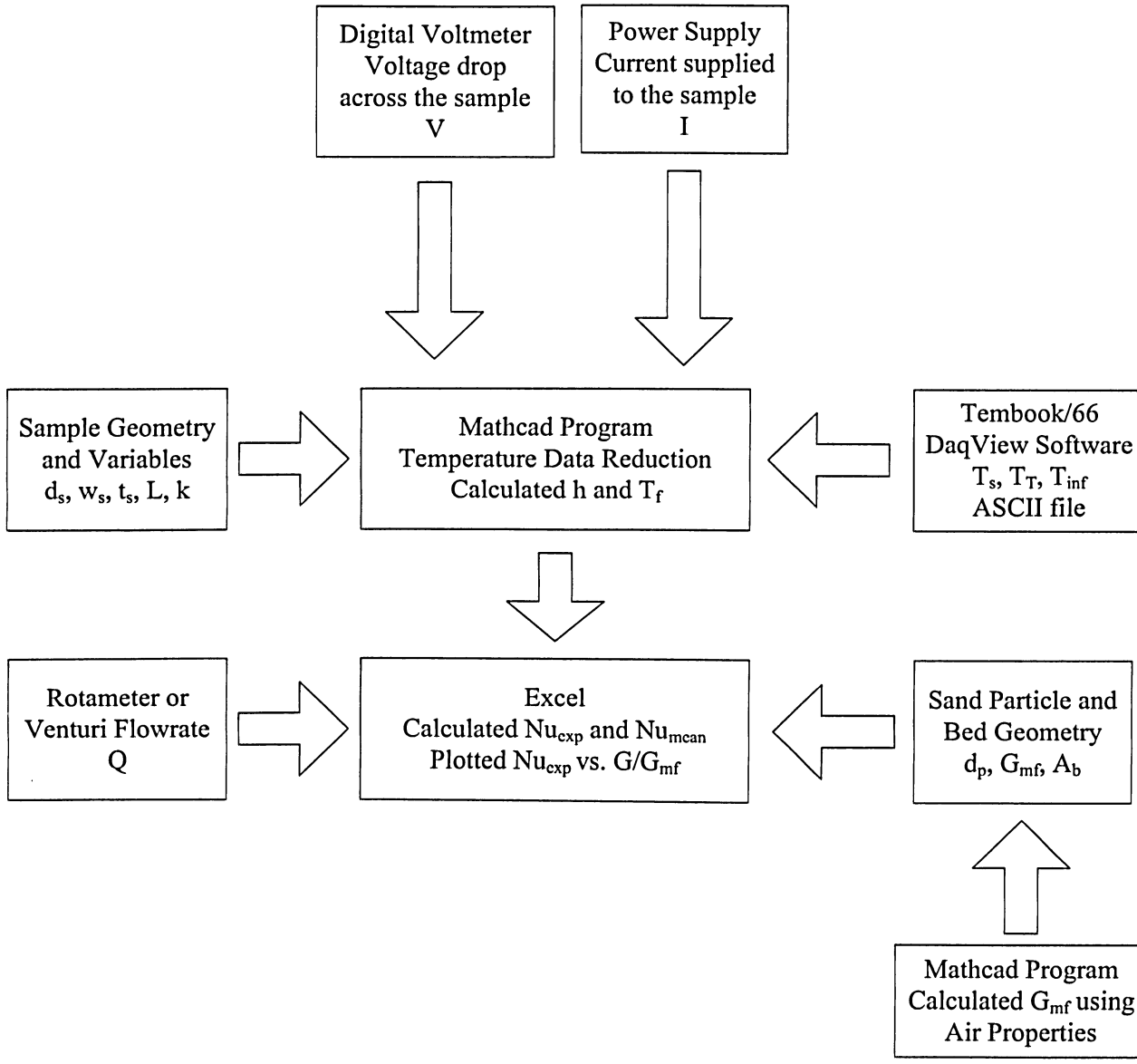

Figure 4.4 – Data Processing Block Diagram for an Experimental Run

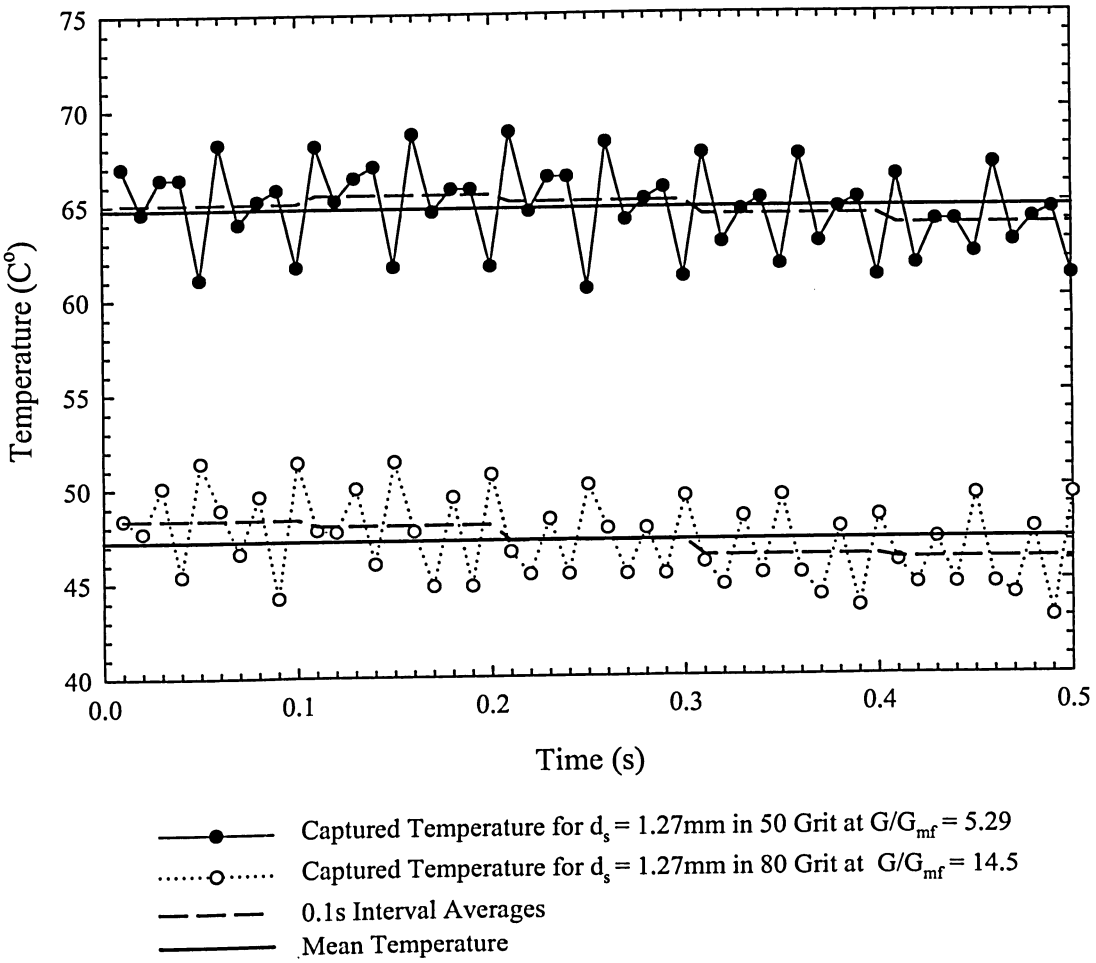

Figure 4.5 - Captured Temperatures for d_s = 1.27mm for Two Experimental Runs

CHAPTER FIVE

RESULTS AND DISCUSSIONS

5.1 CALCULATION OF THE HEAT TRANSFER COEFFICIENT

The method used to calculate the heat transfer coefficient, h, was based on the analysis of objects of uniform cross sectional area with uniform heat generation [19]. Figure 5.1 illustrates the flat strip fin model used for the derivation of h.

Since $w_s >> t_s$, the classic fin equation derivation was used with a modification to account for heat generation. The following assumptions were made:

- 1-D conduction in the x-direction
- Steady state conditions
- Thermal conductivity is constant
- Radiation effects are negligible
- h is uniform over the surface

The following results were obtained by applying the conservation of energy to an element of width dx, as shown in Figure 5.2

$$q_x + q'dx = q_{x+dx} + dq_{conv} \tag{5.1}$$

where,

The heat conduction into the control volume (CV) is:

$$q_x = -kA_c \frac{dT}{dx} \tag{5.2}$$

The heat generated within the CV by electrical resistance is:

$$q'dx = \frac{VI}{L}dx \tag{5.3}$$

The heat conduction out of CV is:

$$q_{x+dx} = q_x + \frac{dq_x}{dx}dx \tag{5.4}$$

The heat convection from CV surface is:

$$dq_{conv} = hdA_s\left[T(x) - T_\infty\right] \tag{5.5}$$

and the surface area of element

$$dA_s = Pdx \tag{5.6}$$

Substituting Equations (5.2) to (5.5) into Equation (5.1) and re-arranging yields:

$$\frac{VI}{LkA_c} = -\frac{d^2T(x)}{dx^2} + \frac{hP}{kA_c}\left[T(x) - T_\infty\right] \tag{5.7}$$

Defining an excess temperature $\theta(x)$ as:

$$\theta(x) \equiv T(x) - T_\infty \tag{5.8}$$

Since T_∞ is constant:

$$\frac{d^2\theta(x)}{dx^2} = \frac{d^2T(x)}{dx^2} \tag{5.9}$$

Transforming the dependent variable in Equation (5.7) with Equations (5.8) and (5.9) forms the following linear, second order differential equation:

$$\frac{VI}{LkA_c} = -\frac{d^2\theta(x)}{dx^2} + m^2\theta(x) \tag{5.10}$$

where,

$$m^2 \equiv \frac{hP}{kA_c}$$

The general solution to Equation (5.10) is given by:

$$\theta(x) = C_1 e^{mx} + C_2 e^{-mx} + \frac{VI}{LhP} \tag{5.11}$$

The constants of integration C_1 and C_2, were resolved by defining the axis origin at the center of the sample, illustrated in Figure 5.1. The first boundary condition was established by analyzing the excess temperature change at x = 0, which is constant by symmetry;

$$\frac{d\theta(0)}{dx} = 0 \tag{5.12}$$

Applying the first boundary condition to Equation (5.10) results in $C_1 = C_2 = C$. Applying the identity $2\cosh(mx) = e^{mx} + e^{-mx}$ and the constant C to Equation (5.10) gives:

$$\theta(x) = C\left[2\cosh(mx)\right] + \frac{VI}{LhP} \tag{5.13}$$

The second boundary condition was developed by defining an excess terminal temperature at $x = \pm\frac{L}{2}$:

$$\theta_T = \theta\left(\pm\tfrac{L}{2}\right) \equiv T_T - T_\infty \tag{5.14}$$

where the terminal temperatures $T_T = T\left(\pm\frac{L}{2}\right)$ were measured and therefore known quantities. Solving Equation (5.13) for C using the second boundary condition gives:

$$C = \frac{\theta_T - \dfrac{VI}{LhP}}{2\cosh\left(m\dfrac{L}{2}\right)} \tag{5.15}$$

Substituting (5.15) and the excess temperature definition (5.8) into Equation (5.13), the final form where h appears in the temperature profile is given by:

$$T(x) = \left[\theta_T - \frac{VI}{LhP}\right]\frac{\cosh(mx)}{\cosh\left(m\frac{L}{2}\right)} + \frac{VI}{LhP} + T_\infty \qquad (5.16)$$

where,

T(x) = Temperature at position "x" along the samples length

θ_T = Excess terminal temperature

V = Measured voltage drop across the samples end terminals

I = Current supplied to sample

L = Heated sample length

h = Heat transfer coefficient

k = Sample thermal conductivity (constant)

T_∞ = Bed temperature

$$m = \sqrt{\frac{hP}{kA_c}}$$

The geometry for the cylinders and strips used in this work are defined in the following table.

Table 5.1 – Sample Geometry

	Cylinder Sample	Flat Strip Sample
P, Perimeter	$P_{cylinder} = \pi d_s$	$P_{strip} = 2w_s + 2t_s$
A_c, Cross-sectional area	$A_{c,cylinder} = \frac{\pi\left(d_s^2 - d_i^2\right)}{4}$	$A_{c,strip} = w_s t_s$
dA_s, Surface Area of Element	$dA_{s,cylinder} = \pi d_s dx$	$dA_{s,strip} = (2w_s + 2t_s)dx$
Geometry definitions	d_s = Outside diameter d_i = Inner diameter	w_s = Sample width t_s = Sample thickness $w_s >> t_s$

Equation (5.16) was used for both cylinder tube and flat strip h calculations with respective geometry modifications. It must be noted that the tube ends were sealed with silicon allowing no air to flow inside the cylinder tube. This allowed the air's temperature to gradually increase to a steady state temperature equivalent to the temperature of the inside cylinder tube wall. Once steady state is reached, there will no longer be heat generated by the cylinder tube wall conducted into the air.

As mentioned in Chapter 3, large copper terminal connectors were required to manage the large currents used to heat the samples. As a result, assuming uniform temperature along the length of the sample was not necessarily a good assumption, particularly for the larger samples where L/d_s and L/w_s were small. In order to account for this, the above model was developed to use both the centerline temperature T_s and T_T, the measured terminal temperature. Figure 5.3 illustrates the worst case temperature distribution for a $d_s = 0.00127$m sample plotted along the samples length, $L = 0.256$m. The conditions used to calculate the temperature distribution are summarized in Table 5.2. It is observed that the temperature distribution is essentially constant along 86% of its length and approaches the terminal temperature over the remaining 7% where conduction losses into the terminals are significant [20].

Examining Equation (5.16), the heat transfer coefficient appears implicitly; therefore, an iterative method was used by varying h until T(0) matched the measured T_s using mathematical software. The simple expression $h = \frac{VI}{A_s(T_s - T_\infty)}$ was in error by nearly 10%, justifying use of this model.

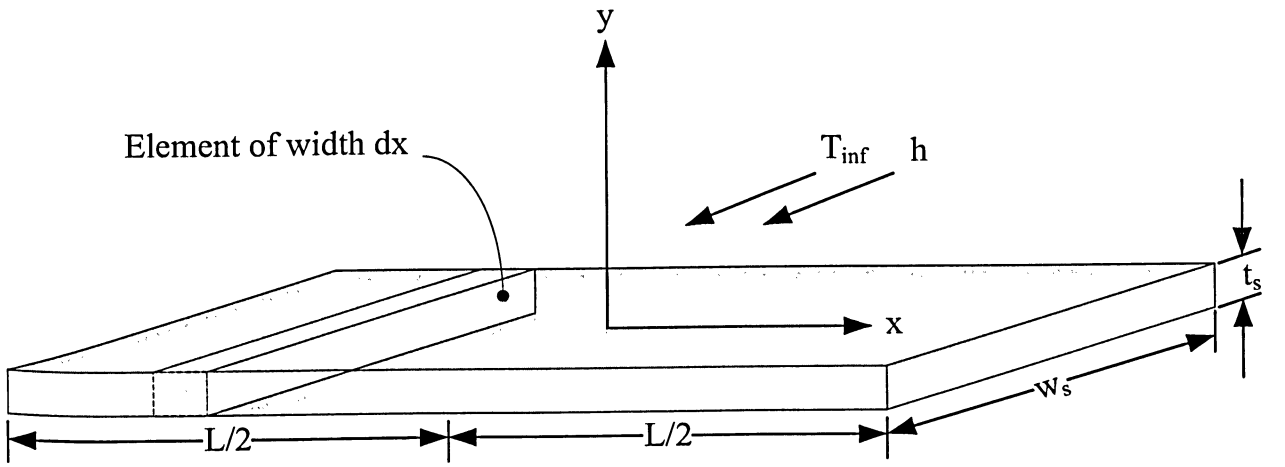

Figure 5.1 – Flat Strip Fin Model

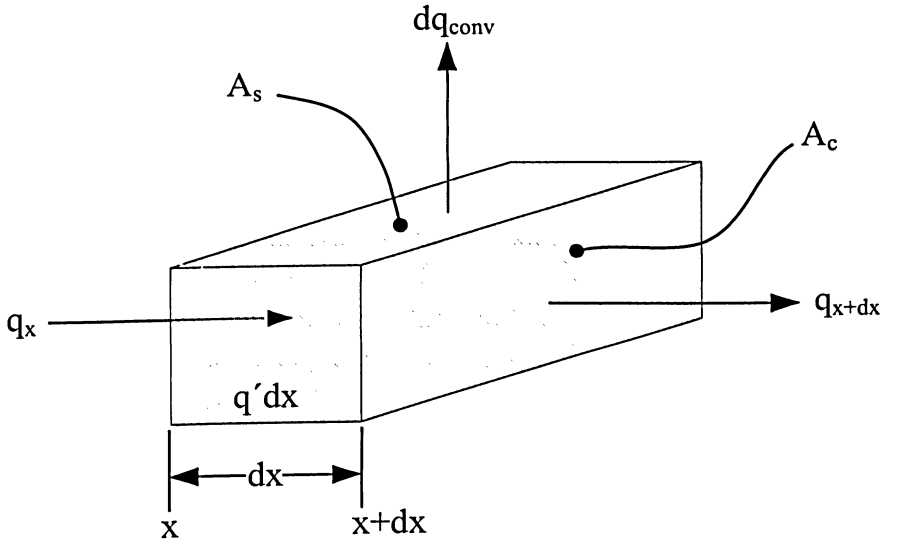

Figure 5.2 – Energy Balance of Element of Width dx

Table 5.2 – Conditions Used to Calculate the Temperature Distribution for Figure 5.3

Heat Generation	V = 0.7546V	I = 2.49A
Heat Transfer Properties	h = 159.7W/m^2-K	k = 14.9W/m-K
Geometry	L = 0.256m	d_s = 0.00127m
Temperatures	T_s = 30.5°C T_∞ = 19°C	T_T = 19.3°C

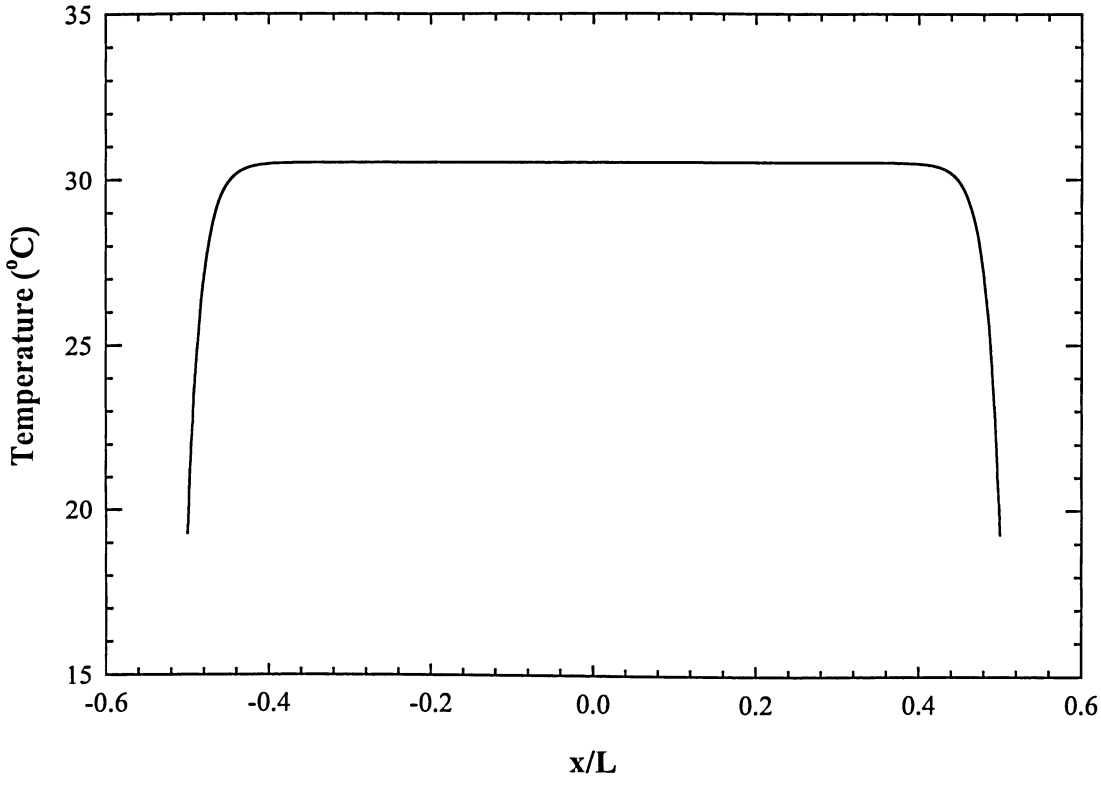

Figure 5.3 – Sample Temperature Distribution based on Equation (5.16) for d_s = 1.27mm

5.2 HEAT TRANSFER TO SMALL CYLINDERS IMMERSED IN A FLUIDIZED BED

Tests were carried out by immersing the sample cylinders in beds of aluminum oxide sand detailed in Table 5.3.

Table 5.3 – Properties of Aluminum Oxide Sand

Grit Sand Size	50	60	70	80	90
Mean Particle Diameter, d_p (μm)	330	254	203	165	145
Density, ρ_p (kg/m^3)	3970	3970	3970	3970	3970
Fluidizing Rate Range, G/G_{mf}	0.14–5	0.22–8.5	0.34–14	0.5–15	0.64–22
Archimedes Number, Ar	5175	2360	1205	657	439
Fluidizing Gas Mass flux at minimum fluidizing conditions, G_{mf} (kg/m^2-s)	0.156	0.099	0.066	0.045	0.035

Heat transfer rates were calculated using Equation (5.16) by measuring the steady state temperature difference between the cylinder surface and the bed for fluidizing rates $0.14 < G/G_{mf} < 22$. An experimental Nusselt number, Nu_{exp}, was calculated using the thermal conductivity of air, k_{air}, based on the average film temperature, T_{film}.

$$Nu_{exp} = \frac{hd_s}{k_{air}} \tag{5.17}$$

where,

$$T_{film} = \frac{\Delta T_{avg} + \Delta T_{tube}}{2} + T_\infty$$

$$\Delta T_{avg} \equiv T_s - T_\infty$$

$\Delta T_{tube} \equiv$ Temperature difference between inside of tube and outside due to tube wall resistance. (5.18)

$\Delta T_{tube} = 0$ for flat strip

Nu_{exp} versus G/G_{mf} are plotted in Figure 5.4 to 5.6 for all samples in 50, 70 and 90 grit sand. It can be seen from these figures that Nu_{exp} was at a minimum for low ranges of G/G_{mf} and begins to increase at approximately 1.5 G/G_{mf}. Nu_{exp} continues to increase rapidly up to 2.5

G/G_{mf}, where a maximum exists and remains constant within a ±5 - 10% range for higher fluidizing rates up to 22 G/G_{mf}. As mentioned, in a bubbling fluidized bed, the heat transfer coefficient depends on two major parameters: particle residence time near the tube surface (particle convection) and bed porosity adjacent to the tube surface (gas convection). When the gas velocity is increased, particle residence time, τ, is decreased due to the rising bubbles and higher bed porosity. At low velocities (below 2.5 × G_{mf}), these competing effects result in an increase in heat transfer coefficient when the fluidizing velocity is increased [9]. Figure 5.7 shows the results for heat transfer measurements from a 7.94mm diameter sample for all grit size tested. It can be seen that particle size d_p did not influence h in the laminar flow regime, a result well established in published literature [21]; therefore, heat transfer rates at lower ranges of G/G_{mf} were not studied in this thesis, but it should be emphasized that this type of qualitative variation of Nu_{exp} with G is characteristic of fluid-particle systems belonging to Geldart's group B powder classification [13]. This trend was similar for all sample cylinders tested for all grit sizes.

A steady Nusselt number value, Nu_{mean}, was evaluated by calculating the mean of Nu_{exp} values in the fully fluidized regime, i.e., from $G = 2.5 \times G_{mf}$ to the maximum flow rate tested for that sample (Nu_{mean} was adjusted accordingly for results indicating a plateau higher than $G/G_{mf} = 2.5$). Nu_{mean} is plotted versus the mean particle diameter, d_p, in Figure 5.8 for all cylinder data. It can be seen that Nu_{mean} decreases as d_p increases. It is also observed that Nu_{mean} increases as the cylinder diameter, d_s, increases. This qualitative trend is in complete agreement with published results in the literature [7, 9] for tubes immersed in fluidized bed. This is because for larger particles, the effective thickness of the gas film increases while the surface to volume ratio decreases. As mentioned, the residence time, τ, of the particles at the heat transfer surface

depends on the fluidizing velocity and increasing it causes τ to decrease [1]; in other words, the net surface area of particle contact with the tube for smaller solid particle diameter increases. Furthermore, due to changes in the particle motion/hydrodynamics, the particle convection would increase for smaller particles [9]. The effect of cylinder diameter in Nusselt number is further discussed in Section 6.2.2.

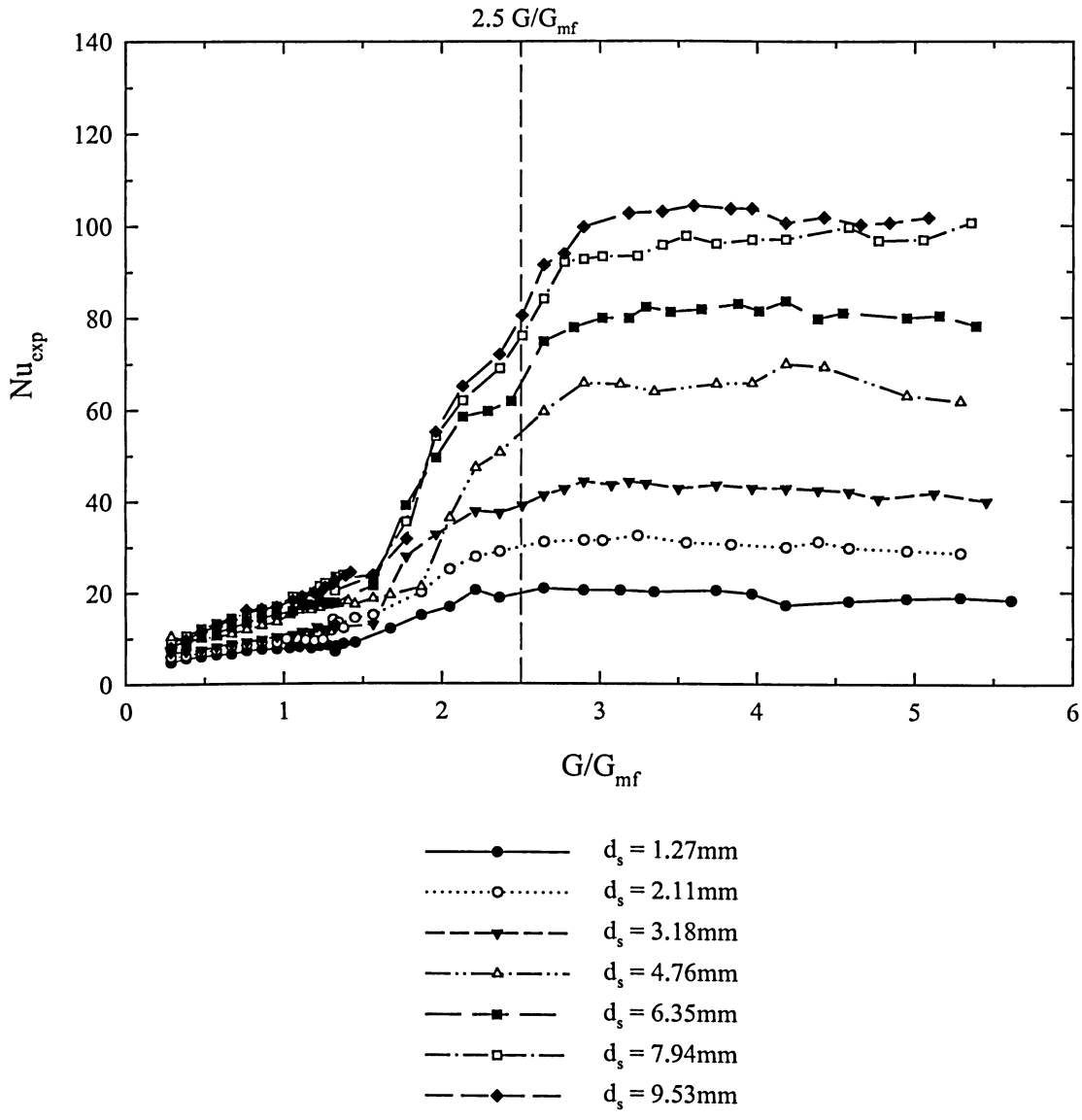

Figure 5.4 - Experimental Nusselt Number vs. G/G_{mf} in 50 Grit Sand for all Cylinder Sizes

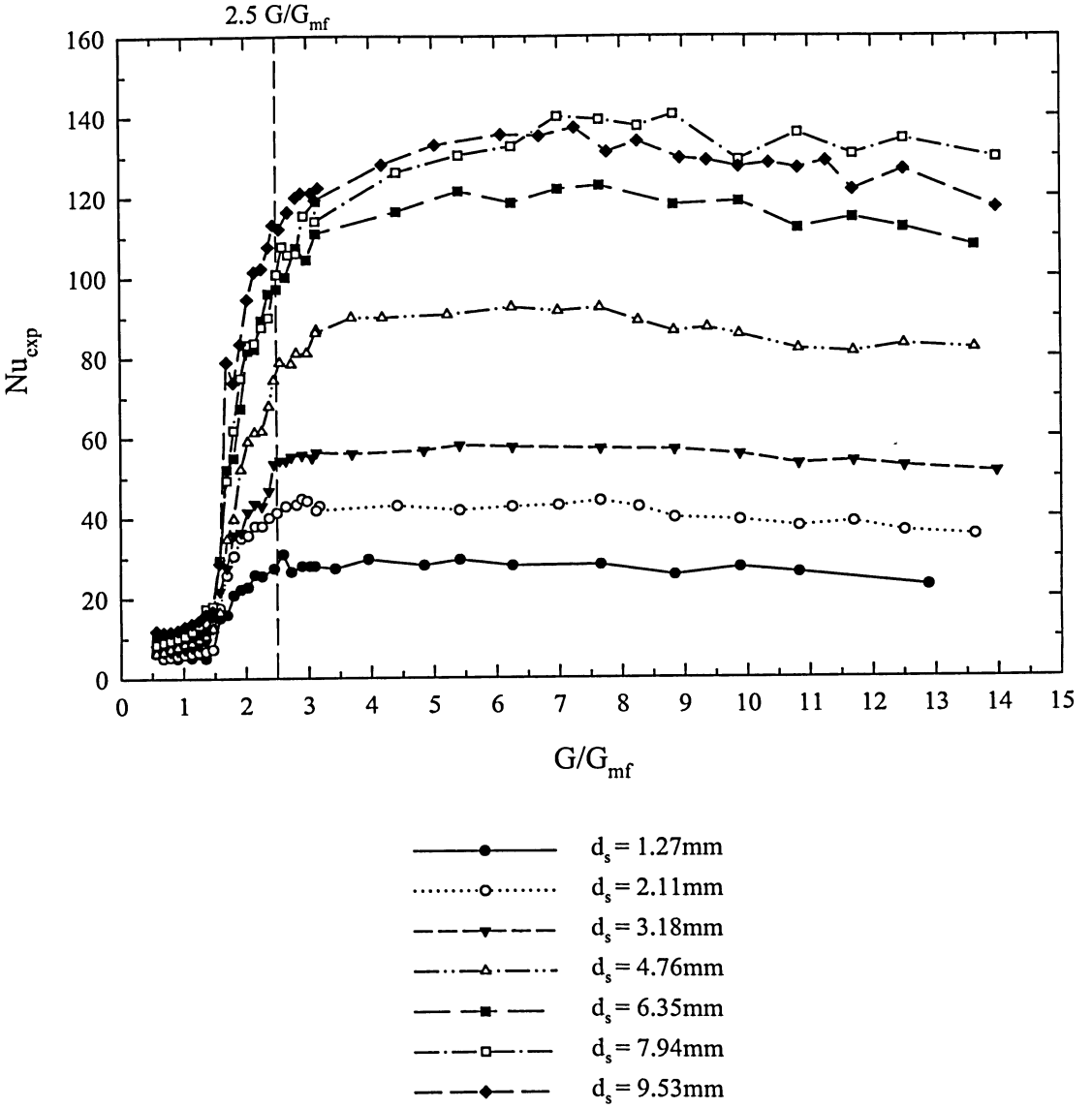

Figure 5.5 – Experimental Nusselt Number vs. G/G_{mf} in 70 Grit Sand for all Cylinder Sizes

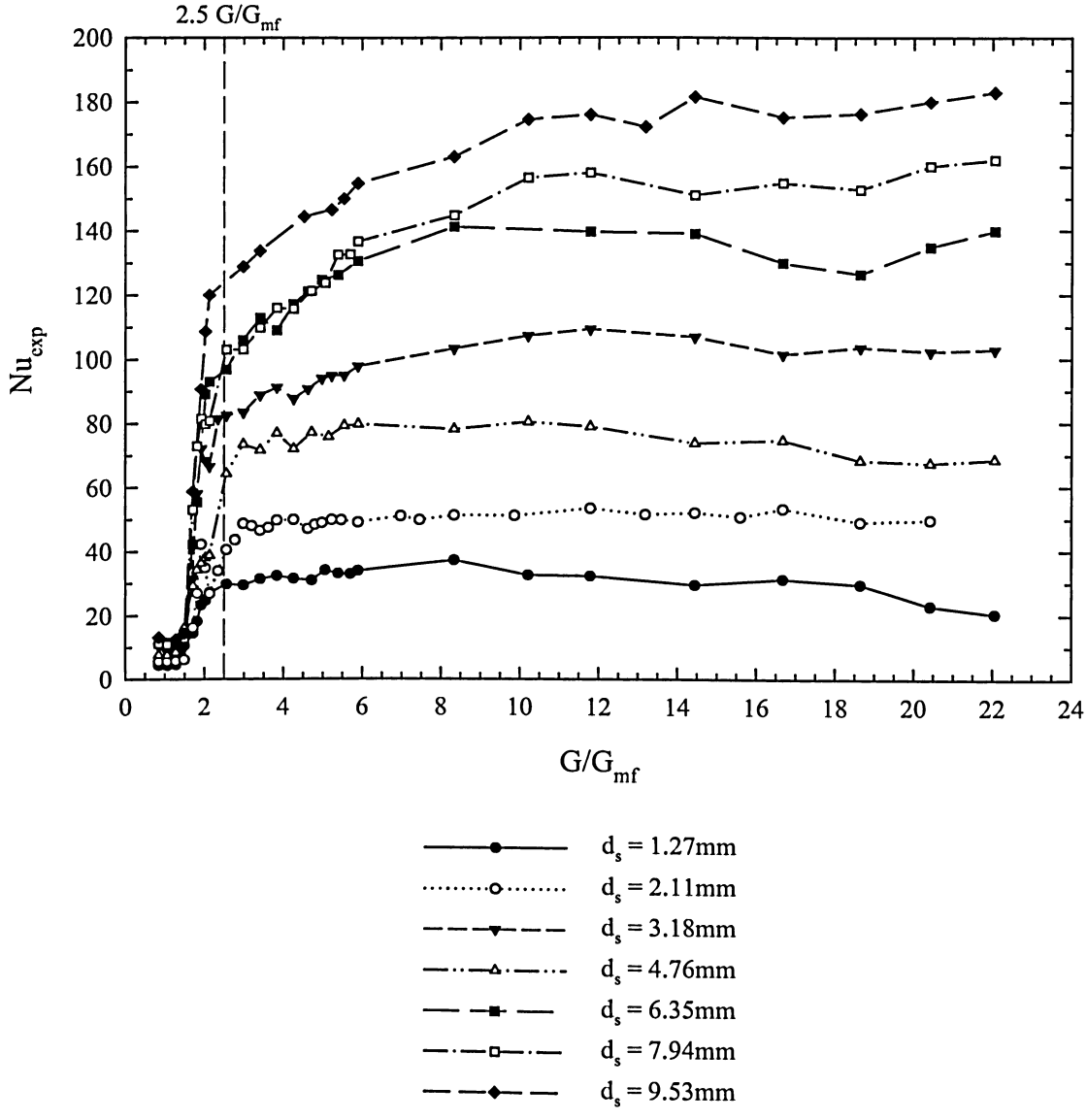

Figure 5.6 - Experimental Nusselt Number vs. G/G_{mf} in 90 Grit Sand for all Cylinder Sizes

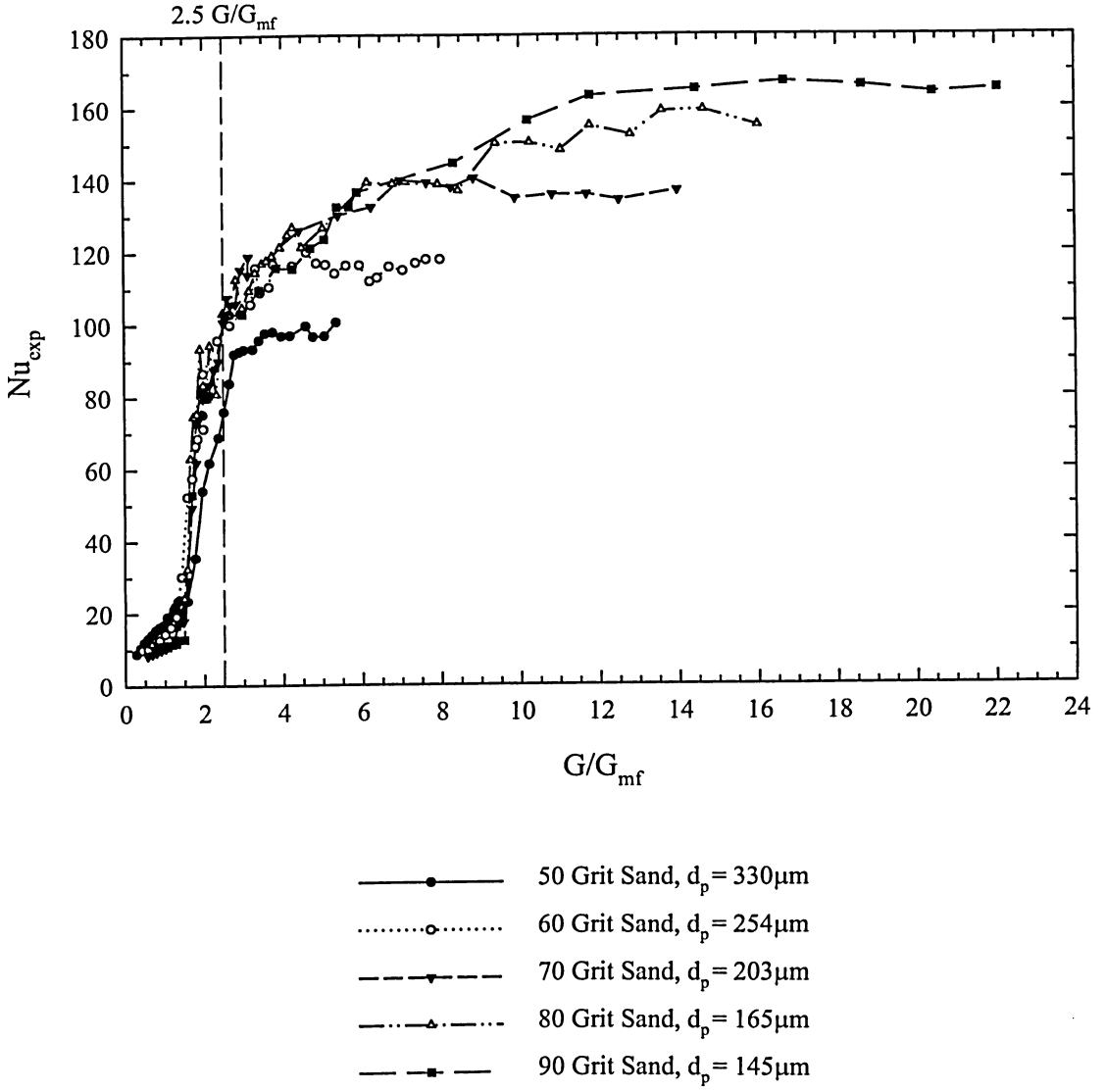

Figure 5.7 – Experimental Nusselt Number vs. G/G_{mf} for a 7.94mm Cylinder Sample for all Grit Sizes

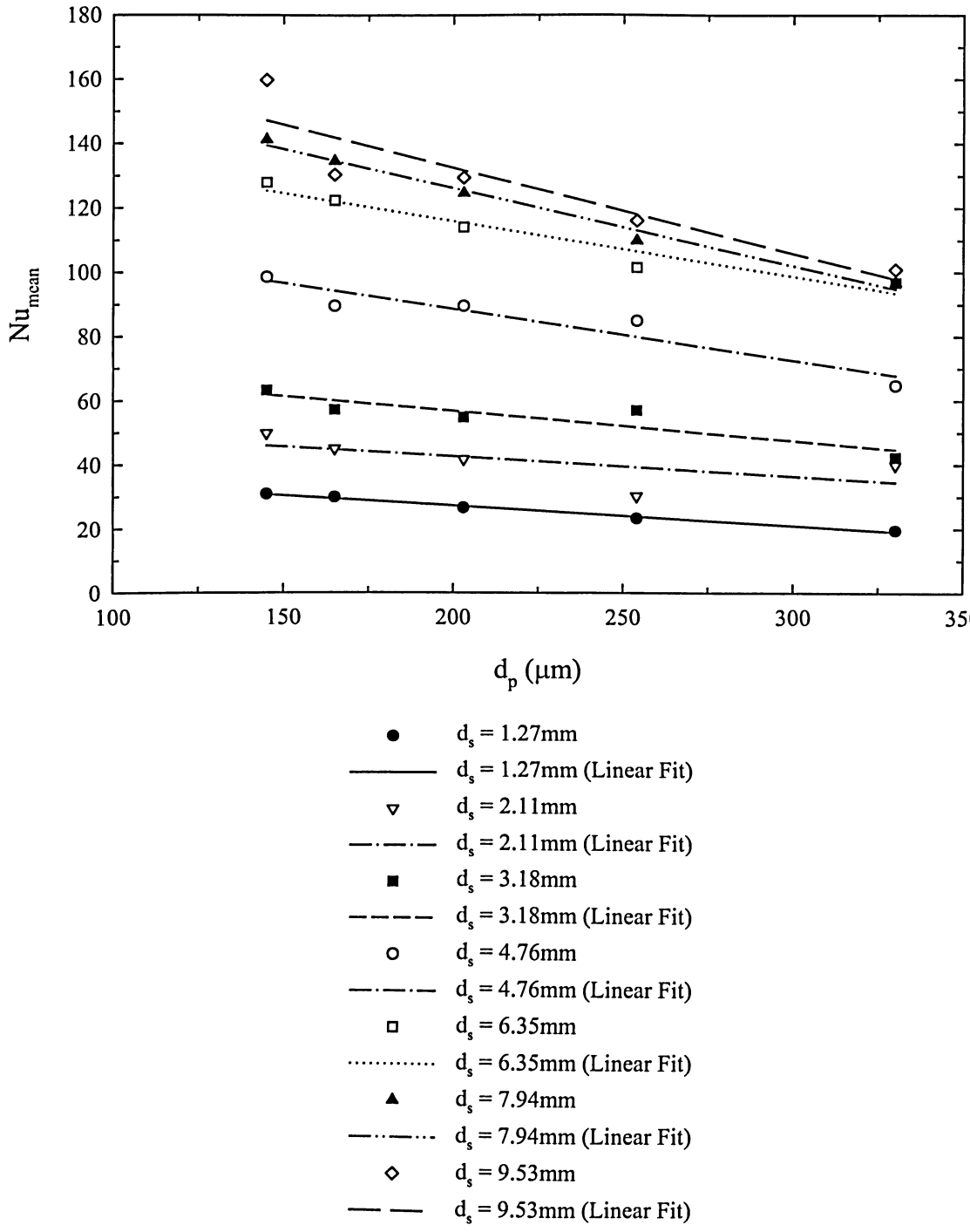

Figure 5.8 – Mean Nusselt Number vs. Mean Particle Diameter for all Cylinder Sizes

5.3 HEAT TRANSFER TO FLAT STRIPS IMMERSED IN A FLUIDIZED BED

Tests were carried out by immersing the sample strips in beds of aluminum oxide sand, detailed in Table 5.3, from a horizontal (0°) to a vertical (90°) orientation in 15° increments. The heat transfer coefficient was calculated using Equation (5.16) with its respective geometry, shown in Table 5.1. Nu_{exp} versus G/G_{mf} trends for w_s = 6.35, 9.53 and 12.70mm samples were similar to those observed from small cylinders, as seen in Figure 5.9 to 5.11. However, the largest sample tested, w_s = 25.40mm (1"), at a 0° orientation demonstrated behaviour similar to those reported by [4] for large tubes in fluidized bed, where the heat transfer rate continues to increase monotonically with fluidizing rate increase.

Figure 5.12 presents the results obtained by rotating the 12.70mm samples orientation from 0° to 90° in 30° increments in a 70 Grit bed. It is shown that the sample's orientation has a significant influence on Nu_{exp} increasing by approximately 15% from a flat horizontal orientation (0°) to a vertical position (90°). To illustrate this better, Nu_{mcan} was calculated using the method described in Section 5.2 and plotted in Figure 5.13 versus the angle orientation for w_s = 12.70mm in 50, 70 and 90 grit beds. It clearly illustrates the influence angle orientation has on the heat transfer coefficient, where the relationship is linear and increases steadily as the angle increases. It is understood that $\frac{\partial Nu}{\partial \theta}$ would be zero at both 0° and 90° due to symmetry, but this trend is not shown in Figure 5.13 for simplification purposes. These results were consistent for all samples and grit size tested. The effect of orientation on the heat transfer coefficient is discussed further in Section 6.3.2.

The particle size has the same influence on the heat transfer coefficient as discussed earlier for small cylinders where h decreases as d_p increases, illustrated in Figure 5.14 to 5.16 for

all w_s at 0°, 45° and 90° orientations respectively. Taking a closer look at the figures, the 25.4mm sample shows an exception to this trend at 0° and 45° orientations where an increase in Nu_{mean} is observed from d_p = 145 to 203μm. Inspecting the 25.4mm sample data further, it is observed in Figure 5.17 that the increase in Nu_{mean} in the $145 < d_p < 203\mu m$ range is consistent for all orientations except for 75° and 90°. This implies that 70 Grit sand has the best particle motion around a large strip in a horizontal position, a key element in good heat transfer to an immersed surface discussed further in Chapter 6.

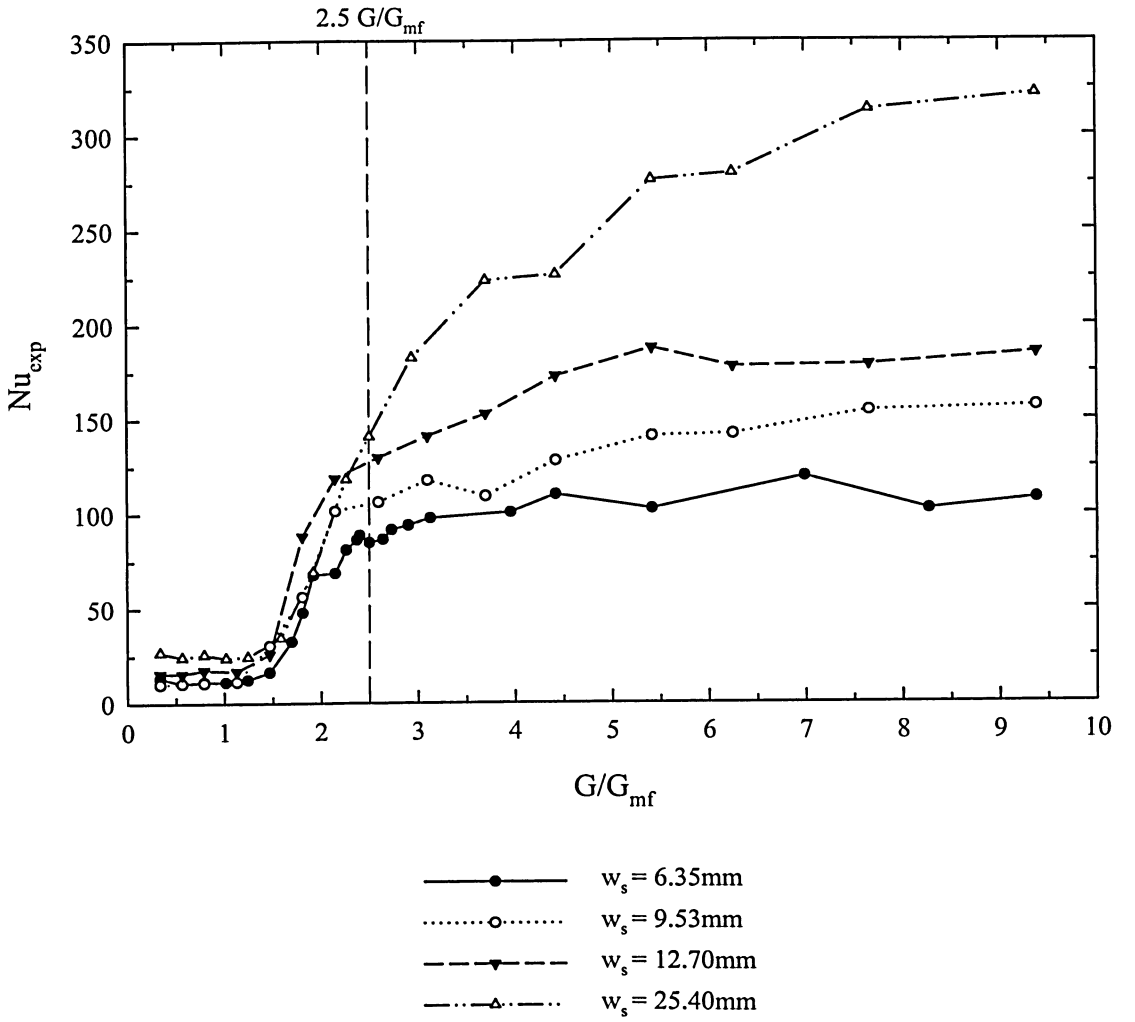

Figure 5.9 – Experimental Nusselt Number vs. G/G_{mf} for all Flat Strip Sample Sizes at 0° Orientation in 70 Grit Sand

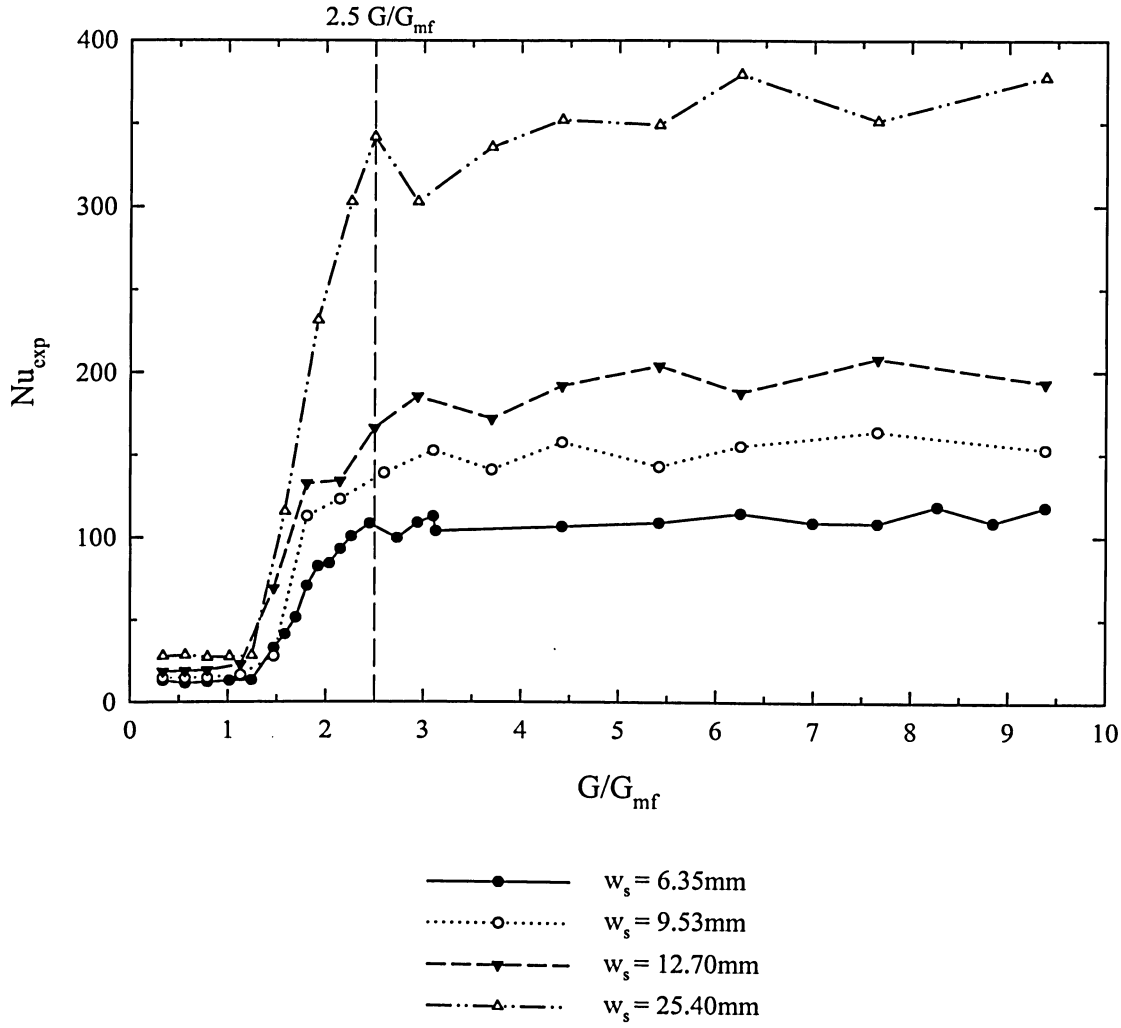

Figure 5.10 - Experimental Nusselt Number vs. G/G_{mf} for all Flat Strip Sample Sizes at 45° Orientation in 70 Grit Sand

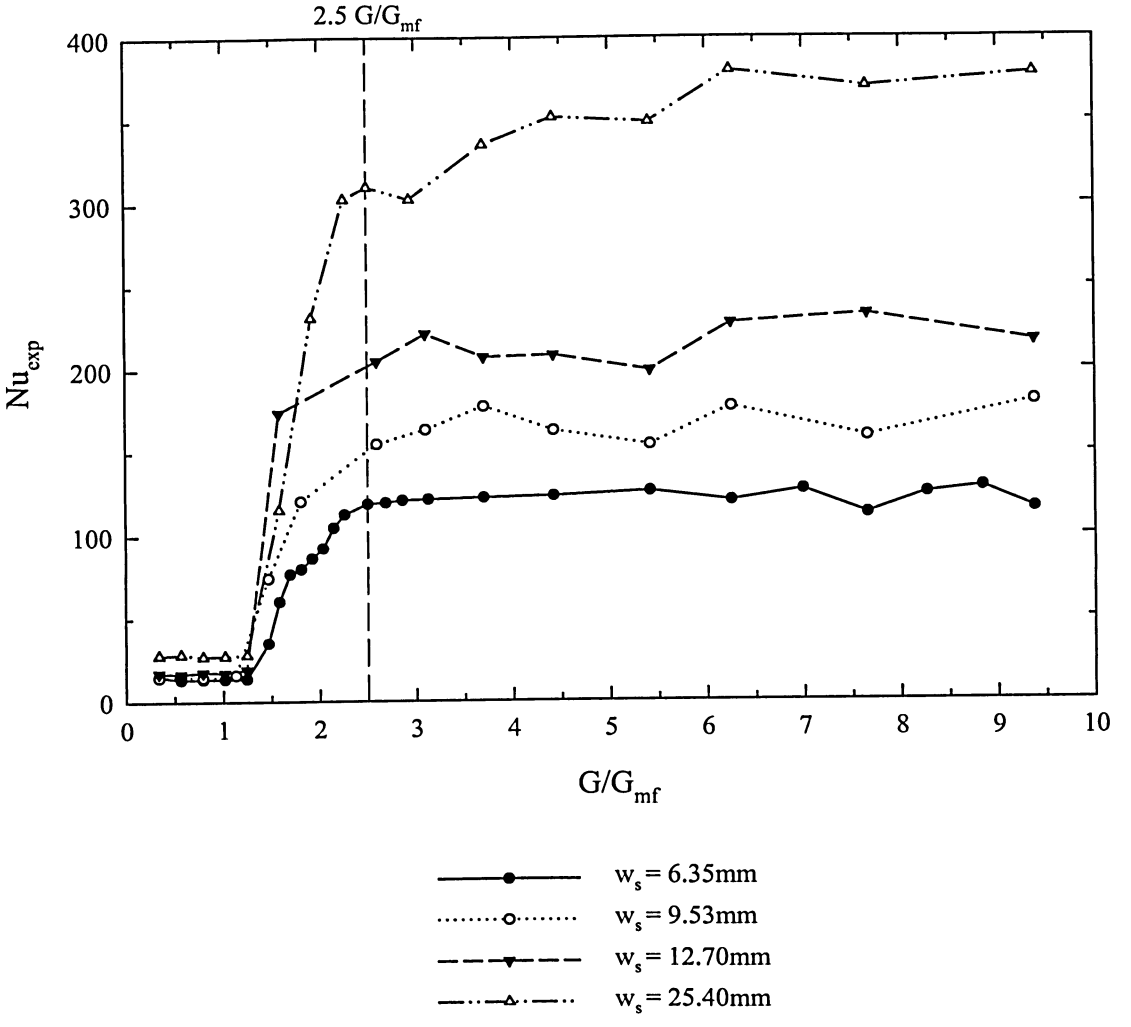

Figure 5.11 - Experimental Nusselt Number vs. G/G_{mf} for all Flat Strip Sample Sizes at 90° Orientation in 70 Grit Sand

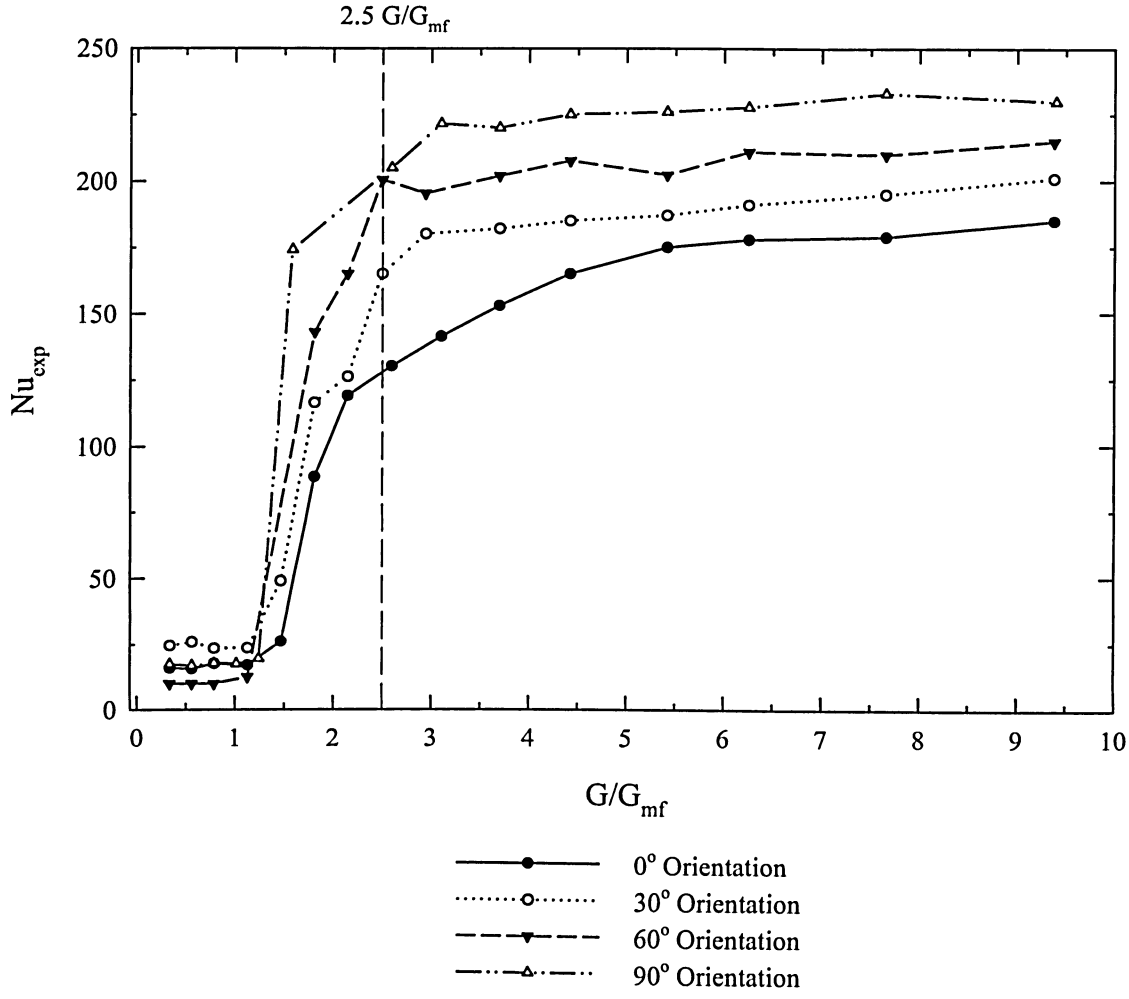

Figure 5.12 – Experimental Nusselt Number vs. G/G_{mf} for w_s = 12.70mm Flat Strip Sample in 70 Grit Sand for 0°, 30°, 60° and 90° Orientations

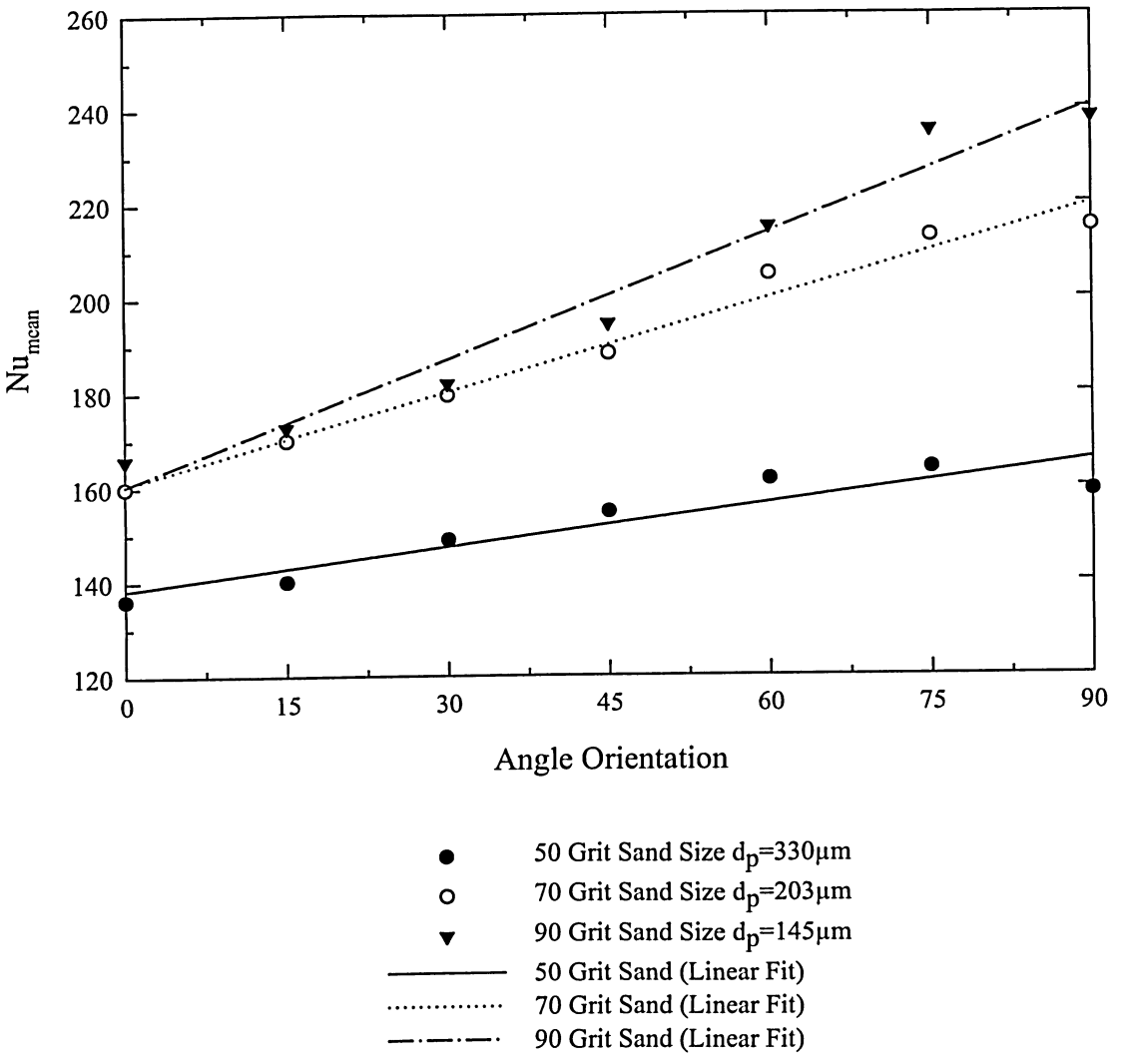

Figure 5.13 – Mean Nusselt Number vs. Angle Orientation for w_s = 12.70mm Flat Strip Sample in 50, 70 and 90 Grit Sand

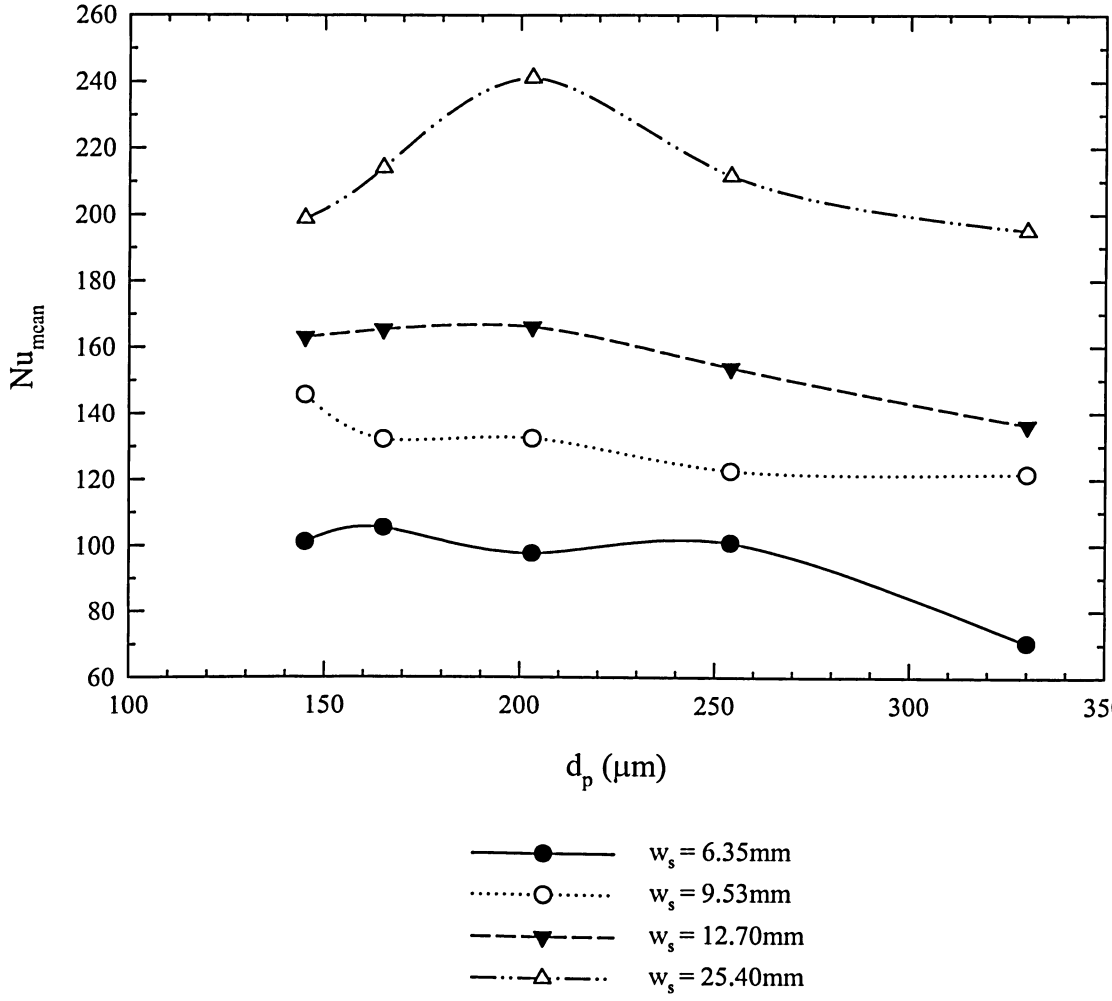

Figure 5.14 – Mean Nusselt Number vs. Particle Size for all Flat Strip Samples at 0°

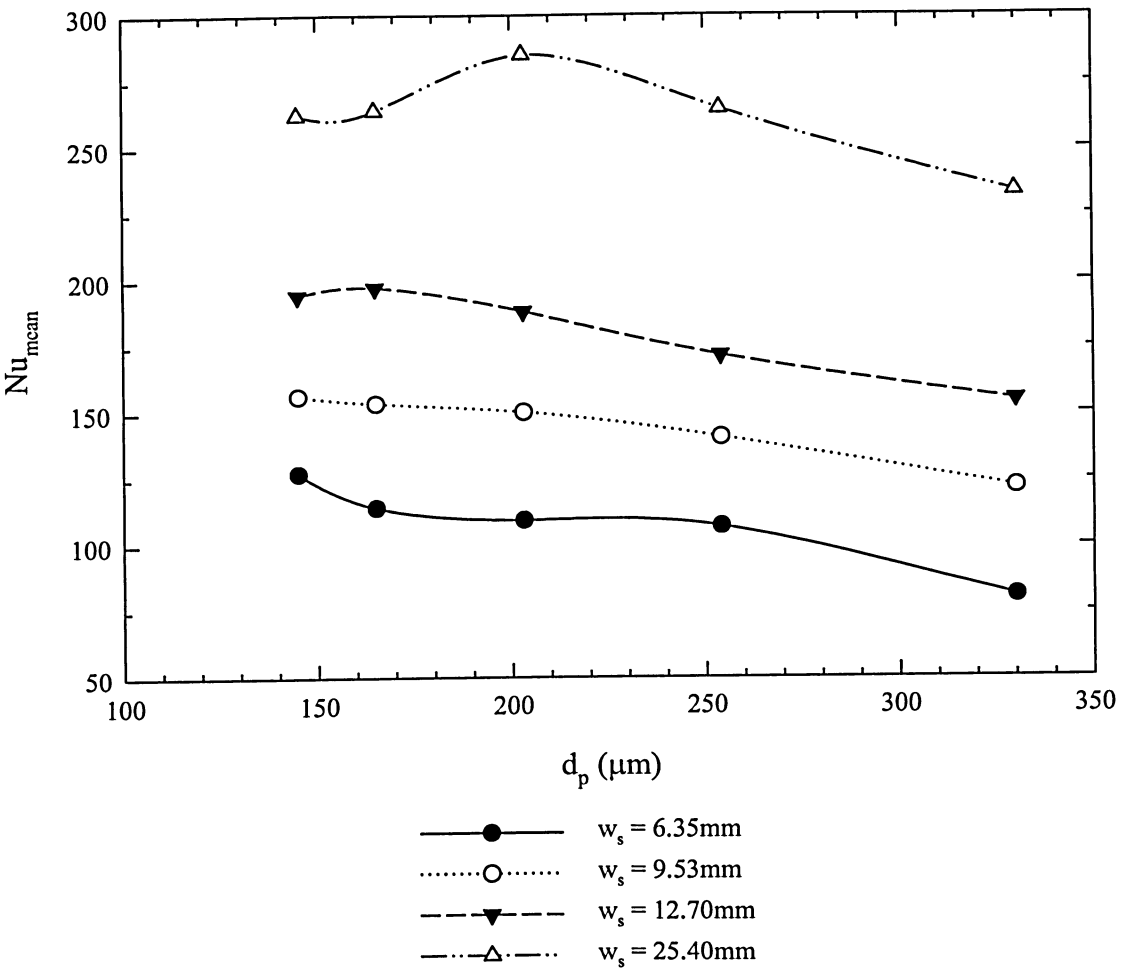

Figure 5.15 - Mean Nusselt Number vs. Particle Size for all Flat Strip Samples at 45°

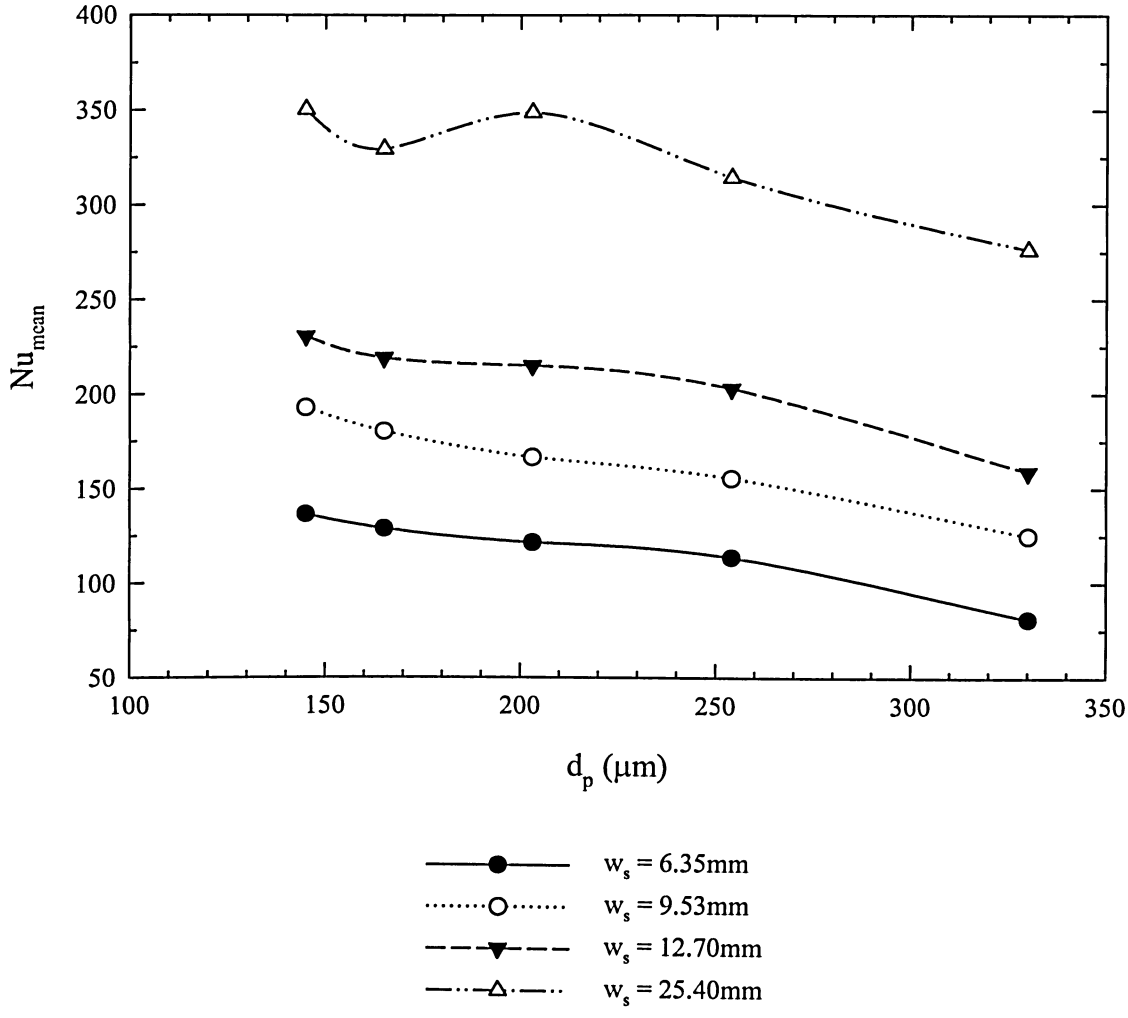

Figure 5.16 - Mean Nusselt Number vs. Particle Size for all Flat Strip Samples at 90°

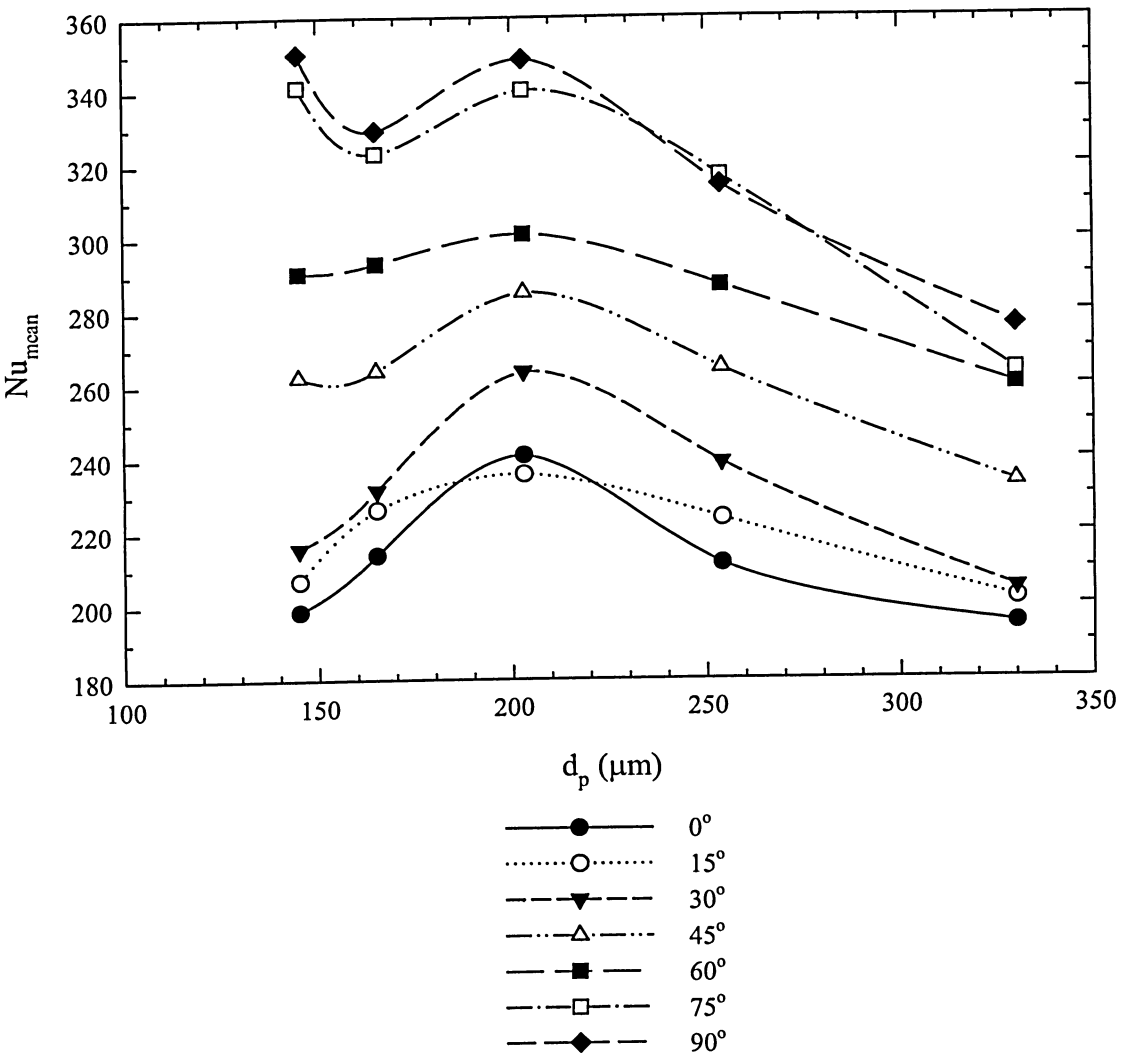

Figure 5.17 – Mean Nusselt Number vs. Particle Size for w_s = 25.4mm Sample for all Orientation

CHAPTER SIX

ANALYSIS

6.1 DIMENSIONAL ANALYSIS

It is beneficial to perform a dimensional analysis for a given configuration (fluidized bed and heat transfer surface) to establish which variables affect the heat transfer coefficient, h. It is understood that h is a function of the physical properties of the particulate material and the fluidizing agent, as well as flow rate [22]. The following table presents the influencing factors with their respective units and dimension.

Table 6.1 – Summary of Properties

Properties	Units	Dimension
Acceleration due to gravity, g	m/s^2	L/t^2
Particle Diameter, d_p	m	L
Particle Density, ρ_p	kg/m^3	M/L^3
Particle Specific Heat, C_{ps}	Ws/kg-K	L^2/t^2-T
Particle Thermal Conductivity, k_p	W/m-K	ML/t^3-T
Gas Viscosity, μ_g	kg/m-s	M/L-t
Gas Density, ρ_g	kg/m^3	M/L^3
Gas Specific Heat, C_{pg}	Ws/kg-K	L^2/t^2-T
Gas Thermal Conductivity, k_g	W/m-K	ML/t^3-T
Characteristic Length, L_c	m	L
Fluidizing Gas Mass Flux, G	kg/m^2-s	M/L^2-t
Bed Voidage, ε	-	-
Heat Transfer Coefficient	W/m^2-K	$M/T\text{-}t^3$

The Buckingham Π Theorem can be applied to form dimensional groups with the influencing factors of Table 6.1. Four dimensions are considered in the analysis, specifically: mass M, length L, time t, and temperature T. With thirteen dimensional variables and four dimensions, nine dimensionless groups can be obtained, which are presented below:

$$\Pi_1 = \frac{\rho_g d_p^3 (\rho_p - \rho_g) g}{\mu_g^2} \equiv Ar \tag{6.1}$$

$$\Pi_2 = \frac{\rho_p}{\rho_g} \tag{6.2}$$

$$\Pi_3 = \frac{C_{pg}\mu_g}{k_g} \equiv Pr \tag{6.3}$$

$$\Pi_4 = \frac{C_{ps}\mu_g}{k_g} \tag{6.4}$$

$$\Pi_5 = \frac{k_p}{k_g} \tag{6.5}$$

$$\Pi_6 = \frac{L_c}{d_p} \tag{6.6}$$

$$\Pi_7 = \frac{G}{G_{mf}} \tag{6.7}$$

$$\Pi_8 = 1 - \varepsilon \tag{6.8}$$

The non-dimensional heat transfer coefficient is defined as usual in the form of a Nusselt Number:

$$\Pi_9 = \frac{hL_c}{k_g} \equiv Nu \tag{6.9}$$

where the characteristic length is defined as:

$$L_c = d_s \text{ (outside diameter of the cylinder sample)} \tag{6.10}$$

$$L_c = w_s \text{ (width of the flat strip sample)} \tag{6.11}$$

The non-dimensional groups affecting the Nusselt number are determined by examining the properties of the solids and the fluidizing agent in the laminar flow regime. According to Molerus *et al.* [22], the gas density ρ_g has an insignificant effect on the heat transfer coefficient in the laminar flow regime. This was determined experimentally by measuring heat transfer coefficients in a fluidized bed operating at 0.1 and 10MPa, indicating no significant difference of h values between the two pressures [22]. Therefore, the non-dimensional group Π_2 is excluded from further analysis.

As discussed in Section 2.5.2, one of the controlling factors for heat transfer between the bed and surface is the gas thermal conductivity, k_g. This property is relevant because the heat transfer occurs mainly through the gas film between the particles and the surface for fluidizing rates near G_{mf} and must be accounted for in predicting a suitable Nusselt number. On the contrary, the particle thermal conductivity, k_p, can be neglected. Many investigators [4, 23] reported that k_p had no effect on heat transfer. Experimental results reported in Chapter 5 indicate that heat transfer by conduction and its magnitude is small at low G/G_{mf}, where there is little particle motion and long contact times between the particles and sample's surface. For conditions in excess of G_{mf}, the overall heat transfer mechanism changes from pure conduction to particle and gas convection. At these conditions, the volumetric heat capacity of the particles and the gas thermal conductivity control the overall heat transfer process [4]. Thus, k_p is considered negligible for conditions in excess of G_{mf}, excluding Π_5 from further analysis.

According to moving-bed experiments reported in [22], the gas specific heat C_{pg} can be assumed insignificant for heat transfer from the heating surface to fine-grained particles. In addition, the volumetric heat capacity of the gas, $\rho_g C_{pg}$, is insignificant when compared in magnitude with $\rho_p C_{ps}$. The non-dimensional group Π_3 is left out from further analysis.

Based on the results reported in Chapter 5, the Nusselt number does not vary much beyond $G/G_{mf} > 2.5$ (where the mean Nusselt number was evaluated from). This suggests that G does not have a significant influence on the heat transfer coefficient in the higher fluidizing rates tested; therefore, the non-dimensional parameter Π_7 can be eliminated from further analysis, provided that $G/G_{mf} > 2.5$. Furthermore, since ε depends on G, Π_8 can also be eliminated from the analysis.

Given that all experimental runs conducted operated with the same fluidizing gas and particles at ambient bed temperatures, the non-dimensional parameter Π_4 remained constant for all runs, and therefore cannot be included in the analysis.

Therefore, based on dimensional analysis and experimental trends observed at higher fluidizing rates the Nusselt number is mainly a function of the following:

$$Nu = f\left(Ar; \frac{L_c}{d_p}\right) \tag{6.12}$$

The characteristic length is replaced using Equation (6.10) for small cylinders,

$$Nu = f\left(Ar; \frac{d_s}{d_p}\right) \tag{6.13}$$

and Equation (6.11) for flat strips with an additional factor, θ_o, corresponding to the angle orientation of the sample in degrees.

$$Nu = f\left(Ar; \frac{w_s}{d_p}; \theta_o\right) \tag{6.14}$$

6.2 SMALL CYLINDERS IMMERSED IN A FLUIDIZED BED

Many correlations have been developed by other investigators for predicting Nusselt number for immersed horizontal tubes in fluidized beds of small particles [5 – 8, 17]. They have been presented in Chapter 2. These correlations are well summarized by Saxena [1] and are used to predict the Nusselt number for three cases, illustrated in Figures 6.1 to 6.3 along with experimental data. As can be seen in the figures, all the correlations grossly over-predict the heat transfer rate from the sample, and none show the steady plateau apparent in the data [20].

As discussed in Section 5.2 and illustrated in Figures 5.4 to 5.7 all of the cylinder data taken demonstrated this steady plateau trend, except for the larger samples in 90 grit bed where the plateau developed at higher fluidizing rates. These correlations were developed using tube diameters larger than the tubes presently studied and do not extrapolate down to the smaller tube diameters tested. It is worth noting Grewal and Saxena's correlation unsuccessfully predicts Nu within the uncertainty of 25% as claimed by the authors [7]. The effect of cylinder diameter is further discussed in Section 6.2.2.

6.2.1 CORRELATING EXPERIMENTAL DATA

Nu_{mean} was plotted versus the non-dimensional group d_s/d_p for d_p = 145, 203 and 330μm (90, 70 and 50 Grit Sizes) shown in Figure 6.4. It is observed from the figure that the relationship is approximately linear for each particle size tested. An effort was made to collapse all the data to a single curve. The dimensional analysis discussed in Section 6.1 suggests that the Nusselt number will be a function given by Equation (6.13). The data was well correlated by a function of the form:

$$Nu_{pred,cyl} = C_1 Ar^{C_2} \frac{d_s}{d_p} \tag{6.15}$$

Constants C_1 and C_2 were evaluated by minimizing the root mean square error (RMSE). A value of zero would correspond to a perfect fit.

$$RMSE = \sqrt{\frac{\sum_{i=1}^{N} \frac{\left(Nu_{exp,i} - Nu_{pred,i}\right)^2}{Nu_{exp,i}^2}}{N-1}} \qquad (6.16)$$

$N \equiv$ Sample Set

The constants C_1 and C_2 were calculated to be 1.31 and 0.14 respectively with an RMSE = 0.130. Less than 15% of the data fell outside of the estimated error. Equation (6.15) can be re-written with the constants.

$$Nu_{pred,cyl} = 1.31 Ar^{0.14} \frac{d_s}{d_p} \qquad (6.17)^1$$

The reliability of a correlation is greatly improved if it can also predict the data not employed in its development. An effort was made to compare the predictions from the present correlation of Equation (6.17) and the data of various investigators, as well as hot bed data presented in Table 6.2 . This is graphically displayed in Figure 6.5.

Table 6.2 – Relevant Data from Referenced Experiments

Reference	Material	Ar	d_p (μm)	d_s (mm)	Bed Temperature
Grewal & Saxena [7]	Silica sand	432	167	12.7	Ambient
	Silicon carbide	631	178	12.7	Ambient
	Alumina sand	2425	259	12.7	Ambient
	Silicon carbide	5342	362	12.7	Ambient
	Silica sand	8513	451	12.7	Ambient
	Silica sand	11880	504	12.7	Ambient
Stojanović & Stojiljković [24]	Quartz sand	1126	300	16	Ambient
Rasouli *et al.* [9]	Silica sand	740	200	15	Ambient
	Silica sand	2735	307	15	Ambient
Koundakjian [3]	Aluminum Oxide	246	254	1.27–6.35	300°C

[1] Result published in [20]. Presented at the 18th International Conference on Fluidized Bed Combustion, May 25, 2005, Toronto, Canada

Examining Figure 6.5, it can be seen that Equation (6.17) predicts the Nusselt number within the estimated ±15% error for 85% of the experimental data. However, larger cylinders with d_s = 7.94 and 9.53mm tested stray away from the +15% error line for almost all grit sizes where Equation (6.17) over-predicts the Nusselt number by approximately 23%. The reason for this is explained in Section 6.2.2. Examining the reference data in Figure 6.5, it is observed that the correlation predicts the Nusselt number fairly well for experiments tested in sand particles d_p < 307μm or alternatively Ar < 2700. It is evident that sand properties with a larger d_p and Ar significantly under-predict the Nusselt number for the referenced data. This would be expected since the referenced tests were conducted on larger cylinders (d_s > 12.7mm) and Nusselt number trends for large tubes behave differently than small ones; furthermore, larger sand particles decrease h considerably. Nevertheless, the correlation can be considered to be satisfactory for small cylinders and larger cylinders in a bed within the Ar range tested. The effect of cylinder diameter on Nusselt number is discussed further in Section 6.2.2.

6.2.2 EFFECT OF CYLINDER DIAMETER ON NUSSELT NUMBER

The heat transfer along the circumference of a tube varies because the local fluid dynamics vary around the tube. Therefore, the heat transfer analyses and calculations for the tubes are complicated. Due to the flow resistance of a horizontally immersed tube to fluidizing medium a defluidized 'particle cap' of solids forms on the top of the tube shown in Figure 6.6 [25]. The size and height of the cap depend on the tube size and its surface conditions and the particle characteristics, such as diameter, density and sphericity. At the bottom of the tube, Glass and Harrison [26] observed a thin film of air approximately 0.5mm for their experiments. This suggests that a gas bubble is trapped on the upstream side preventing the cap from being

displaced by bubbles rising across the tube. Doherty *et al.* [27] emphasized that the gas trapped on the upstream side of the tube increased with the tube diameter and played an important role in establishing the value of h_{avg}. Saxena [1] supports this observation and reports that for a horizontal tube the surface voidage, ε_s, values were smallest at the top or down stream side of the tube, largest and identical at the two lateral sides of the tube, and intermediate at the bottom of upstream side of the tube. Figure 6.7 illustrates the results for a tube with a d_s = 50.8mm of ε_s and bulk bed voidage, ε_b, as a function of U/U_{mf} at angular positions of 0°, 60°, 180°, and 300° [1]. It can be seen that at each of the four positions the voidage increased with an increase in fluidizing velocity above U_{mf}, with each position varying in rate of increase. These results have an important effect on h_{avg} for a horizontal tube of d_s. Doherty *et al.* [27] explained the decrease in h_{avg} as d_s increased on the basis of an increase in particle residence time with the increase in tube diameter, and as a result the temperature difference between the tube and the particle decreases. This reduction in driving force brings about a reduction in the heat transfer coefficient. For small tube diameters the particle cap would have little effect on the local surface heat transfer coefficient. This is because smaller cylinders would form very small particle caps where fresh particles would replace them more frequently than for larger tubes. With the entire tube surface exposed to good particle motion around it, the local surface heat transfer would be more equally distributed. This suggests Nusselt number trends for smaller tube diameters would behave differently than those for larger tube diameters where the particle cap would increase and influence the heat transfer coefficient. Most of the literature reported investigates larger tube diameters immersed in fluidized bed; therefore, bed behaviour around the surface of a small immersed tube is still uncertain. However, the understanding of this dependence of h_{avg} on d_s involves a detailed interpretation of the changing hydrodynamic condition of the bed,

particularly in relation to solids motion and related bubble dynamics which is discussed further in [27].

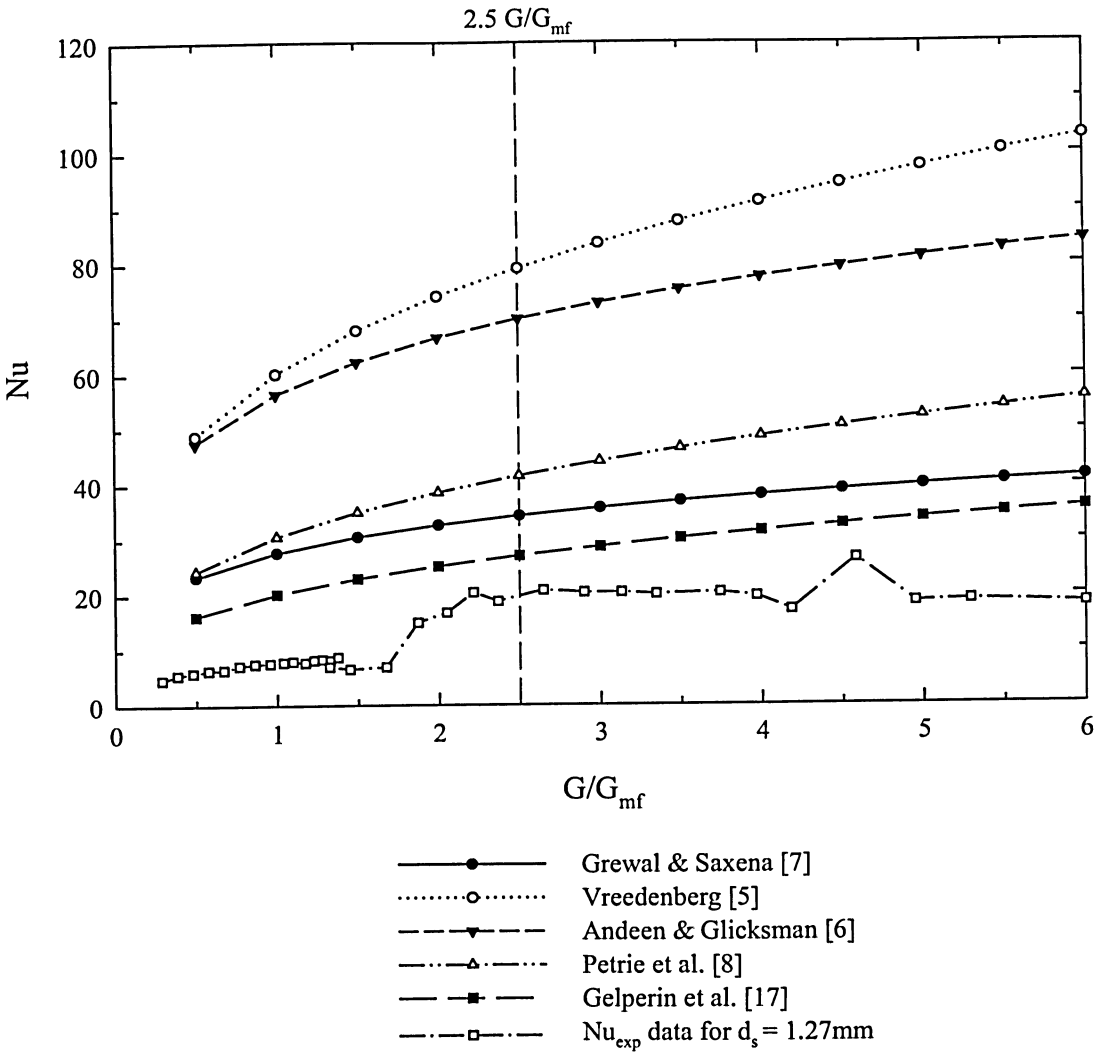

Figure 6.1 – Predicted Nusselt Number for Standard Correlations and Experimental Nusselt Number Data for d_s = 1.27mm in a Bed of d_p = 330μm

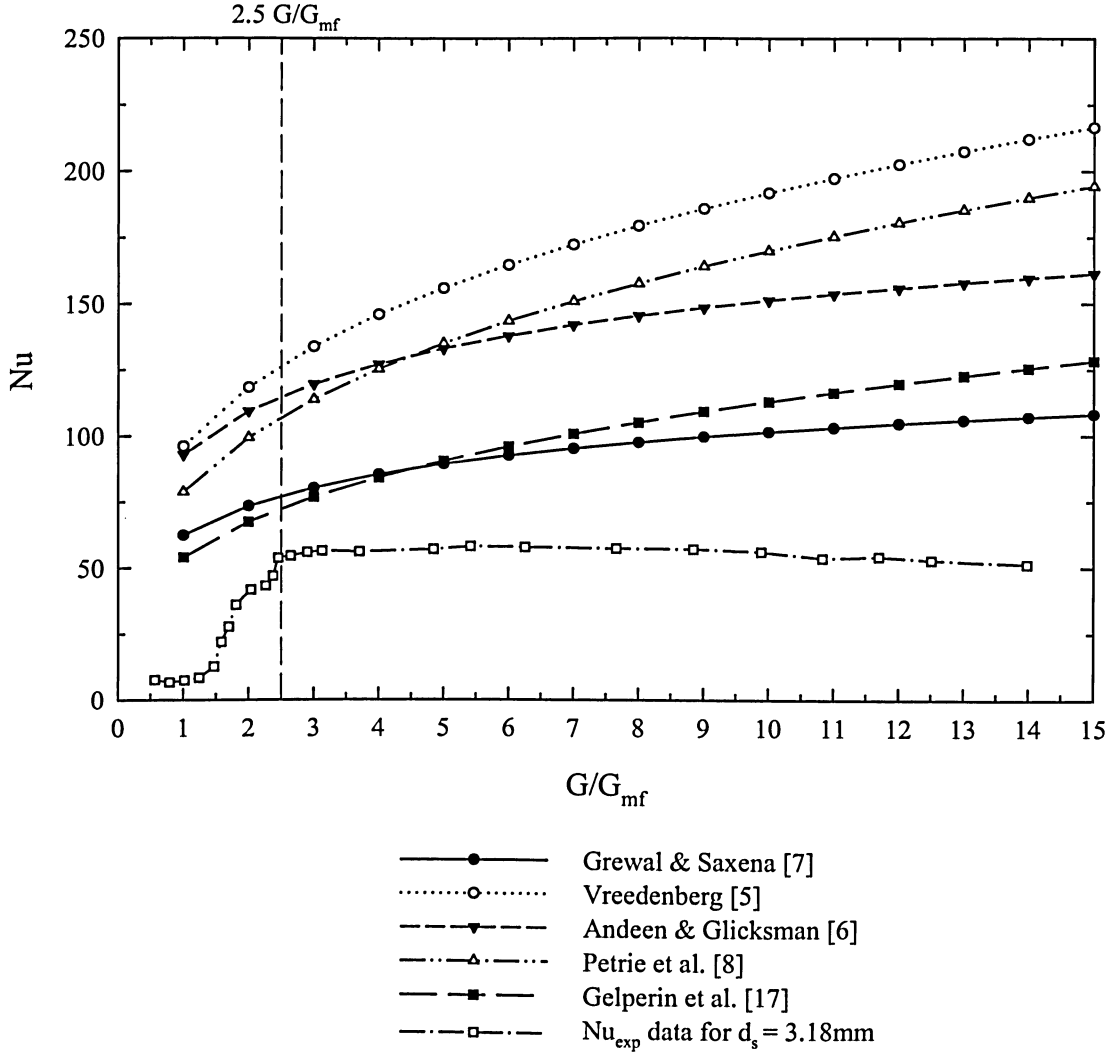

Figure 6.2 – Predicted Nusselt Number for Standard Correlations and Experimental Nusselt Number Data for $d_s = 3.18$mm in a Bed of $d_p = 200\mu$m

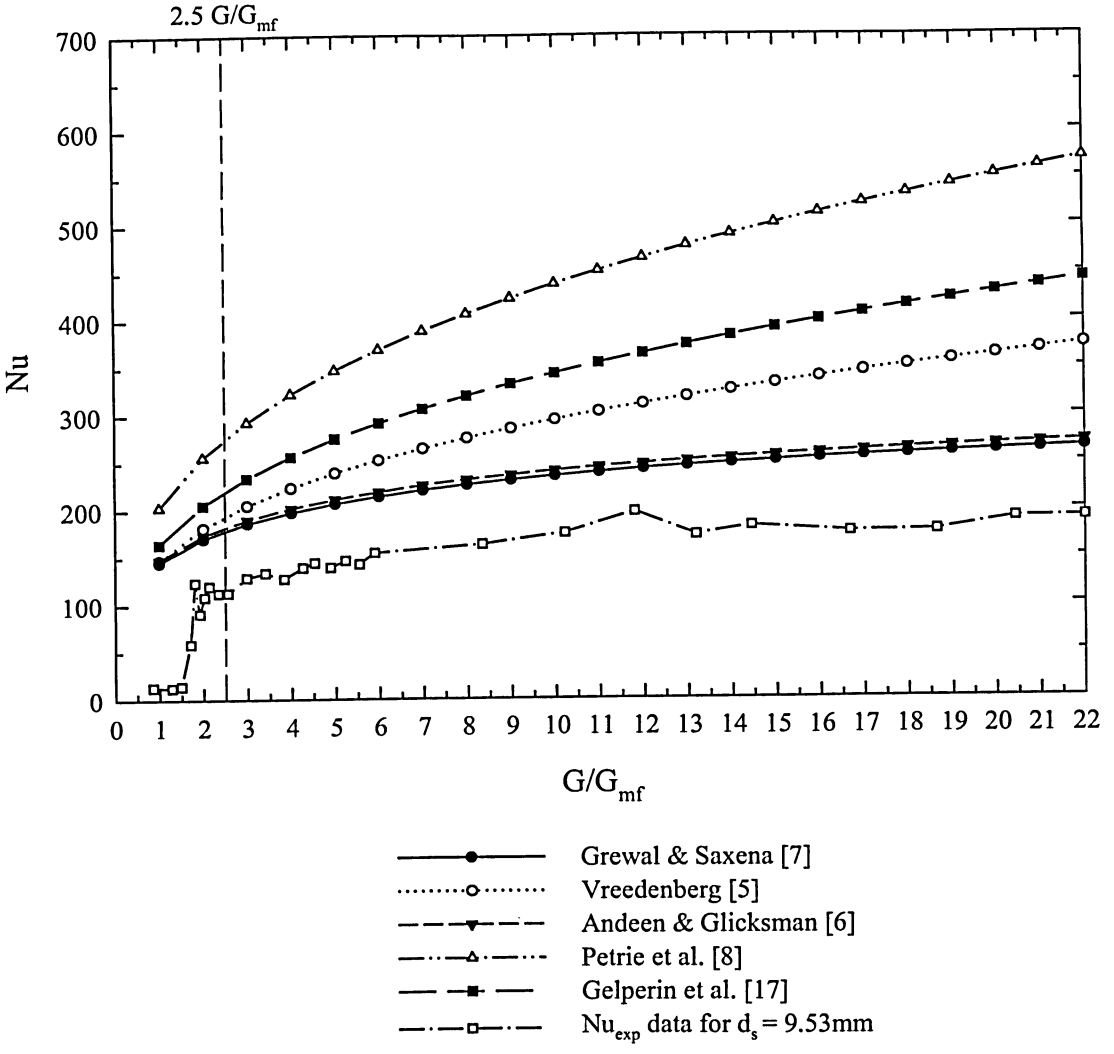

Figure 6.3 – Predicted Nusselt Number for Standard Correlations and Experimental Nusselt Number Data for d_s = 9.53mm in a Bed of d_p = 145μm

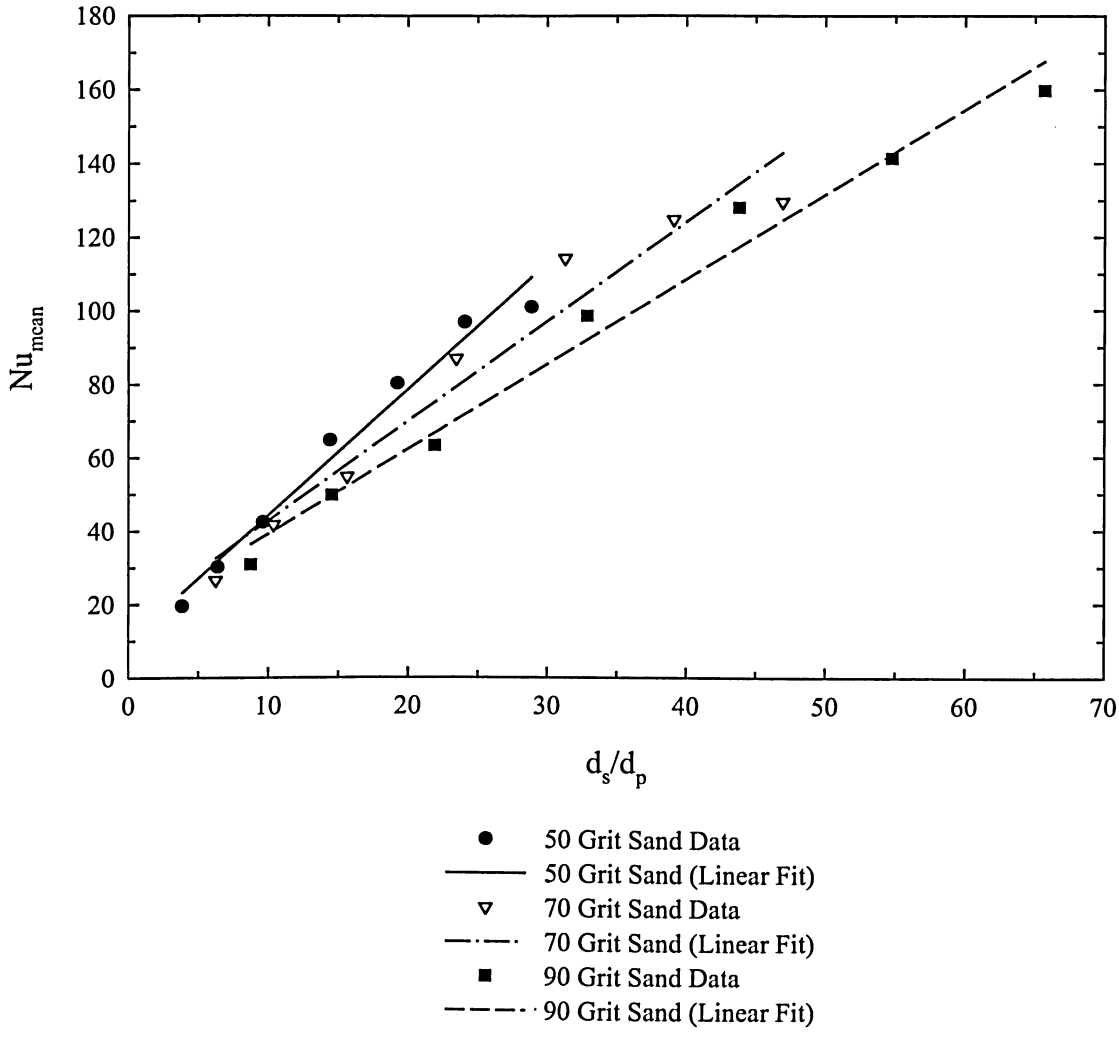

Figure 6.4 – Mean Nusselt Number vs. d_s/d_p for all Cylinders in 50, 70 and 90 Grit Data

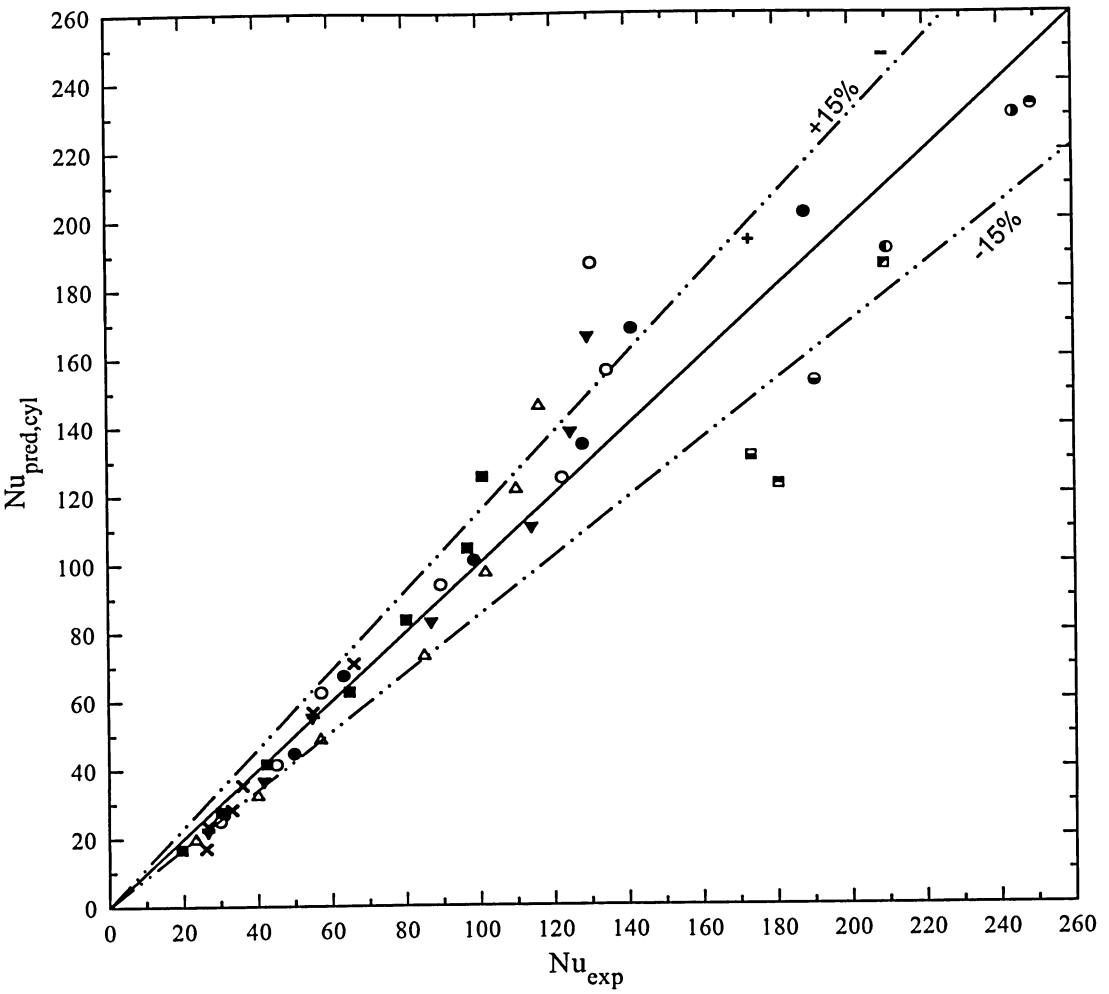

- d_p = 145μm (90 Grit Sand) Experimental Data
- d_p = 165μm (80 Grit Sand) Experimental Data
- d_p = 203μm (70 Grit Sand) Experimental Data
- d_p = 254μm (60 Grit Sand) Experimental data
- d_p = 330μm (50 Grit Sand) Experimental Data
- d_p = 254μm Hot Bed (300°C) Data [3]
- d_p = 167μm Silica Sand, d_s = 12.7mm [7]
- d_p = 178μm Silicon Sand, d_s = 12.7mm [7]
- d_p = 259μm Alumina Sand, d_s = 12.7mm [7]
- d_p = 362μm Carbide Sand, d_s = 12.7mm [7]
- d_p = 451μm Silica Sand, d_s = 12.7mm [7]
- d_p = 504μm Silica Sand, d_s = 12.7mm [7]
- d_p = 300μm Quartz Sand, d_s = 16mm [24]
- d_p = 200μm Silica Sand, d_s = 15mm [9]
- d_p = 307μm Silica Sand, d_s = 15mm [9]

Figure 6.5 – Predicted Nusselt Number vs. Experimental Data for all Cylinders and Referenced Data

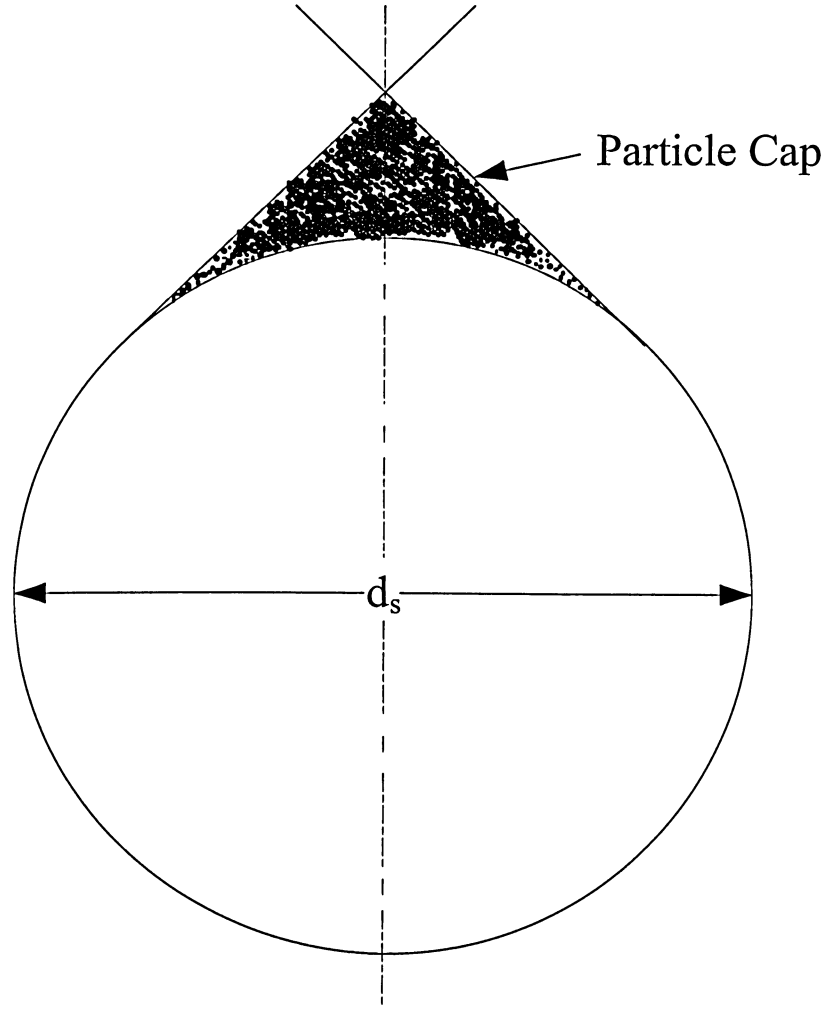

Figure 6.6 – 'Particle Cap' at the Top of Horizontally Immersed Tube (Adapted from Wang *et al.* [23])

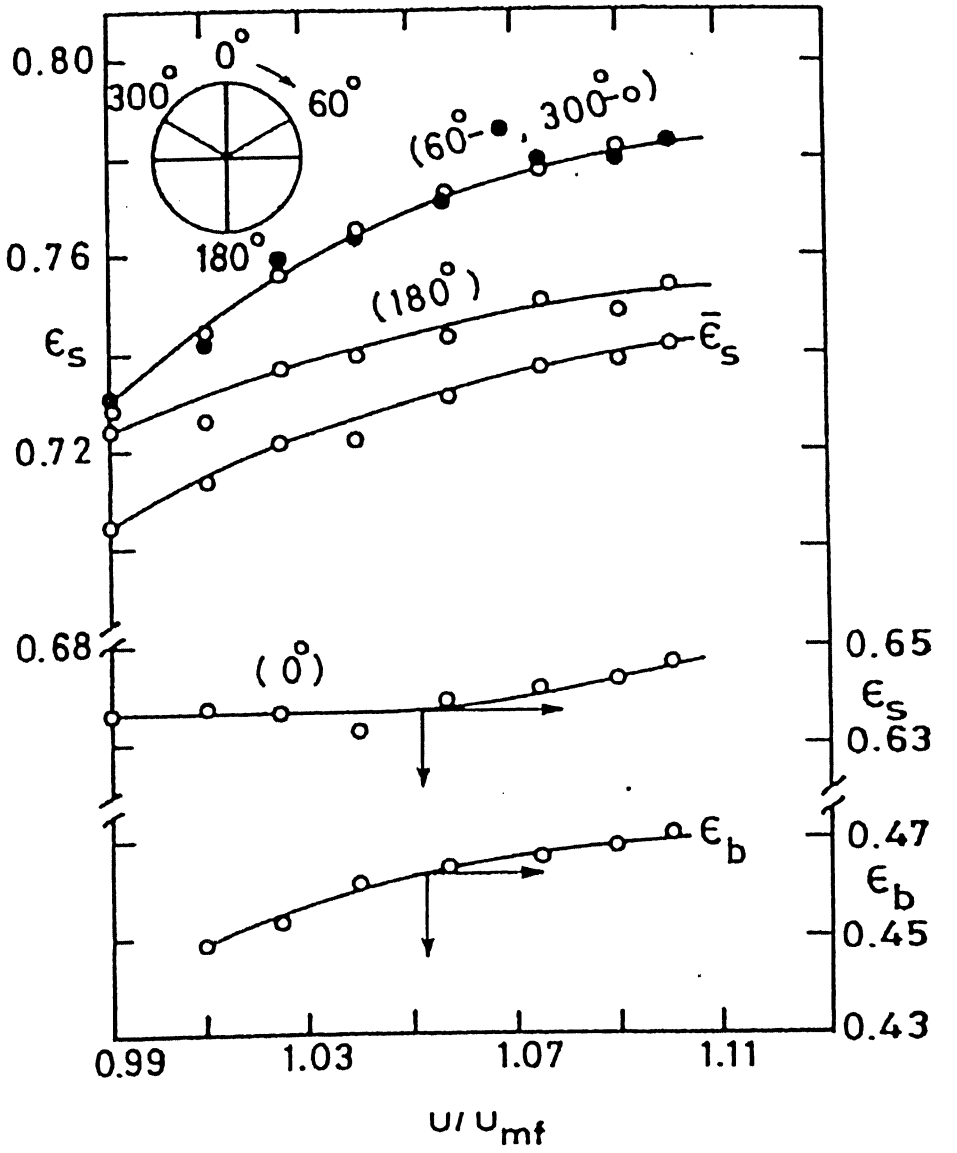

Figure 6.7 – Variation of ε_s at Four Peripheral Positions (0°, 60°, 180°, and 300°) for a d_s = 50.8mm glass tube, and ε_b as a Function of U/U_{mf} (Adapted from Saxena [1])

6.3 FLAT STRIPS IMMERSED IN A FLUIDIZED BED

Objects such as spheres, tubes, walls and flat plates immersed in fluidized bed have been well investigated [1, 2, 4, 28, 29, 30], but thin flat strips immersed in fluidized bed is an area less studied. Correlating the experimental data and the effects of sample width and orientation on Nusselt number will be discussed.

6.3.1 CORRELATING EXPERIMENTAL DATA

From the results and dimensional analysis discussed earlier in Chapter 5 and Section 6.1 respectively, the influencing factors for heat transfer of the immersed strip in a fluidized bed are the geometry, namely the width of sample w_s, the orientation of the sample θ_o and particle size d_p corresponding to their respective Archimedes number Ar. The following steps summarize the approach taken to develop a suitable correlation for all the flat strip data.

For each orientation tested Nu_{mean} was plotted versus $Ar^n w_s/d_p$ for all data, shown in Figure 6.8 to 6.10. It is observed from the figures that a function of the following form best fits the data set within a ±15% error.

$$y = C_1 \ln(x) - C_2 \tag{6.18}$$

The constant n = 0.2 was chosen as a preliminary value and was adjusted accordingly further into the analysis. The geometric factor (θ_o, angle orientation) was incorporated into constants C_1 and C_2 by plotting them versus their respective orientation, illustrated in Figure 6.11. It is shown in the figure that the constants have a linear relationship with the orientation of the form:

$$C_1 = A\theta_o + B \tag{6.19}$$

$$C_2 = D\theta_o + E \tag{6.20}$$

Combining Equations (6.20) and (6.19) into (6.18) gives:

$$y = (A\theta_o + B)\ln(x) - (D\theta_o + E) \tag{6.21}$$

or re-written:

$$Nu_{pred,strip} = (A\theta_o + B)\ln\left(Ar^n \frac{w_s}{d_p}\right) - (D\theta_o + E) \tag{6.22}$$

Constants A, B, D, E and n were adjusted by minimizing the root mean square error (Equation (6.16)). The constants were evaluated to be 1.12, 75, 4.70, 266 and 0.2 respectively with an RMSE = 0.0604. Substituting the constants into Equation (6.22) and re-arranging gives:

$$Nu_{pred,strip} = \theta_o\left[0.892\ln\left(Ar^{0.2}\frac{w_s}{d_p}\right) - 4.19\right] + 75\ln\left(Ar^{0.2}\frac{w_s}{d_p}\right) - 266 \tag{6.23}$$

$$\theta_o = 0°, 15°, 30°, ..., 90°$$

As shown in Figure 6.12, the data are well correlated by Equation (6.23). An effort was made to test the proposed correlation with published experimental data (wall and plate heat transfer in a fluidized bed), but was unsuccessful due to the lack of available information.

6.3.2 EFFECT OF STRIP WIDTH AND ORIENTATION ON NUSSELT NUMBER

The fluid dynamics around an immersed object strongly influences the heat transfer coefficient in a fluidized bed. If the heat transfer is to be good then the surface of the object needs to be brought into contact as rapidly as possible with fresh particles and thus, a defluidized part of the bed near the object would be detrimental to good heat transfer [31]. As discussed in Section 6.2.2, a 'particle cap' forms on the top of a tube due to the flow resistance of the immersed object in the fluidizing medium. This concept can be extended to immersed flat strips. Results reported in Chapter 5 and Equation (6.23) show the Nusselt number at a minimum for a

horizontal strip (0°) and at a maximum for a vertical strip (90°). Intuitively, it is expected that a particle cap would form on the top surface of the strip at a horizontal position whereas the particles for a strip at a vertical position would be continually replaced by fresh particles by the rising bubbles, significantly increasing the overall heat transfer. Furthermore, the width of the sample would considerably affect the upstream flow of bubbles and to some degree, affect the heat transfer. The understanding of this dependence of h on w_s involves a detailed interpretation of the changing hydrodynamic condition of the bed, particularly in relation to solids motion and related bubble dynamics, which is beyond the scope of this work.

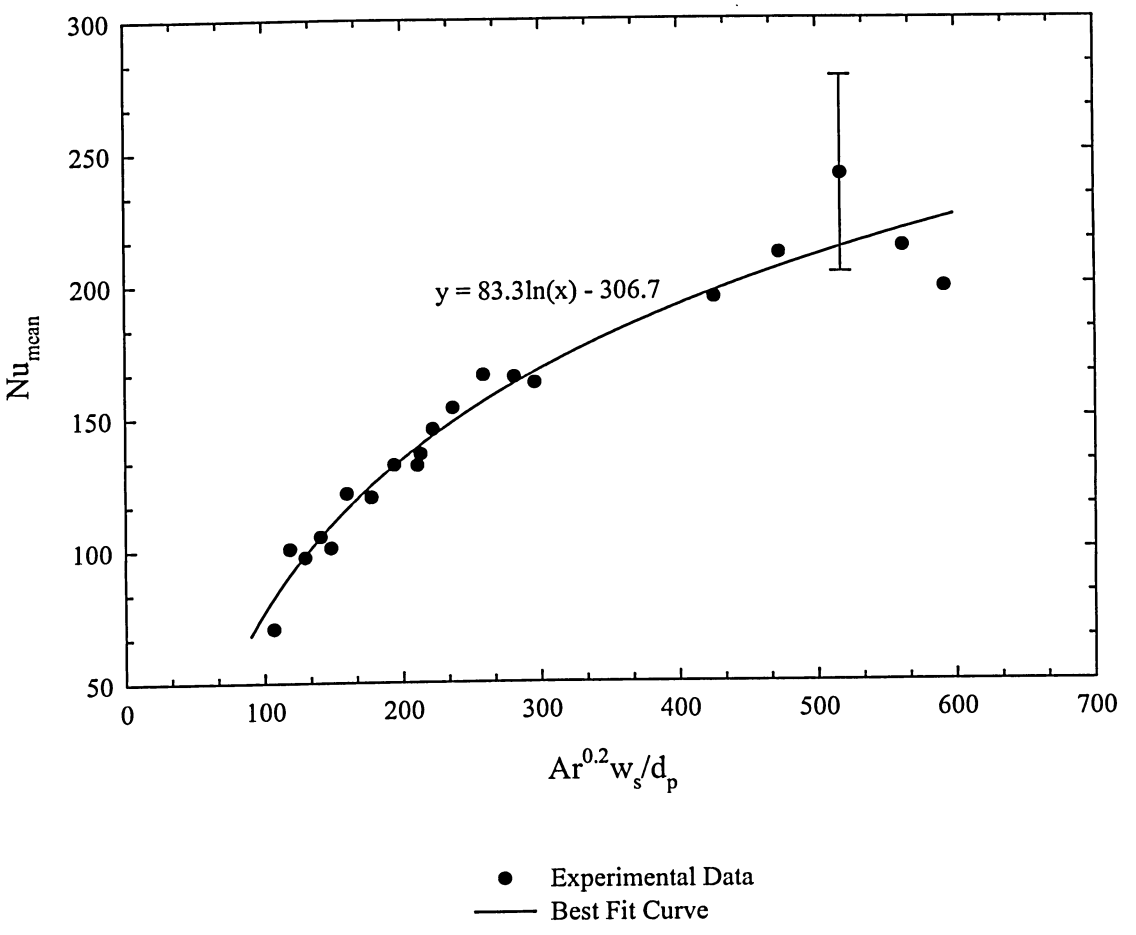

Figure 6.8 – Mean Nusselt Number vs. $Ar^{0.2}w_s/d_p$ for all Experimental Data at 0°

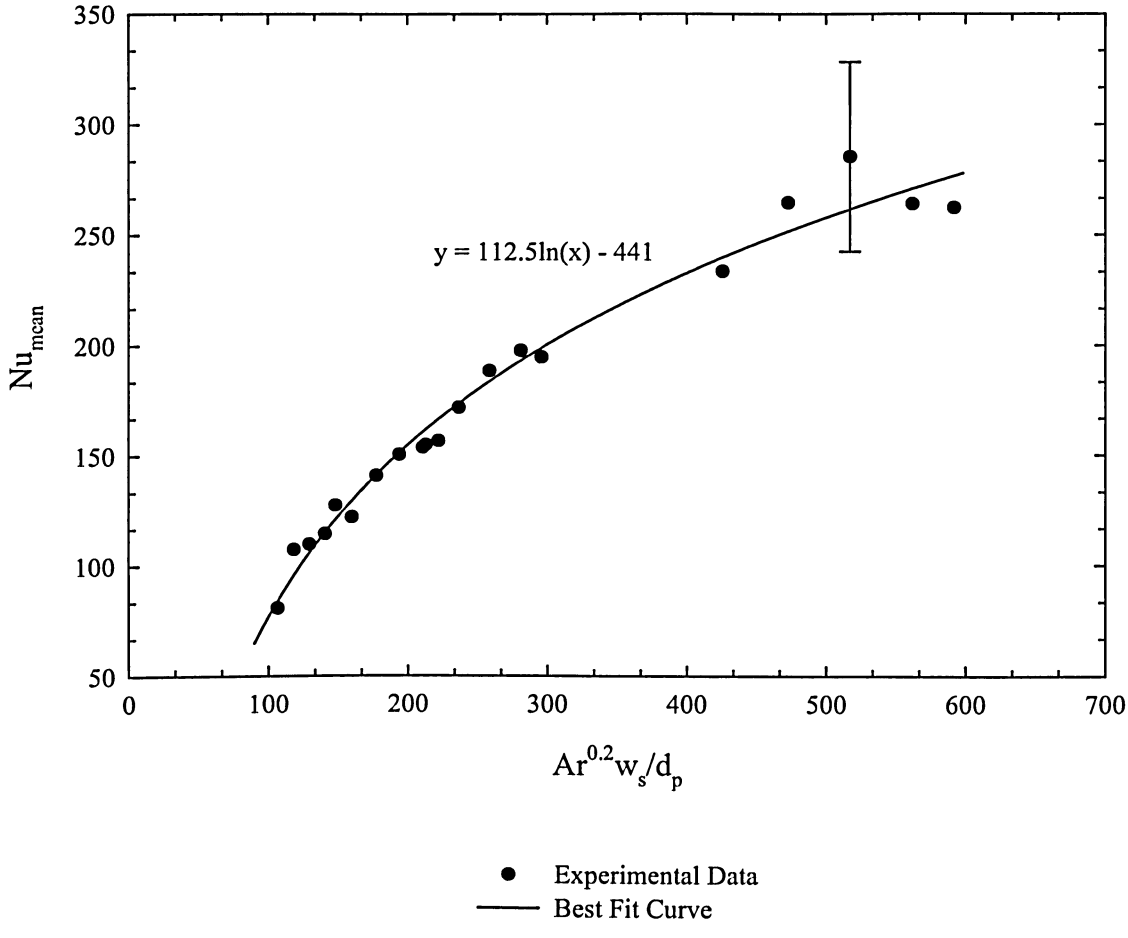

Figure 6.9 – Mean Nusselt Number vs. $Ar^{0.2}w_s/d_p$ for all Experimental Data at 45°

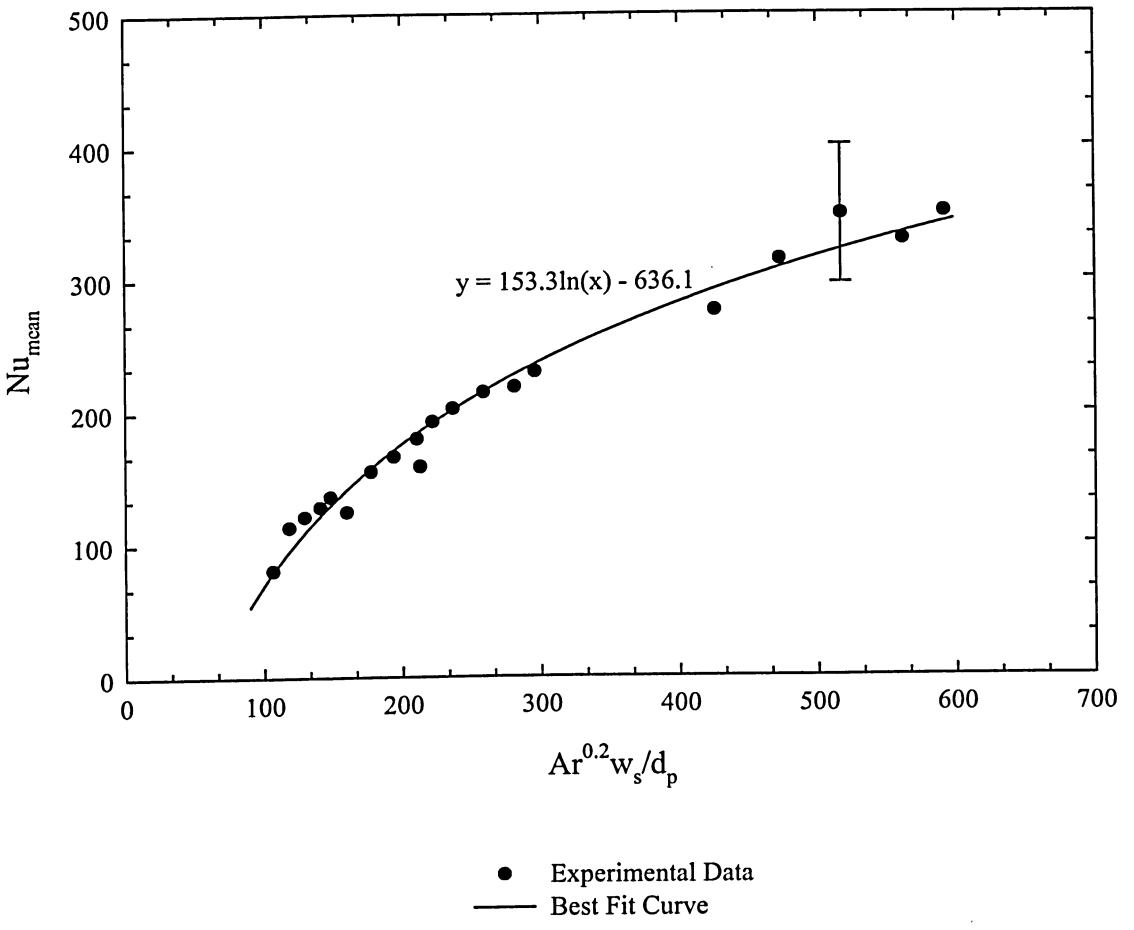

Figure 6.10 – Mean Nusselt Number vs. $Ar^{0.2}w_s/d_p$ for all Experimental Data at 90°

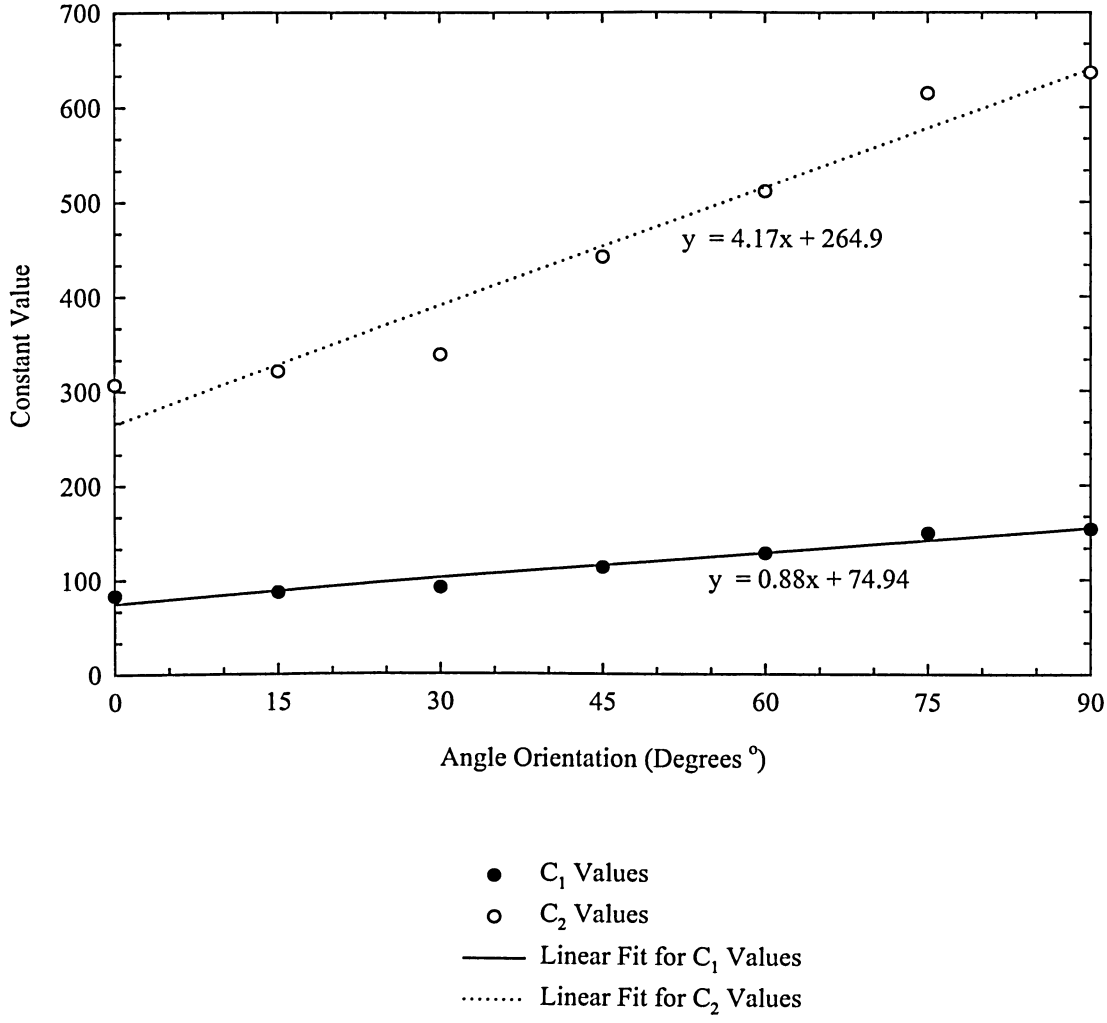

Figure 6.11 – Linear Representation for Constant Values with respect to Angle Orientation

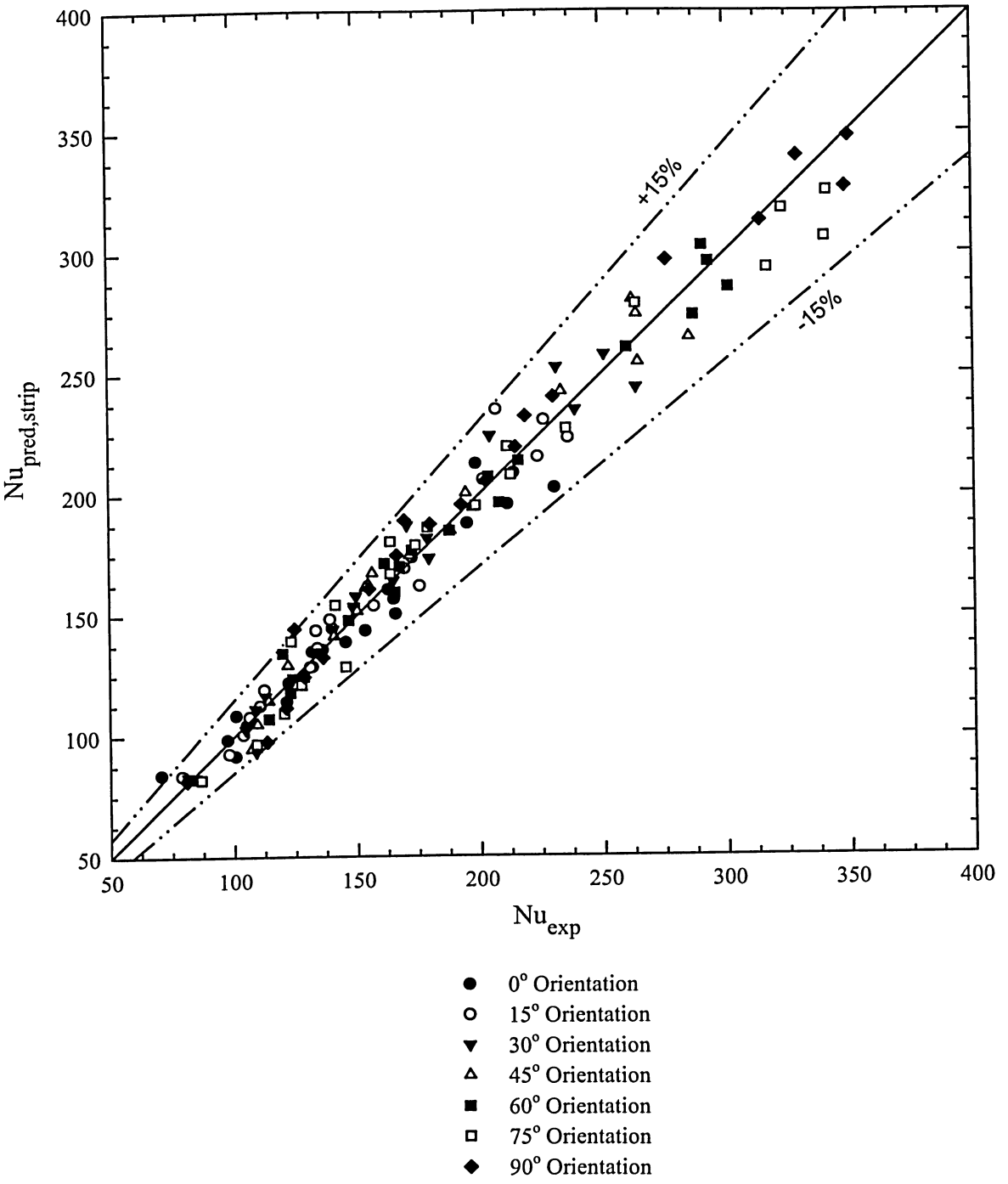

Figure 6.12 – Predicted Nusselt Number vs. Experimental Data for all Data

CHAPTER SEVEN

UNCERTAINTY ANALYSIS

Conducting an uncertainty analysis provides the experimenter a rational way of evaluating the major contributors of error in the results. It also allows the experimenter to modify experimental equipment, procedure and analysis such that the results are described to be "good" within a predicted error range. This chapter discusses the uncertainty in experimental results.

7.1 AIR FLOW UNCERTAINTIES

The air flow rate was measured with a rotameter (low flow rate) and two venturis (mid and high flow rates). The following expression was used to determine the flow rate through the venturi:

$$Q = C_v A_T \sqrt{\frac{2\Delta P}{\rho_g \left(1-\beta^4\right)}} \tag{7.1}$$

The uncertainty in the discharge coefficient, C_v, provided by the venturi manufacturer was estimated to be ±0.5%. The inlet flow conditions depend on the installation and conversely affect the discharge coefficient. The venturi sections of the pipe were installed with no inlet flow disturbances. The uncertainty in throat area, A_T, is negligible since its diameter is manufactured

within a ±0.0254mm (±0.001") tolerance or better than ±0.001% uncertainty. This uncertainty yields a negligible effect on the total uncertainty in the flow rate. The uncertainty in the rotameter is limited by the user's ability to read the rotameter scale accurately. This uncertainty has been estimated to be approximately ±0.1SCFM. The pressure drop across the 1" venturi meter was measured with a U-tube manometer. The 2½" venturi meter was measured with a U-tube manometer and a differential pressure gauge. The differential pressure gauge is reported by the manufacturer [32] to have an accuracy of ±2%. The uncertainty in the pressure drop for the U-tube manometers is limited by the user's ability to read the manometer accurately, estimated to be approximately ±0.1"WC. The inlet air density is calculated from the ideal gas law where the inlet pressure and temperature were measured. A Bourdon gauge measured the inlet pressure which has an accuracy of ±5% of full-scale reading. The measured value of the inlet temperature had an uncertainty of ±2°C resulting in an uncertainty of 0.0015kg/m^3 or 0.1% for the inlet air density. The uncertainty of the last term appearing in Equation (7.1), β, is negligible because of tight tolerances on the venturi flow meters.

The relative uncertainty in the flow rate measurements is found by applying the procedure outlined in [33]:

$$W_Q = \left\{ \left(\frac{\partial Q}{\partial C_v} w_{C_v} \right)^2 + \left(\frac{\partial Q}{\partial A_T} w_{A_T} \right)^2 + \left(\frac{\partial Q}{\partial \Delta P} w_{\Delta P} \right)^2 + \left(\frac{\partial Q}{\partial \rho_g} w_{\rho_g} \right)^2 + \left(\frac{\partial Q}{\partial \beta} w_{\beta} \right)^2 \right\}^{1/2} \qquad (7.2)$$

Evaluating each of the terms in Equation (7.2) gives $W_Q = 0.5$ CFM or 1.95%.

The parameter contributing to the majority of error in the calculated W_Q is the measured pressure difference across the venturi meters and rotameter, which are subject to individual inconsistency. Knowing the air flow rate, the fluidizing gas mass flux, G, could be calculated using Equation (2.10). It is repeated below:

$$G = \frac{\rho_g Q}{A_b} \tag{7.3}$$

The effective bed area, A_b, is the area bounded by the shell walls ($0.07604 m^2$). Overall, the average uncertainty associated with the mass flux was ±2.0%.

7.2 TEMPERATURE MEASURING UNCERTAINTIES

Errors arising from temperature measurement depend on the accuracy of the thermocouple and the data acquisition system. The accuracy of the K type thermocouple is reported by the manufacturer [34] to be about ±2.2°C or 0.75% when measuring temperatures from 0 to 1250°C. The accuracy of the TempBook is ±1.5°C when measuring temperatures from 0 to 100°C (Operator's Manual). These inaccuracies were acceptable for this experiment because the temperature was recorded when a difference of 15 to 20°C between the sample and bed temperatures were observed. Furthermore, temperature measurements were recorded when all monitored temperatures remained in a ±1°C range respectively in a five minute time span. This criterion ensured steady state errors to be less than 1°C. The temperature difference between the terminals and bed temperature took a considerably long time to reach steady state due to the size of the terminals. The excess terminal temperature (θ_T) was less than 3°C for all runs. Conduction losses ("fin" effects) for the center thermocouple of the flat strip samples were kept to a minimum (discussed in Chapter 3) and were estimated to be less than 2%. Considering the errors discussed above, the uncertainty of the measured temperature difference between the surface of the sample and the bulk of the bed was ±2.25°C and ±1°C for θ_T.

7.3 HEAT TRANSFER UNCERTAINTIES

The variables recorded during the capturing of steady state temperatures that could effect the heat transfer calculation included the voltage drop across the sample and the supplied current. For all the samples tested, a digital multimeter model GDM-8145 was used to measure the voltage across the sample. According to the manufacturer, the accuracy of the voltmeter is ±0.1%. The current to resistively heat the samples was supplied by a GW Instek Programmable Power Supply model PSH-10100 at constant voltage. The manufacturer reports the accuracy of the displayed current to be ≤0.2% or +90mA. All samples were resistively heated to satisfy the $\Delta T \approx 15°C$ condition. Having considered these sources of uncertainties, the uncertainty in the power dissipation term is estimated to be ±0.3%.

The heat transfer coefficient values were determined by varying h in Equation (5.16) until T(0) matched the measured T_s using Mathcad 2001 Professional, discussed in Section 5.1. Equation (5.16) is simplified and re-arranged below for further analysis:

$$\Delta T = \left[\theta_T - \frac{VI}{LhP}\right] \frac{1}{\cosh\left(\sqrt{\frac{hP}{kA_c}}\frac{L}{2}\right)} + \frac{VI}{LhP} \tag{7.4}$$

where,

$$\theta_T = T_T - T_\infty$$
$$\Delta T = T_s - T_\infty$$

Equation (7.4) presents h implicitly for the temperature distribution model at x = 0 (sample center). Solving Equation (7.4) for h yielded a root function making it difficult to take the partial derivative of the respective variables for the uncertainty analysis. Taking a look at the variables that influence the heat transfer coefficient, the majority of uncertainties in h would arise from the measured temperatures, namely T_s, T_T, and T_∞ which appear in the θ_T and ΔT terms. The sample

geometry parameters P, A_c and L, along with the sample thermal conductivity k, were constant for each run. Their uncertainties are considered insignificant compared to those measured during the experimental runs. To further simplify the analysis the terminal excess temperature (θ_T) uncertainty will be ignored. Its influence on the overall uncertainty in h is unknown.

The overall uncertainty in the heat transfer coefficient is calculated using the expression $h = \frac{VI}{A_s \Delta T}$ and by applying the procedure outlined in [33]:

$$W_h = \left\{ \left(\frac{\partial h}{\partial V} w_V \right)^2 + \left(\frac{\partial h}{\partial I} w_I \right)^2 + \left(\frac{\partial h}{\partial \Delta T} w_{\Delta T} \right)^2 + \left(\frac{\partial h}{\partial A_s} w_{A_s} \right)^2 \right\}^{1/2} \tag{7.5}$$

Table 7.1 demonstrates the evaluated results of Equation 7.5 for various samples tested. The uncertainty in h varied from experiment to experiment within a range of 10 to 20%.

Table 7.1 – Uncertainty in h for Various Samples Tested

Sample	V (V)	w_V	I (A)	w_I	ΔT	$w_{\Delta T}$	h (W/m^2-K)	W_h	% Uncertainty
6.35mm Flat Strip	0.8543	±0.0008	17.01	≤0.0034	12.45	±2.25	338.5	61.2	18.1
25.4mm Flat Strip	1.0761	±0.0011	85.02	≤0.017	17.086	±2.25	415.6	54.7	13.2
9.35mm Cylinder	0.7497	±0.0007	80.01	≤0.016	13.79	±2.25	586.6	95.7	16.3
2.11mm Cylinder	0.7368	±0.0007	5.00	≤0.001	17.55	±2.25	122.9	15.8	12.8

It should be noted that estimating the heat transfer coefficient using the simple expression $h = \frac{VI}{A_s \Delta T}$ resulted in a 10% error with the temperature distribution model presented in Chapter 5. This simplified model assumes insulated ends and uniform sample temperature. The above result was used as an estimate of uncertainty in the measured heat transfer coefficient.

7.4 NON-QUANTIFIABLE UNCERTAINTIES

The heat transfer coefficient of an immersed object in a fluidized bed is affected by many parameters including its characteristic length (d_s, w_s), the fluidizing mass flux (G), the mean diameter of the sand (d_p) and Archimedes number (Ar). The uncertainties in these parameters can be analyzed and given proper values, but other factors like the location and the frequency of the rising bubbles in the fluidized bed, as described by the bed voidage (ε), cannot be quantified easily.

Theoretically, bubble location and formation will form randomly throughout the bed. The air bubbles originate at the porous tiles and grow by coalescence with other bubbles rising through the bed and then bursting at the surface of the fine sand. Immersing an object within the bed would interfere with this fluidized bed behaviour, creating gas voids underneath the sample and particle caps at the top. Therefore, it is possible that bubbles form more often in some regions than in others and thus the bubble occurrence and location may not be truly random.

As discussed in Chapter 4, the procedure for temperature recording consisted of capturing the steady state temperature of the samples center and ends and bed temperature. The temperature readings were then averaged within the first half second of the recorded data. The probability that the bubbles for each test run would be the same is highly unlikely. Similarly the frequency of bubbles in the vicinity of the heat transfer surface would vary from one experiment to another. The nature of bubble location and frequency is uncontrollable resulting in some non-quantifiable uncertainties. However, tests of repeatability under fixed conditions produced RMS variations in the 2 to 5% range, thus suggesting that the above is not a serious matter.

The analysis itself includes some assumptions that may contribute to uncertainties. In deriving the temperature distribution (Equation (7.4)), the convective coefficient h is assumed to

be uniform over the surface. It is likely that the terminals holding the ends of the sample cause flow disturbances that alter the convection coefficients at the sample ends. The magnitude of this effect is non-quantifiable. Additionally, it has been assumed that no heat is generated in the sample portion that is in the terminals. As the terminals are large cross-section copper, this is likely a good assumption, except right near the point where the sample emerges from the terminals, where some heat will be generated as current funnels into the sample. However, this is not expected to be significant.

CHAPTER EIGHT

CONCLUSIONS AND RECOMMENDATIONS

8.1 CONCLUSIONS

The heat transfer coefficients for small size cylinders and flat strips immersed in a fluidized bed have been determined by carrying out experiments in a lab-scale fluidized bed of various fine sand sizes. In addition, a correlation that predicts the mean Nusselt number within ±15% was developed for each object geometry.

8.1.1 SMALL CYLINDERS IMMERSED IN A FLUIDIZED BED

Heat transfer results for small cylinders immersed in a fluidized bed were presented in Section 5.2. A consistent trend was observed for the smaller cylinders tested. At fluidizing rates between 0.14 and 1 G/G_{mf}, little or no change of the Nusselt number was observed for all tested samples and sand size. As the fluidizing velocity increased, the particle residence time decreased due to the rising bubbles and higher bed porosity, effectively increasing the Nusselt number rapidly up to a point (approximately $2.5 \times G_{mf}$) where it plateaued within a ±5 - 10% range to the maximum flow rate tested for that sample. Larger cylinders tested showed a slightly different trend at higher fluidizing gas rates where the Nusselt number continued to increase monotonically, similar to that seen with larger tubes. For all cases, a mean Nusselt number was

evaluated and plotted versus the mean particle diameter. The plotted results showed that the mean Nusselt number decreased as the mean particle diameter increased, indicating that better particle motion around the cylinder and hence higher heat transfer rates were attained by smaller particles. This is because, for larger particles, the effective thicknesses of the gas film increases while the surface to volume ratio decreases, a trend observed by many previous researchers.

It was also observed that the mean Nusselt number increased with increasing cylinder diameter. In part, this is due to an increase in particle residence time with the increase in tube diameter, resulting in the temperature difference between the tube and the particles decreasing.

A correlation that predicts the mean Nusselt number within ±15% was developed for the small cylinder data. Data reported by various researchers [3, 7, 9, 24] for a range of tube sizes in a variety of particle materials and sizes correlated well with the present correlation, as long as d_s is small or $Ar < 2700$.

The results obtained for small cylinders immersed in a fluidized bed in this thesis show that correlations developed for larger tubes do not extrapolate well for smaller sized cylinders on the order of 1 – 10mm diameter. Heat transfer data for cylinders in this range are critical in designing fluidizing bed systems for heat treating wire. However, there are areas that require further research and are discussed in Section 8.2.

8.1.2 FLAT STRIPS IMMERSED IN A FLUIDIZED BED

Heat transfer results for flat strips immersed in a fluidized bed were presented in Section 5.3. Similar trends to the small cylinder results were observed in Nu_{exp} versus G/G_{mf} plots for the small samples tested. The largest sample tested (25.4mm) showed a more pronounced increasing monotonic behaviour where no maximum was observed. The Nusselt number

increased approximately 15% from a flat horizontal position to a vertical position rotated along the center axis lengthwise. This result is due to better particle contact along the vertical surface of the strip where no particle cap would form on the top side and no gas voids would form at the bottom, whereas a horizontal strip would be more susceptible to particle cap and gas void formations.

A correlation that predicts the mean Nusselt number within 15% was developed for all flat strip data. A geometric factor taking into account the angle orientation was included. Due to the lack of work in this area of research, no other published experimental data were available to test the proposed correlation.

Heat transfer to flat strips immersed in a fluidized bed has not been studied by previous researchers because it does not have any obvious application in the power generation industry. However, an alternative to lead furnaces to heat treating steel straps is essential for future manufacturing, and, because a fluidized bed furnace is capable of high heat transfer rates, having knowledge of heat transfer to flat strips immersed in a fluidized bed is imperative for future design. Because this is a new area of research, further studies are required and are discussed in the following section.

8.2 RECOMMENDATIONS

Avenues worth investigating to further understand the heat transfer to immersed cylinders and flat strips in a fluidized bed are discussed.

One of the major influences of heat transfer to an object immersed in a fluidized bed is the changing hydrodynamic condition of the bed. Solids motion and bubble dynamics in a fluidized bed have been the focus for many investigators [9, 27, 35, 36, 37]. However, particle motion around small cylinders and thin flat strips has not been studied. Understanding bed behaviour would help quantify the bed voidage, an important parameter in the heat transfer process.

Hot bed tests should be done for the flat strips. Comparing cold and hot bed data would help identify discrepancies between the two bed conditions. This can be done by modifying the fluidized bed unit by including an electric heater at the inlet of the fluidizing air or by immersing the flat strip in a fluidized bed furnace.

Heat transfer data collected at low fluidizing rates were not analyzed in this thesis. This information could be useful in studying fluidizing conditions of packed beds.

REFERENCES

[1] Saxena, S.C., 1989, "Heat Transfer Between Immersed Surfaces and Gas-Fluidized Beds," Advances in Heat Transfer **19**, pp.97-190

[2] Baskakov, A.P., Berg, B.V., Vitt, O.K., Filippovsky, N.F., Kirakosyan, V.A., Goldobin, J.M. and Maskaev, V.K., 1973, "Heat Transfer to Objects Immersed in Fluidized Beds," Powder Technology **8**, pp.273-282

[3] Koundakjian, P., 2002, "Heat Transfer to Small Cylinders Immersed in a Fluidized Bed Heat Treating Furnace," MASc Thesis, University of Waterloo

[4] Botterill, J.S.M., 1975, "Fluid-Bed Heat Transfer: Gas-Fluidized Bed Behaviour and its Influence on Bed Thermal Properties," Academic Press, London

[5] Vreedenberg, H.A., 1958, "Heat Transfer Between a Fluidized Bed and a Horizontal Tube," Chem. Eng. Sci. **9**, pp.52-60

[6] Andeen, B.R. and Glicksman, L.R., 1976, "Heat Transfer to Horizontal tubes in Shallow Fluidized Beds," ASME Paper No. 76-HT-67

[7] Grewal, N.S. and Saxena, S.C., 1980, "Heat Transfer Between Immersed Surfaces and Gas-Fluidized Beds," Int. J. Heat Mass Transfer **23**, pp.1505-1519

[8] Petrie, J.C., Freeby, W.A. and Buckham, J.A., 1968, "In-bed Heat Exchangers," Chem. Eng. Prog. **64**(67), pp.45-51

[9] Rasouli, S., Golriz, M.R. and Hamidi, A.A., 2005, "Effect of Annular Fins on Heat Transfer of a Horizontal Immersed Tube in Bubbling Fluidized Beds," Powder Technology **154**, pp.9-13

[10] Yates, J.G., 1983, "Fundamentals of Fluidized-Bed Chemical Processes," Buttworths Monographs in Chemical Engineering, London

[11] Pell, M., 1990, "Gas Fluidization," Handbook of Powder Technology, Elsevier, NY

[12] Howard, J. R., 1989, "Fluidized Bed Technology: Principles and Applications," Adam Hilger, Bristol and New York

[13] Geldart, D., 1973, "Types of Gas Fluidization," Powder Technology **7**, pp.285-292

[14] Ergun, S., 1952, "Fluid Flow Through Packed Columns," Chem. Eng. Prog., **48**, pp.245

[15] Wen, C. Y. and Yu, Y. H., 1966, "A Generalized Method for Predicting the Minimum Fluidization Velocity," AIChEJ, **12**, pp.610-612

[16] Gupta, C. K. and Sathiyamoorthy, D., 1999, "Fluid Bed Technology in Materials Processing," CRC Press LLC, Florida

[17] Gelperin, N.I., Kruglikov, V.,Ya. and Ainshtein, V.G., 1966, "Heat Transfer Between a Fluidized Bed and a Surface," Int. Chem. Eng. **6**(1), pp.67-73

[18] Kunii, d. and Levenspiel, O., 1991, "Fluidization Engineering," 2nd Ed., Butterworth-Heinemann Newton, MA

[19] Incropera, F.P. and DeWitt, D.P., 1996, "Introduction to Heat Transfer," 3rd Ed., John Wiley & Sons Inc. NewYork, NY

[20] Friedman, J., Koundakjian, P., Naylor, D., and Rosero, D., 2005, "Heat Transfer to Small Horizontal Cylinders Immersed in a Fluidized Bed," ASME Paper No.HT-05-1147

[21] Molerus, O., 1992, "Arguments on Heat Transfer in Gas Fluidized Beds," Chemical Engineering Science **48**, pp.761-770

[22] Molerus, O. and Wirth, K. E., 1997, "Heat Transfer in Fluidized Beds," Chapman & Hall, London

[23] Wang, L., Wu, P., Zhang, Y., Yang, J., Tong, L. and Ni, X., 2004, "Effects of Solid Particle Properties on Heat Transfer between High-Temperature gas Fluidized Bed and Immersed Surface," Applied Thermal Engineering **24**, pp.2145-2156

[24] Stojanović, B. and Stojiljković, M., 1999, "The Influence of Fluidization Velocity on Heat Transfer Between Fluidized Bed and Inclined Heat Transfer Surfaces," The scientific journal FACTA UNIVERSITATIS, Series: Mechanical Engineering **1**(6), pp.703-710

[25] Wang, L., Ping, W. and Xuezhi, N., 2005, "Surface-Particle-Emulsion Model of Heat Transfer Between a Fluidized Bed and an Immersed Surface," Powder Technology **149**, pp.127-138

[26] Glass, D.H. and Harrison, D., 1964, "Flow Patterns Near a Solid Obstacle in a Fluidized Bed," Chemical Engineering Science **19**, pp.1001-1002

[27] Doherty, J.A., Verma, R.S., Shrivastava, S. and Saxena, S.C., 1986, "Heat Transfer from Immersed Horizontal tubes of different Diameter in a Gas Fluidized Bed," Energy **11**(8), pp.773-783

[28] Donsi, G. and Ferrari, G., 1995, "Heat Transfer Coefficients between Gas Fluidized Beds and Immersed Spheres: Dependence on the Sphere Size," Powder Technology **82**, pp.293-299

[29] Parmar, M.S. and Hayhurst, A.N., 2002, "The Heat Transfer Coefficient for a Freely Moving Sphere in a Bubbling Fluidized Bed," Chemical Engineering Science **57**, pp.3485-3494

[30] Pillai, K.K., 1976, "Heat Transfer to a Sphere Immersed in a Shallow Fluidized Bed," Letters in Heat and Mass Transfer **3**, pp.131-146

[31] Sinclair, R., Wright, J. C. J. and Thomas, C. G., 1964, "Flow Patterns Near a Solid Obstacle in a Fluidized Bed," Chemical Engineering Science **19**, pp.1001-1002

[32] Dwyer, www.dwyer-inst.com

[33] Holman, J.P., 1994, "Experimental Methods for Engineers," 6th Ed., McGraw-Hill, Inc. New York

[34] Omega Engineering, Inc., www.omega.ca

[35] Wang, X.S. and Rhodes, M.J., 2005, "A DEM Study of Particle Motion Near the Walls of Gas Fluidized Beds," Powder Technology **160**, pp.15-19

[36] Hamidiour, M., Mostoufi, N., Sotudeh-Gharebagh, R. and Chaouki, J., 2005, "Monitoring the Particle-Wall Contact in a Gas Fluidized Bed by RPT," Powder Technology **153**, pp.119-126

[37] Chen, J.C., Grace, J.R. and Golriz, M.R., 2005, "Heat Transfer in Fluidized Beds: Design Methods," Powder Technology **150**, pp.123-132

[38] Moffat, R. J., 1988, "Describing the Uncertainties in Experimental Results," Experimental Thermal and Fluid Science **1**, pp.3-17

[39] Botterill, J.S.M. and Desai, M., 1971, "Limiting Factors in Gas-Fluidized Bed Heat Transfer," Powder Technology **6**, pp.231-238

[40] Saxena, S.C. and Ganzha, V.L., 1985, "Dependence of Heat-Transfer Coefficient for Immersed Surfaces in a Gas-Fluidized Bed on Pressure," Powder Technology **44**, pp.115-124

[41] Chen, P. and Pei, D.C.T., 1984, "A Model of Heat Transfer Between Fluidized Beds and Immersed Surfaces," Int. J. Heat Mass Transfer **28**(3), pp.675-682

[42] Bordulya, V.A., Teplitsky, Y.S., Markevich, I.I., Hassan, A.F. and Yeryomenko, T.P., 1991, "Heat Transfer Between a Surface and a Fluidized Bed: Consideration of Pressure and Temperature Effects," Int. J. Heat Mass Transfer **34**(1), pp.47-53

[43] Leong, K.C., Lu, G.Q, Bhatia, S.K. and Rudolph, V., 1998, "Modelling of Heat Transfer in Fluidized-Bed Coating of Thin Plates," Chemical Engineering Science **53**(6), pp.1307-1310

[44] Gunn, D.J. and Hilal, N., 1994, "Heat Transfer from Vertical Surfaces to Dense Gas-Fluidized Beds," Int. J. Heat Mass Transfer **37**(16), pp.2465-2473

[45] Werther, J., 1999, "Measurement Techniques in Fluidized Beds," Powder Technology **102**, pp.15-36

[46] Sjösten, J., Golriz, M.R., Nordin, A. and Grace, J.R., 2004, "Effect of Particle Coating on Fluidized-Bed Heat Transfer," Ind. Eng. Chem. **43**, pp.5763-5769

[47] Agarwal, P.K., 1991, "Transport Phenomena in Multi-Particle Systems-IV. Heat Transfer to a Large Freely Moving Particle in Gas Fluidized Bed of Smaller Particles," Chemical Engineering Science **46**, pp.1115-1127

[48] Scott, S.A., Davidson, J.F., Dennis, J.S. and Hayhurst, A.N., 2004, "Heat Transfer to a Single Sphere Immersed in Beds of Particles Supplied by Gas at Rates above and below Minimum Fluidization," Ind. Eng. Chem. **43**, pp.5632-5644

[49] Parmar, M.S. and Hayhurst, A.N., 2002, "The Heat Transfer Coefficient for a Freely Moving Sphere in a Bubbling Fluidised Bed," Chemical Engineering Science **57**, pp.3485-3494

[50] Dincer, I., Kilic, Y.A. and Kahveci, N., 1996, "Heat Transfer Modelling of Spherical Particles Subject to Heating in a Fluidized Bed," Int. Comm. Heat Mass Transfer **23**(5), pp.705-712

[51] Linjewile, T.M., Hull, A.S. and Agarwal, P.K., 1993, "Heat Transfer to a Large Mobile Particle in Gas-Fluidized Beds of Smaller Particles," Chem. Eng. Sci. **48**, pp.3671-3675

[52] Prins, W., Casteleijn, T.P., Draijer, W. and Van Swaaij, W.P.M., 1985, "Mass Transfer from a Freely Moving Single Sphere to the Dense Phase of a Gas Fluidized Bed of Inert Particles," Chemical Engineering Science **40**(3), pp.481-497